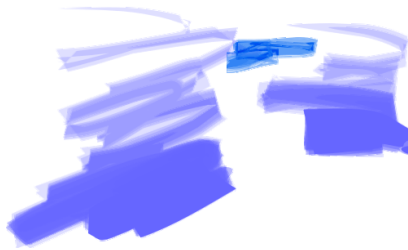


THE UNIVERSITY OF NEW SOUTH WALES
SCHOOL OF PHYSICS



Mesoscopic Quantum Ratchets and the
Thermodynamics of Energy Selective
Electron Heat Engines

Tammy E. Humphrey

*A thesis submitted in fulfilment of the requirements
for the degree of Doctor of Philosophy*

September 6, 2003

Abstract

A ratchet is an asymmetric, non-equilibrated system that can produce a directed current of particles without the need for macroscopic potential gradients. In rocked quantum electron ratchets, tunnelling and wave-reflection can induce reversals in the direction of the net current as function of system parameters.

An asymmetric quantum point contact in a GaAs/GaAlAs heterostructure has been studied experimentally as a realisation of a quantum electron ratchet. A Landauer model predicts reversals in the direction of the net current as a function of temperature, amplitude of the rocking voltage, and Fermi energy.

Artifacts such as circuit-induced asymmetry, also known as "self-gating", were carefully removed from the experimental data, which showed net current and net differential conductance reversals, as predicted by the model. The model also predicts the existence of a heat current where the net electron current changes sign, as equal numbers of high and low energy electrons are pumped in opposite directions by the asymmetric ratchet potential at this point.

An idealised quantum electron ratchet is studied analytically as an energy selective electron heat engine and refrigerator. The hypothetical device considered consists of two electron reservoirs with different temperatures and Fermi energies. The reservoirs are linked via a resonant state in a quantum dot, which functions as an idealised energy filter for electrons. The efficiency of the device approaches the Carnot value when the energy transmitted by the filter is tuned to that where the Fermi distributions in the reservoirs are equal.

The maximum power regime, where the filter transmits all electrons that contribute positively to the power, is also examined. Analytic expressions are obtained for the power and efficiency of the idealised device as both a heat

engine and as a refrigerator in this regime of operation. The expressions depend on the ratio of the voltage to the difference in temperature of the reservoirs, and on the ratio of the reservoir temperatures. The energy selective electron heat engine is shown to be non-endoreversible, and to operate in an analogous manner to the three-level amplifier, a laser based quantum heat engine. Implications for thermionic refrigerators and power generators are discussed.

Contents

1	Outline	8
1.1	Part I	8
1.2	Part II	10
I	Experimental Mesoscopic Quantum Ratchets	12
2	Introduction to Ratchets and QPCs	13
2.1	Ratchets	13
2.1.1	What is a Ratchet?	13
2.1.2	The Smoluchowski-Feynman Ratchet	13
2.1.3	Types of Ratchets	15
2.1.4	Applications	17
2.1.5	Quantum Ratchets	18
2.2	Low-Dimensional Electron Transport in Semiconductor Heterostructures	19
2.2.1	The Two-Dimensional Electron Gas in GaAs/AlGaAs .	19
2.2.2	Quantum Point Contacts (QPCs)	21
2.2.3	The Landauer Equation	22
3	Asymmetric Conductance in QPCs	26
3.1	Experimental Devices and Set-up	26
3.1.1	Devices: Background, Fabrication and Characterization	26
3.1.2	Experimental Setup	27

3.2	Distinguishing Circuit and Device Asymmetry	32
3.2.1	Circuit Induced Asymmetry	33
3.2.2	Using Symmetry Relations to Remove CIA	36
3.2.3	The Symmetric Gating Technique	40
3.3	Experimental Verification of Symmetry Relations	42
3.3.1	Data from the Symmetric Device A5	43
3.3.2	Data from the Asymmetric Device D3	46
3.3.3	A Zero-Bias Anomaly in the Bias Spectroscopy Measurements	50
3.4	Conclusions	54
4	Asymmetric QPCs as Quantum Ratchets	56
4.1	Quantum Ratchets	56
4.2	Theory	62
4.3	Numerical Model	67
4.3.1	Modelling the potential	67
4.3.2	Modelling the voltage drop	70
4.3.3	Calculation of the transmission probability	71
4.3.4	Numerical Results	71
4.4	Experimental Data	77
4.4.1	Net Differential Conductance versus Gate Voltage . . .	78
4.4.2	Net Differential conductance versus Source-drain Voltage	83
4.4.3	Net Differential Conductance versus Temperature . . .	85
4.5	Conclusions	88

II The Thermodynamics of Energy Selective Electron Heat Engines **90**

5	Introduction to Electron Heat Engines	91
5.1	The Thermodynamics of Heat Engines and Refrigerators . . .	92
5.1.1	What is a Heat Engine?	92
5.1.2	Carnot Efficiency and Reversibility	93

5.2	Electronic Systems as Heat Engines and Refrigerators	94
5.2.1	Thermoelectric Power Generators and Refrigerators . .	94
5.2.2	Thermionic Power Generators and Refrigerators	98
5.2.3	Cryogenic Electron Refrigerators	100
5.3	Brownian Heat Engines	101
5.4	Finite Time Thermodynamics	105
5.4.1	What is Finite Time Thermodynamics?	105
5.4.2	Endoreversibility and the Curzon-Ahlborn Efficiency .	105
5.4.3	Brownian Heat Engines in Finite Time	107
6	Quantum Ratchets as Heat Pumps	109
6.1	Adaptation of Landauer Theory to Heat Currents	111
6.2	Numerical Calculations for the Experimental Ratchet	113
6.3	Numerical Calculations for a Double Barrier Ratchet	118
6.4	Conclusions	124
7	Energy Selective Electron Heat Engines	126
7.1	Using Energy Filtering in an Electron Heat Engine	126
7.1.1	The Energy Selective Electron Heat Engine	127
7.1.2	The Idealised Rocked Resonant Tunnelling Ratchet . .	128
7.1.3	The Seebeck Resonant Tunnelling Ratchet	130
7.2	Reversible Regime of Operation	130
7.2.1	Entropy Change due to Transfer of Electrons between Electron Reservoirs	131
7.2.2	Number Flux between Electron Reservoirs	133
7.2.3	Heat Flux and Calculation of the Efficiency	134
7.3	Maximum Power Regime of Operation	136
7.3.1	Maximum Power Achievable with a 1D System	138
7.3.2	The Intermediate Case: Between Maximum Power and Maximum Efficiency	152
7.3.3	Comparison with the Three-Level Amplifier	158
7.4	Conclusions	164

8 Outlook	166
8.1 Energy Filtering in Thermionic Power Generators and Refrigerators	166
8.1.1 Efficient Thermionic Power Generation	167
8.1.2 Efficient Thermionic Refrigeration	168
8.2 Relationship with Thermoelectric Theory	168
A Fabrication Details	171
B Details of the Data Analysis	174
C Dependence of τ on the barrier shape	176
D Numerical Calculation of τ	182
E Saddle-point Potential Model	184
F Fermi Distribution Proof	185
G Derivation of $\delta S/\delta N$	187
H 2D-0D-2D and 3D-0D-3D transport	189
I Maximum Power Integrals	193

Acknowledgements

I thank my supervisors, Heiner Linke and Richard Newbury for their ongoing encouragement, support and advice, and for taking the time to read and give feedback on many drafts of this thesis.

My husband, David Humphrey, has been a sounding board for my ideas, and encouraged me to persevere when things were difficult.

Conversations with Prof. Poul-Erik Lindelof on the experimental work are gratefully acknowledged, as well as his hospitality during my visit to his Lab to fabricate devices.

Many, many, thanks to Jack Cochrane, whose assistance made the experimental work so much easier. Also to Adam Micolich, who gave experimental advice and provided great feedback on this thesis in record time.

Thanks to Josh Gotham, Andrew Brown and to Dave (again) for proof-reading and helping me polish this thesis in the final days, I really appreciated the help.

Finally to my family, Mum, Karen and Robyn; Dave's family, Margaret and Andy, Steve and Claire, and to my friends, thanks for persevering in asking me how it was going, and patiently listening to the answer, for so long.

This thesis is dedicated to my late father, Owen Dann, who always encouraged and assisted me.

Cover Illustration: stylised sketch of an energy selective electron heat engine.

Publications

1. "Experimental Tunneling Ratchets" H. Linke, T.E. Humphrey, A. Löfgren, A.O. Sushkov, R. Newbury, R.P. Taylor, and P. Omling, *Science*, **286**, 2314-2317 (1999).

The numerical modelling for this experiment was performed by the author, and is described in chapter 4 of this thesis. A ‘follow-up’ experiment using new devices is the subject of the experimental chapters (3 and 4) of this thesis.

2. "Pumping Heat with Quantum Ratchets" T.E. Humphrey, H. Linke and R. Newbury, *Physica E*, **11**, 281-286 (2001).

This paper was based on the work presented in Chapter 6 of this thesis.

3. "Reversible Quantum Brownian Heat Engines for Electrons" T.E. Humphrey, R. Newbury, R.P. Taylor and H. Linke, *Physical Review Letters*, **89**, 116801 (2002).

This paper consists of the first part of Chapter 7 of this thesis.

4. "The Thermodynamics of Ballistic Electron Heat Engines", T.E. Humphrey, H. Linke and R. Newbury, *Unpublished* (proposed PRB article).

This paper, currently in draft form, covers all of Chapter 7 of this thesis.

5. "Carnot Efficiency in Thermionic Refrigerators and Power Generators", T.E. Humphrey and H. Linke, *Unpublished* (proposed APL article).

This paper, also currently in draft form, is an extension of the Outlook chapter, examining the implications of the results of Chapter 7 of this thesis for conventional thermionic refrigerators and power generators.

Chapter 1

Outline

As reflected by the title, the work described in this thesis represents a journey from the fabrication and experimental study of mesoscopic electron ratchets, to a fully analytical analysis of the thermodynamics of energy selective electron heat engines. The thesis is divided into two parts along these lines, with results presented essentially in the order they were obtained. The experimental work appears first, while the most significant results obtained in the thesis, the thermodynamic performance limits of energy selective electron heat engines, are located towards the end in Chapter 7.

1.1 Part I

Quantum point contacts (QPCs) are one-dimensional constrictions for electrons with a width close to that of an electron wavelength at temperatures below 10 K, around 50 nm. In the first part of this thesis, QPCs which are asymmetric (wider at one end than the other) are studied as experimental quantum ratchets. In general, ratchets are devices which utilise asymmetry and a source of energy, such as non-directional fluctuations, to produce a directed current of particles in the absence of net macroscopic forces. In quantum ratchets, effects such as tunnelling and wave reflection affect the operation of the ratchet, and can produce changes in the direction of the

rectified current. The aim of the experimental work presented in the first part of this thesis was to observe reversals in the direction of the rectified current in an asymmetric QPC and achieve an understanding of the physical origin of these reversals using a numerical Landauer model.

Part I of the thesis consists of three chapters. The first (Chapter 2 of the thesis) is an introduction to the physics of ratchets and QPCs. The second (Chapter 3) consists of two main parts. Firstly the fabrication of the devices and experimental setup used to measure the conductance of QPCs is discussed. The second part of Chapter 3 describes a preliminary experimental study of asymmetry in the conductance of QPCs. The conductance of a quantum point contact may be asymmetric in the sign of the voltage as a result of either asymmetry present in the device itself, or alternatively, asymmetry in the experimental circuit used to measure the conductance. The aim of the study was to examine two different experimental procedures which may be used to distinguish between the above sources of asymmetry. One of these procedures was then used to isolate that part of the conductance which was due to device asymmetry in the experiment work described in Chapter 4.

Chapter 4 describes the study of an asymmetric QPC specifically as an implementation of a quantum ratchet, and contains the main results of the experimental section of the thesis. Firstly, a numerical model is developed to understand how the conductance of an asymmetric QPC under positive and negative voltages depends upon its shape. The conductance predicted by this model as a function of temperature, Fermi energy and voltage is then compared to the experimentally measured differential conductance of an asymmetric quantum point contact, with good qualitative agreement between the two.

1.2 Part II

The entirely theoretical work presented in part II was motivated by questions raised by the experimental work. One of the conclusions of the numerical model presented in first part of the thesis is that the energy spectrum of electrons transmitted through a quantum ratchet depends upon the sign of the voltage applied across it. In other words, that the application of a square-wave voltage to a quantum ratchet can result in a heat current, even when the net electrical current is zero.

Chapter 5 is an introduction to heat engines in general, and electron heat engines in particular, looking at thermionic and thermoelectric refrigerators and power generators, as well as more recently developed cryogenic electron refrigerators. Also discussed are thermal Brownian motors, which are ratchets where energy supplied via a temperature variation is used to do work against a load.

In Chapter 6, the numerically calculated efficiency of heat pumping by a quantum ratchet constructed using an asymmetric quantum point contact design is compared to that of an asymmetric resonant tunnelling double barrier structure. It is found that the asymmetric QPC does not pump heat very effectively, but that when resonances in the double barrier structure are very narrow, the resonant tunnelling quantum ratchet can actually remove heat from one side, that is, it can refrigerate an electron reservoir. In search of the limiting efficiency of such resonant tunnelling ratchets, a very idealised structure, to be called an "energy selective electron heat engine" (ESE heat engine) in this thesis, was then studied analytically.

Chapter 7 describes results obtained for this generalised electron heat engine in a number of different regimes of operation. The first analysed is the maximum efficiency regime, where the performance of the ESE heat engine is shown to be limited only by the Carnot efficiency. Analytical expressions for the power and efficiency of the ESE heat engine and ESE refrigerator are obtained for operation in the maximum power regime. Lastly, the regime intermediate to these is studied numerically.

Finally, in Chapter 8 it is shown that the work described in Chapter 7 is expected to have significant implications for the design of practical electron heat engines such as thermionic refrigerators and power generators, offering improvements in both the power and efficiency. This is one of the most exciting findings of this thesis, and illustrates somewhat the unpredictability of scientific investigation, that what began as an experimental study of quantum ratchets realised in quantum point contacts has led to new ideas for improving the efficiency of refrigerators.

Part I

**Experimental Mesoscopic
Quantum Ratchets**

Chapter 2

Introduction to Ratchets and QPCs

2.1 Ratchets

2.1.1 What is a Ratchet?

A ratchet may be described as an asymmetric, non-equilibrated system in which the random thermal motion of particles can be rectified to produce directed motion, without the application of a time-averaged net macroscopic force in the direction of motion. It is the presence of non-equilibrium which distinguishes a ratchet from a *perpetuum mobile* of the second kind, that is, a perpetual motion machine in which energy is conserved but the second law of thermodynamics is not obeyed.

2.1.2 The Smoluchowski-Feynman Ratchet

A thought experiment originally proposed by Smoluchowski [1], and later expanded upon by Feynmann in his Lectures on Physics [2], illustrates the impossibility of rectifying thermal fluctuations with a system in equilibrium, even if it contains a source of asymmetry. The system considered consists of a microscopic vane, subject to Brownian motion due to collisions with

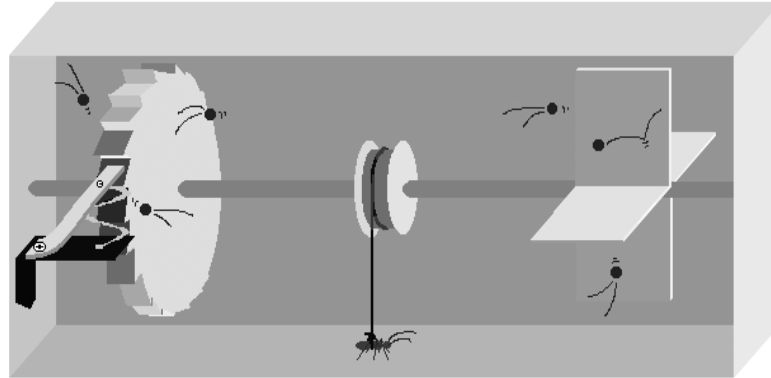


Figure 2.1: The Smoluchowski-Feynman ratchet. The thermal fluctuations in the vane on the right are intended to be rectified by the ratchet and pawl mechanism on the left to do some work (such as lifting a small weight). However, if the vane and the ratchet are held at the same temperature the device cannot operate without violating the second law of thermodynamics.

atoms in a gas at a particular temperature, shown on the right in Figure 2.1, and a ‘ratchet and pawl’, shown on the left in Figure 2.1, also in the same thermal bath as the vane. The ratchet teeth are asymmetric, so that the progression of the ratchet in one direction is ‘easier’ than the other. The intended purpose of the ratchet and pawl is to rectify the motion of the vane so that rotation is more likely to occur in one direction than the other, in order to do useful work such as lifting a small weight. If the device could actually achieve this objective, then useful work would be obtained from a system in equilibrium, in violation of the second law of thermodynamics. The important point is that it is not only the vane, but also the ratchet and pawl which are subject to Brownian motion, with the fluctuations in energy of the spring holding the pawl due to collisions with the atoms in the thermal bath causing it to occasionally lift up, allowing free rotation of the ratchet beneath it. If they are at the same temperature as the vane, then a detailed analysis [2] shows that the probability of forward and reverse motion of the ratchet is the same, so that no useful work can be done by the system.

Feynman also considered the situation where the ratchet and pawl is held at a different temperature to the vane, and showed that in this *non-equilibrium* case the system can operate as a heat engine to perform useful work. He also estimated the conversion efficiency to be that of a Carnot engine, but Parrondo and Español have shown this to be incorrect, and that the efficiency of the Feynman ratchet is limited to a value below the Carnot efficiency [3].

2.1.3 Types of Ratchets

In his comprehensive review [4], Reimann distinguishes *pulsating ratchets* [5, 6, 7, 8, 9, 10], in which the shape of the ratchet potential varies with time, and *tilting ratchets* [11, 12, 13, 14, 15, 16], in which the ratchet potential is subject to an external force with a time-average of zero (known as *rocked ratchets* when the driving force is periodic). A simple example of a pulsating ratchet where the potential alternates in time between two distinct potential shapes (known as an *on-off ratchet*) is shown in Figure 2.2. Particles subject to Brownian noise are confined by an asymmetric periodic potential, which is later 'switched-off' so that the particles may freely diffuse away from the potential minima where they were previously collected. When the potential is 'switched-on' again, the asymmetry of the potential ensures that they are more likely to be captured by the minima on the left (in this example) than the minima on the right, and a net transfer of particles to the left occurs. Even though no net macroscopic force has been used to obtain a net current the non-equilibrium condition has been fulfilled as the input of energy is required to lift the particles when the potential is reapplied.

Figure 2.3 shows a classical rocked ratchet. An asymmetric potential tilted up and down symmetrically is shown at three different moments in time during one period (τ) of operation, $t = 0.25\tau$, tilted up, $t = 0.5\tau$, at zero tilt, and at $t = 0.75\tau$, tilted down. The change in height of the potential barriers when the asymmetric potential is rocked up and down means that Brownian particles subject to the potential are more likely to have sufficient energy to traverse the barriers to the right at $t = 0.75\tau$ in Figure 2.3, than

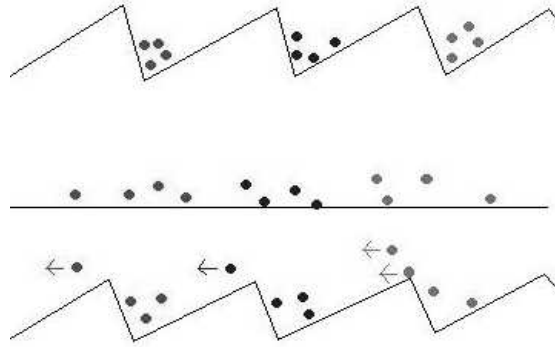


Figure 2.2: A schematic of an on-off ratchet. An asymmetric potential is shown, from the top down, at times $t = 0$, at $t = 0.5\tau$, where it is 'switched off', and finally at $t = \tau$, at which time it has been switched on again. Brownian particles are confined to the potential minima at $t = 0$, when the potential is dropped at $t = 0.5\tau$ they diffuse away. When the potential is reapplied at time $t = \tau$ the asymmetry of the potential ensures that a particle is more likely to be captured by the minima to the left than the minima to the right, so that a net current of particles occurs. This process thus rectifies thermal motion to produce a directed current of particles. This process is not in conflict with the second law of thermodynamics as energy is supplied to the system each time the potential is reapplied.

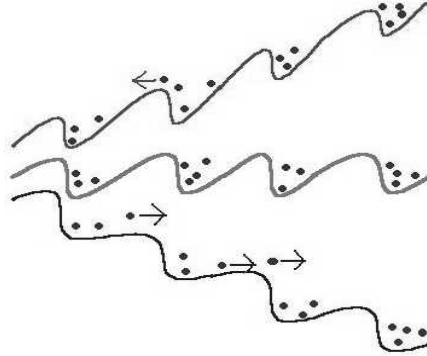


Figure 2.3: A rocked ratchet. The three vertical figures (from top to bottom) show the ratchet potential at time $t = 0.25\tau$, $t = 0.5\tau$ and $t = 0.75\tau$ respectively, where τ is the period of operation of the ratchet. The asymmetry of the potential means that the heights of the potential barriers are lower at $t = 0.75\tau$ than at $t = 0.25\tau$, and operating the ratchet produces a net current of particles to the right (in this particular case).

to the left at $t = 0.25\tau$. This means that on average, a current of particles will flow to the right in the rocked ratchet shown in Figure 2.3.

2.1.4 Applications

There are a number of reasons for studying particle transport in the presence of noise and absence of net macroscopic forces. One reason is that just such an environment is found inside cells, where motor proteins such as kinesin, myosin and dyneins utilise chemical energy gained by hydrolysis of adenosinetriphosphate (ATP) into adenosinediphosphate (ADP) and phosphorous, to move along asymmetric (polar) pathways to transport vesicles inside cells and to contract muscles, and are also important in the process of cell division [17]. These biological systems have been modelled as ratchets with some success, as reviewed in [18].

Another application of ratchets is in particle separation. If a small slope (net force) is added to the ratchet potential in Figures 2.2 and 2.3 then

particles may still be transported by the ratchet up the slope (up to some 'stopping' force). If two types of particles are deposited in the ratchet, then there exists the potential for one to be transported in the opposite direction to the other (one up and one down the slope) allowing separation [19]. Separation of fragments of DNA suspended in water has been achieved using a flashing asymmetric electric field, switched at a rate which allows fragments with higher rates of diffusion to travel towards the electrodes more quickly than others [20, 21, 22]. Other recently realised experimental schemes allow for the transport of particles against a concentration gradient on a micrometer [23] and nanometer scale [24].

2.1.5 Quantum Ratchets

What distinguishes a *quantum ratchet* from the simple examples of classical ratchets discussed earlier? If the classical Brownian particles in the rocked ratchet shown in Figure 2.3 are replaced by quantum particles, which have the ability to tunnel through narrow barriers and to be wave-reflected from sharp barriers, then the crucial difference is that it is not just the change in *height* of a potential barrier which determines the particle current through the ratchet, but also the change in *shape* of the ratchet potential when it is tilted up and down which is important in determining the magnitude and direction of the current produced by the ratchet. A temperature dependent net current reversal for quantum particles in a rocked ratchet was predicted theoretically by Reimann et al. [25, 4] for an over-damped system (of non-fermions) and has been observed experimentally by Linke et al. (with corresponding numerical modelling by the author) [26] for electrons in the ballistic transport regime. This experiment will be discussed in more detail in Chapter 3, as it is the starting point for the experimental work described in this thesis. Through the numerical model [26] a physical picture is developed of the origin of the net current reversal in ballistic quantum ratchets, and this will also be presented in Chapter 3.

Linke et al. have also measured net current reversals in triangular quan-

tum dots through which electron transport is coherent [27, 28, 29]. In that experimental quantum ratchet system, current rectification was achieved via interference effects, rather than as a result of tunnelling or wave reflection effects, as is the case for the experimental quantum ratchets reported in [26] and in this thesis.

2.2 Low-Dimensional Electron Transport in Semiconductor Heterostructures

A semiconductor heterostructure was chosen for the physical implementation of a quantum ratchet, as asymmetric potentials are easily implemented, and techniques for measuring currents through such devices at cryogenic temperatures, where quantum effects such as tunnelling and wave-reflection are observable, is well-developed.

2.2.1 The Two-Dimensional Electron Gas in GaAs/AlGaAs

Semiconductor heterostructures are composed of a number of single crystal layers of semiconductor material which are ‘grown’ on top of each other to single-atomic-layer precision using techniques such as molecular beam epitaxy. GaAs and $\text{Al}_{0.3}\text{Ga}_{0.7}\text{As}$ are direct bandgap semiconductor materials which are often used because their lattice-constant is well matched, while the bandgap of the materials differs by approximately 300meV. The resulting mismatch of the conduction band edges when the two different materials are grown adjacent to each other causes band-bending, as electrons rearrange themselves until the Fermi energy is constant across the interface. Figure 2.4 (a) shows the offset in conduction bands between the AlGaAs and GaAs, and also that electrons from an AlGaAs layer doped with the electron donor Si flow down to the GaAs layer as a result of the potential difference between the band edges. The n-doped layer is separated from the GaAs by an AlGaAs spacer layer to improve the mobility of electrons at the AlGaAs/GaAs

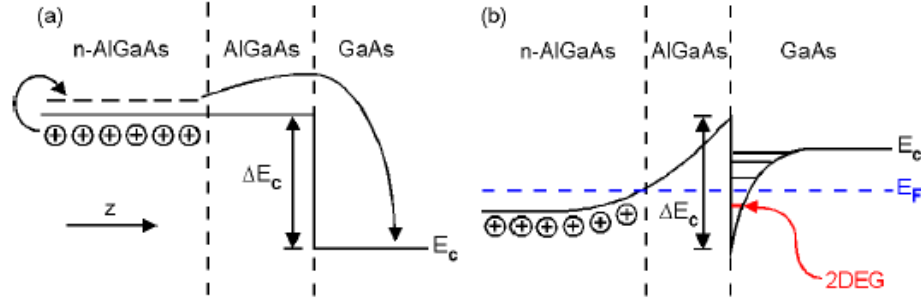


Figure 2.4: (a) shows the conduction band offset at the interface of AlGaAs and GaAs. Free electrons from Si donors follow the gradient between the semiconductor materials until the Fermi energy is constant across the interface. This situation is shown in (b), where band-bending has produced a triangular quantum well at the interface. Thermal smearing of the Fermi occupation function is not sufficient to allow population of the second level in the well, so electrons are confined to the plane defined by the interface of the semiconductors. Figure taken from [30] with permission.

interface. Figure 2.4 (b) shows the band-bending which results from this rearrangement of electrons.

The band-bending produces a triangular shaped potential well with a spacing of allowed energy levels of the order of 30meV, large enough that the second level is not thermally populated by electrons at cryogenic temperatures, and thus confining electrons in the well to the interface of the GaAs and AlGaAs and producing a 'two-dimensional electron gas' (2DEG).

Further confinement to one- or zero dimensions (1D or 0D), and patterning of the 2DEG is possible, for example, by deep or shallow etching [31], or surface-gate [32] techniques, and these are illustrated in Figure 2.5 (a), (b) and (c). Etching is done by covering the wafer of semiconductor with a resist, which is patterned by exposing a certain area by photolithography, for large features ($\sim \text{mm} \rightarrow 10 \mu\text{m}$), or a scanning electron microscope beam for very small features ($\sim 10 \mu\text{m} \rightarrow 100 \text{nm}$). After development, which removes

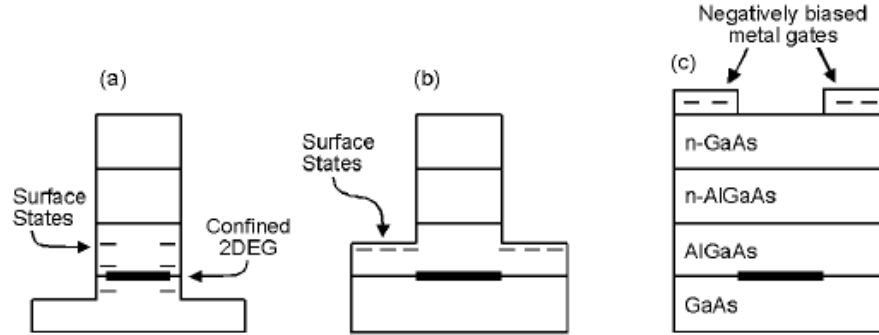


Figure 2.5: (a) is a schematic of the amount of semiconductor material which is removed to confine electrons in the 'deep-etching' technique, showing the production of surface-states at the edges of the confined 2DEG. (b) shallow etching prevents the formation of surface states near the 2DEG, increasing its mobility. (c) illustrates the use of metal top gates to confine the 2DEG below the surface. Taken from [30] with permission.

the resist in exposed areas, the sample is etched using an acid and peroxide to remove areas which have been exposed. The etch time determines how many layers of semiconductor are removed. UV photolithography and deep etching is generally used for fabricating Hall bars, an isolated area of 2DEG approximately $50\,\mu\text{m}$ by $20\,\mu\text{m}$ in size, with a number of ohmic contacts, as shown in figure 2.6. In the devices studied in this thesis, electron beam lithography and shallow wet-etching was then used to confine the 2DEG in the Hall bar to a smaller region which formed the quantum point contact (QPC), shown in figure 2.7.

2.2.2 Quantum Point Contacts (QPCs)

Quantum point contacts, or QPCs, have been extensively studied since the simultaneous discovery of quantised conductance by van Wees et al. [33] and Wharam et al. [34] in 1988. Quantised conductance is only observed at temperatures lower than $\approx 10\,\text{K}$, where the mean free path of electrons is

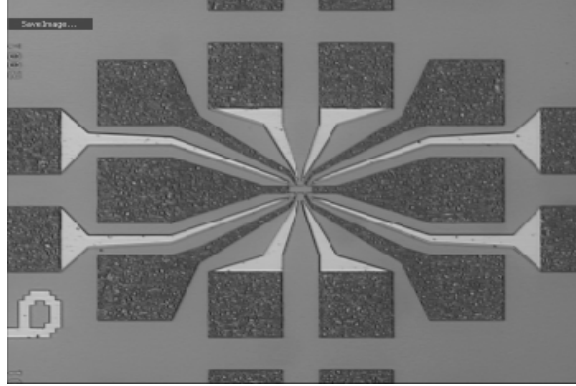


Figure 2.6: The Hall bar used for the devices is in the very centre of this picture (taken through a microscope, the field of view is a few mm^2). The Ohmic contacts (dark) and gates (whitish) are shown around it. These are composed of Ge/Au/Ni/Au, and are contacted with bonding wires to a chip holder, and thereby to the rest of the measurement setup.

longer than the length of the constriction, that is, where there is no scattering events with impurities, and the transport can thus be described as *ballistic*. The finite resistance of quantum point contacts does not arise from scattering events (as is the case for diffusive transport), but rather from the small width of the point contact constriction compared with that of the leads connecting it to the experimental setup. Very many transverse modes exist in the 2DEG far from the constriction, but the small width of the QPC ($\sim 250 \text{ nm}$) means that only a few transverse modes have an energy less than the Fermi energy, so current is limited to these.

2.2.3 The Landauer Equation

The Landauer equation [35, 36, 37, 38] (good overviews are given in [39, 40, 41]) relates the current through a ballistic conductor such as a quantum point contact to the probability that an electron can be transmitted through it. It is valid when the leads on either side of the conductor are reflectionless, that is, when electrons can enter them from the conductor without suffering reflec-

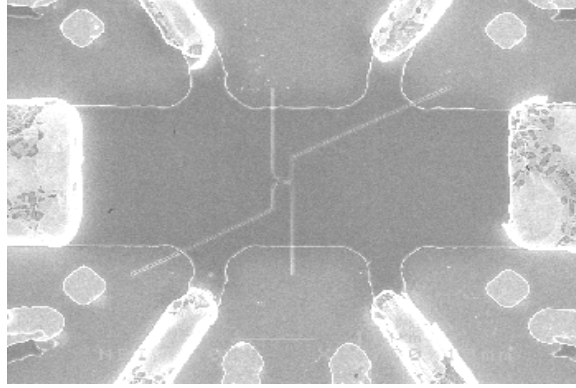


Figure 2.7: This magnified picture of the Hall bar shows just the central region of figure 2.6, and was taken using a scanning electron microscope (SEM). The 2DEG lies in the plane of the image below the surface. The light-coloured lines in the centre are the etched regions which outline the shape of the point contact. Around the outside the ohmic contacts may be seen (shiny due to the deposited metal). The top right and bottom left ohmic contacts the 2DEG on either side of the central point contact, forming the ‘side-gates’ which were used to adjust the width of the point contact. The white line just visible at the bottom centre corresponds to $10\ \mu\text{m}$.

tions. The central idea of this formalism is that the total current through the conductor is given by the difference between the left and right-going currents of electrons. Each of these currents is determined, as a function of electron energy, by the product of the density of states, Fermi occupation function, velocity and transmission probability of the electrons across the conductor. The current due to electrons from the left is then given by

$$I_L = 2e \int_0^\infty f[E(k), \varepsilon_L, T_L] \nu(k) \tau(k, V_{sd}) \frac{dk}{2\pi} \quad (2.1)$$

In this equation the factor of the electronic charge $e = -1.6 \times 10^{-19}$ changes number current to charge current. The factor of 2 at the front of the integral accounts for spin while $dk/2\pi$ is the density of k states in one-dimension. $f[E(k), \varepsilon_L, T_L]$ is the Fermi occupation function in the left lead, which gives

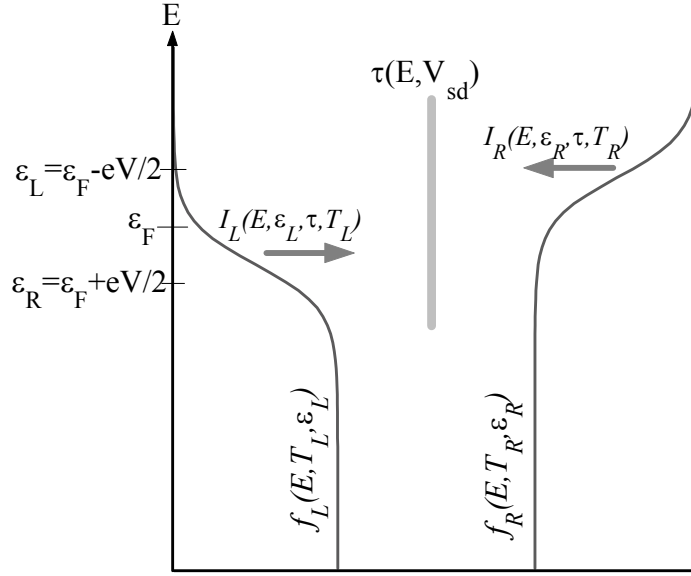


Figure 2.8: The Fermi occupation function of two electron reservoirs with different Fermi energies is shown. The current flowing between these reservoirs as a function of energy depends upon the difference in the occupation of states, $f_L - f_R$, and the transmission probability, $\tau(E, eV_{sd})$, where E is the energy of electrons and V_{sd} is the source-drain voltage between the reservoirs. The electronic charge $e = -1.6 \times 10^{-19}$, T_C and T_H are the temperatures in the reservoirs, and ϵ_F is the Fermi energies in the reservoirs when $V_{sd} = 0$.

the probability that a state is occupied, and is a function of the energy, E , of the state, the Fermi energy, ε , and the temperature, T , of the lead. $\nu(k)$ is the velocity of the electrons while τ is the probability that an electron with wavevector k is transmitted through the conductor. It is usually more convenient to integrate over energy, so the following substitution into equation 2.1 is made:

$$dk = \frac{dk}{dE}dE = \frac{1}{\hbar\nu}dE \quad (2.2)$$

$$I_L = \frac{2e}{h} \int_{U_L}^{\infty} f[E, \varepsilon_L, T_L] \tau(E, V_{sd}) dE \quad (2.3)$$

Here the bottom of the conduction band in the left lead is denoted by U_L . A common lower limit of integration may be used for the left and right lead currents if transport only occurs at energies much higher than the bottom of the left and right bands, or if the greater of U_L and U_R is used. The Fermi distribution on the left is given by:

$$f[E, \varepsilon_L, T_L] = \frac{1}{1 + \exp \frac{E - \varepsilon_L}{kT_L}} \quad (2.4)$$

The Fermi distributions in the left and right reservoirs are illustrated in Figure 2.8. The equation for the current due to electrons from the right is obtained similarly as

$$I_R = -\frac{2e}{h} \int_{U_R}^{\infty} f[E, \varepsilon_R, T_R] \tau(E, V_{sd}) dE \quad (2.5)$$

The total current is then

$$I(V_{sd}) = I_L + I_R = \frac{2e}{h} \int_{U_0}^{\infty} \tau(E, V_{sd}) \{f[E, \varepsilon_L, T_L] - f[E, \varepsilon_R, T_R]\} dE \quad (2.6)$$

This equation will be used to model transport through the asymmetric quantum point contact studied experimentally in this thesis. There is excellent agreement between Landauer equation and experimental results [39, 40, 41].

Chapter 3

Asymmetric Conductance in QPCs

3.1 Experimental Devices and Set-up

This chapter provides background information to Chapter 4. It outlines the devices and measurement setup, as well as a preliminary experiment, the purpose of which is to develop techniques for differentiating between different sources of asymmetry in conductance data from quantum point contacts. One of these techniques is then utilised in the main experimental work, which will be presented in Chapter 4.

3.1.1 Devices: Background, Fabrication and Characterization

The devices studied in this thesis were fabricated by the author in 2001 at the Ørsted Laboratory, Niels Bohr Institute, Copenhagen University, Denmark. Full details of the fabrication methods and parameters may be found in Appendix A.

Figure 3.1 is a diagram of the AlGaAs heterostructure wafer used as a starting point to make the devices. The wafer was grown by Claus Sørensen

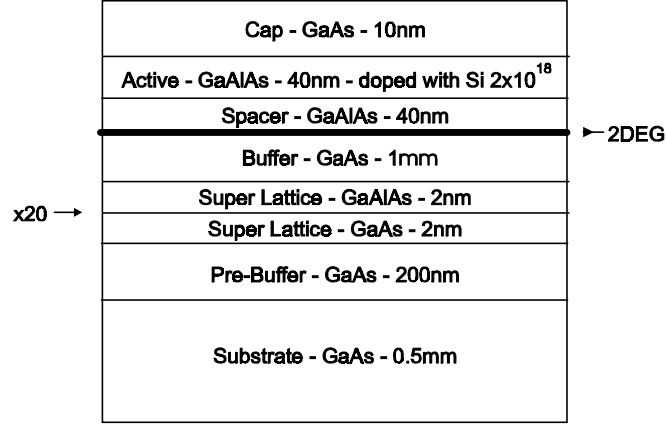


Figure 3.1: The heterostructure used for the devices. The 2DEG is located at the interface of the GaAs buffer and GaAlAs spacer layers.

in 1998 at the same institute. Figures 3.2 and 3.3 are scanning electron microscope images of the symmetric and asymmetric devices used in the experiments. Shubnikov-de Haas and Hall measurements were made on the samples by the author and it was found that the electron density was $2.05 \times 10^{15} \text{ cm}^{-2}$, and the Fermi energy, $\varepsilon_F = 7.5 \text{ meV}$.

3.1.2 Experimental Setup

Equipment

The experiments were performed using an Oxford Instruments Heliox pumped ^3He cryogenic system to achieve the base temperature of 0.23 K. An Iotech DAC488 Digital-to-Analog converter (DAC) was used to provide the DC source-drain voltages for the gates and bias voltages, while SR830 lock-in amplifiers were used as an AC source and to measure voltages across the device. The temperature of the device was measured using a Lakeshore Germanium resistor with a range of 30 mK to 5 K, which was located at the position of the device and heat sunk in the same manner. Temperatures above 5 K were measured using an Oxford instruments ITC (intelligent temperature controller) with a RuO resistor. A LabView software program was

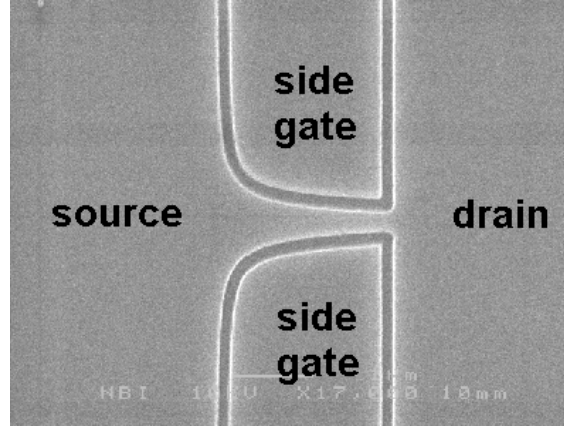


Figure 3.2: A SEM image of the asymmetric device D3 used in the experiments. The dark lines are etched trenches 50nm deep which deplete the 2DEG and so electrostatically define the device. A voltage, V_{sd} , is applied between the source and drain contacts and the conductance measured between the remaining two ohmics, as shown in figure 2.7. The areas above and below the device are contacted separately to the rest of the 2DEG and used as side gates to electrostatically tune the QPC width.

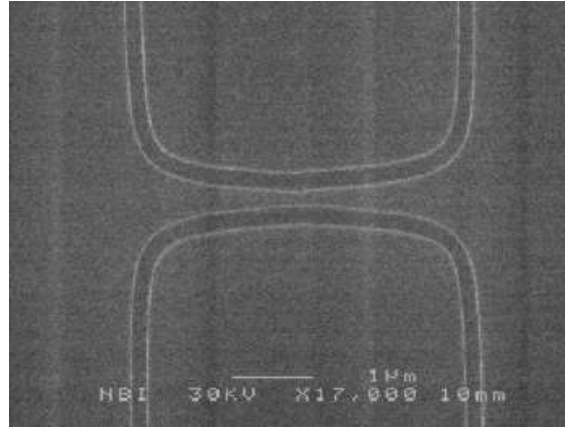


Figure 3.3: A SEM image of the symmetric device A5 used in the experiments. The shape is made by reflecting D3, shown in Figure 3.2, about its right edge.

used for control and data acquisition.

Measurement Circuit

Figure 3.4 shows the experimental circuit used. The Hall bar of the device is located at the top left of the figure, together with an indication of the lithography which separates the 2DEG in the Hall bar into side-gates (top right and bottom left), and the main conducting regions on either side of the QPC, connected via ohmic contacts to current (left and right centre) and voltage probes (top left and bottom right).

The gate voltage, which adjusts the width of the QPC, is applied using the DAC, whose four outputs are indicated in a box at the top right of the figure. Each output could be controlled independently using LabView software. The current through the device was calculated by measuring the voltage over a known (1K) resistor in series with the device, using a Lock-in amplifier (designated LI7 in the diagram). The voltage dropped over the device was measured using another Lock-in amplifier (designated LI8). Separate Ohmic contacts were used to carry current and to measure voltage (four-terminal measurement).

The signal sent to the device consisted of a DC component and a small AC component at 183Hz. These were added using the circuit shown at the bottom of the figure (the ‘AC/DC adder box’), which also reduced the magnitude of the DC voltage by a factor of 700 and reduced the amplitude of the AC voltage by a factor of 750, in order that larger DC and AC input voltages could be used (2V AC at the output of Lock-in 7 was reduced to 0.025mV at the device).

A relay switch (shown top right) was used to switch the grounding point of the gate to ground, or to half the bias voltage, by way of the two 100K resistors, which form a voltage divider. These two measurement configurations will be discussed in detail in the remainder of this chapter. The relay was controlled by a LabView program through a 0/10V voltage from the digital to analog convertor (DAC). The capacitor between the voltage divider and

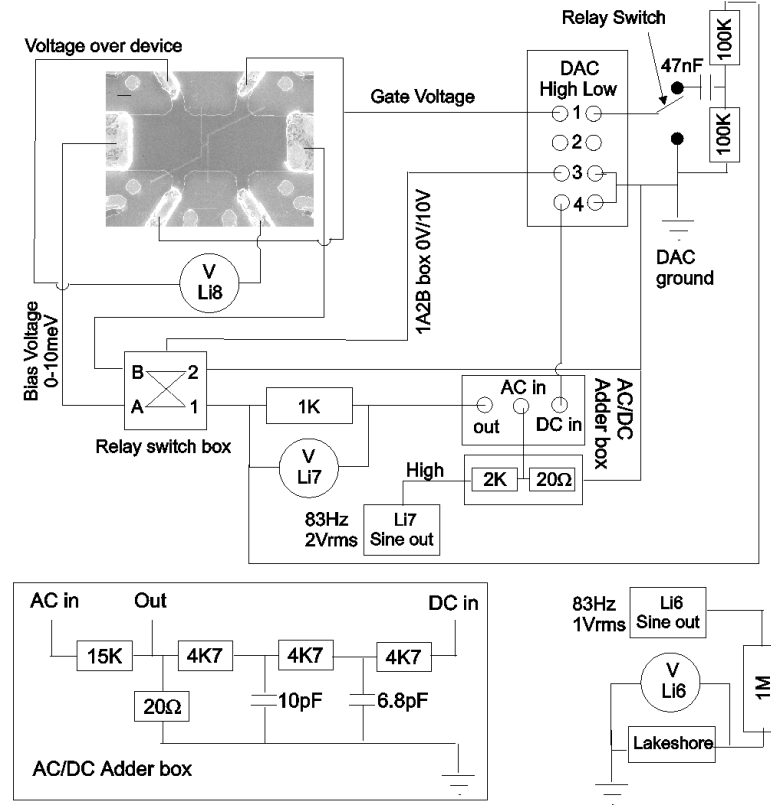


Figure 3.4: The circuit used for the measurements is shown. The device and its Ohmic contacts are shown in the top left-hand corner. The source-drain voltage is applied through a relay-switch box which was used to switch the source and drain Ohmics between 'Forward' and 'Reverse' measurement configurations. The DC and AC components of the source drain voltage originate at the DAC and a lock-in amplifier (marked LI7) respectively and are combined through the AC/DC adderbox, the circuit of which is shown in the bottom left corner of the figure. The voltages over the device and the $1K$ resistor were measured with lock-in amplifiers LI8 and LI7 respectively at the frequency of the AC part of the source-drain voltage, $83Hz$. The gate voltage was applied using the DAC (see the upper right corner of the figure) with respect to either ground or half the source-drain voltage via the voltage divider in the top right corner, depending upon whether the circuit was to be asymmetrically or symmetrically gated. In the range $0.23K$ to $5K$, the temperature was measured using the circuit shown at the bottom right of the figure, where LI6 refers to a lock-in amplifier.

the DAC low acted as a low pass filter to prevent the white noise (\sim mV in magnitude) on the DAC low being transmitted to the device. The temperature of the device was measured using the circuit shown in the bottom right of the diagram, where the resistor labelled ‘Lakeshore’ indicates the Lakeshore Ge resistor.

Experimental Methods

The experiments described in this thesis are concerned with measuring asymmetry in the conductance of QPCs which are lithographically asymmetric. In order to eliminate the possibility that asymmetry in the experimental data originated in the ohmics on the devices which were used as the source and drain contacts, measurements were made of the resistances of these contacts as a function of the source-drain voltage. The source and drain contacts on device A5 had resistances of $208 \pm 7 \Omega$ and $215 \pm 10 \Omega$ respectively, while those for the asymmetric device D3 had resistances of $205 \pm 5 \Omega$ and $204 \pm 10 \Omega$ for $V_{sd} = \pm 3$ mV. While the variation in the resistance of the contacts is up to 5% across the voltage range considered, it will be shown later that the lithographically symmetric device A5 yielded very symmetric data when measured under a symmetric gating setup, so it can be assumed that this level of variation in the resistance of the contacts did not contribute significantly to the asymmetry observed in the data when the experimental setup was switched to an asymmetric gating setup, or in the data from device D3, which was lithographically asymmetric.

In order to increase the signal to noise ratio in the experiment, a small AC signal was added to the DC source-drain voltage across the device. Lock-in amplifiers tuned to the frequency of the AC signal then measure the change in the conductance of the device due to the change in the voltage over the device, the *differential* conductance, dI/dV_{sd} . The AC voltage was always $< 50 \mu\text{V}$ in magnitude, which is approximately twice kT at 300mK. It is important that the magnitude of the AC signal used is large enough that it can be distinguished from thermal noise by the Lock-in amplifiers, but small enough

that it does not cause unnecessary heating of the electrons in the device. The frequency of the AC signal, 183 Hz, was carefully chosen to be high enough to reduce noise in the data, but low enough that the measurements were not frequency dependent. It is also important that the chosen frequency not be close to a multiple of 50 Hz, the power supply frequency. Time constants of 1 s were used on all the lockin amplifiers. This averaging time best balanced the competing requirements of low noise and finite measurement time. In the measurements, two of the three variable parameters (temperature, source-drain voltage and gate voltage) were kept constant whilst the other was swept. Details of the data analysis are given in Appendix B.

3.2 Distinguishing Circuit and Device Asymmetry

Measuring the conductance of asymmetric QPCs is complicated by the fact that, in general, the conductance of even lithographically symmetric QPCs is asymmetric under a change in the sign of the source-drain voltage (see, for example, [42, 43]). This is due to the fact that the grounding point of the gate and that of the source-drain voltage are not independent, and leads to a variation in the ‘effective’ gate voltage along the length of the device and a corresponding change in the conducting width along the device, depending upon the polarity of the source-drain voltage.

This type of asymmetry occurs in all gated devices, and also in devices which are capacitively coupled to a nearby equipotential region such as a parallel 2DEG. The effect is central to the operation of many commercial semiconductor devices such as MOSFETs, where it is responsible for the existence of ‘pinch-off’ [44]. Here, this source of non-symmetric conductance will be termed ‘circuit induced asymmetry’ (CIA).

In the experimental work presented in this thesis, we are primarily interested in non-symmetric conductance due to geometric asymmetry in the QPC itself, and any other source of non-symmetric conductance, such as

CIA, is an artefact that needs to be removed from the data. This section focuses on how this can be achieved, and consists of three parts.

1. Firstly, the physical origin of non-symmetric conductance due to CIA will be distinguished from that due to geometric asymmetry of the QPC in the direction of transport.
2. Two different techniques for removing CIA will be discussed. The first utilises symmetry relationships between the effects of CIA and device asymmetry on the conductance.
3. The second involves removing the component of the non-symmetric conductance due to CIA by applying the gate voltage with respect to the potential at the narrowest part of the QPC (setting the gate grounding point to half the source-drain voltage).

A preliminary experimental test of the effectiveness of the above two techniques will then be presented in the next section of this chapter.

3.2.1 Circuit Induced Asymmetry

Figure 3.5 (a) illustrates how asymmetry in the grounding point of the gate with respect to the narrowest part of a QPC can result in non-symmetric conductance. The three sets of curves indicate the width of the QPC for zero, positive and negative source-drain voltages in the presence of a side gate voltage applied across the length of the device. The width of the right end of the QPC remains constant, determined by the applied gate voltage. The width of the left side of the QPC varies with the sign of the source-drain voltage.

To see why this is the case, note that the application of a source-drain voltage establishes an electric field across the device in the direction of transport, which interacts self-consistently with the electrons in the gate, or any nearby equipotential region. The electrons in the gate arrange themselves in response to this field to maintain a constant electric potential. The sum

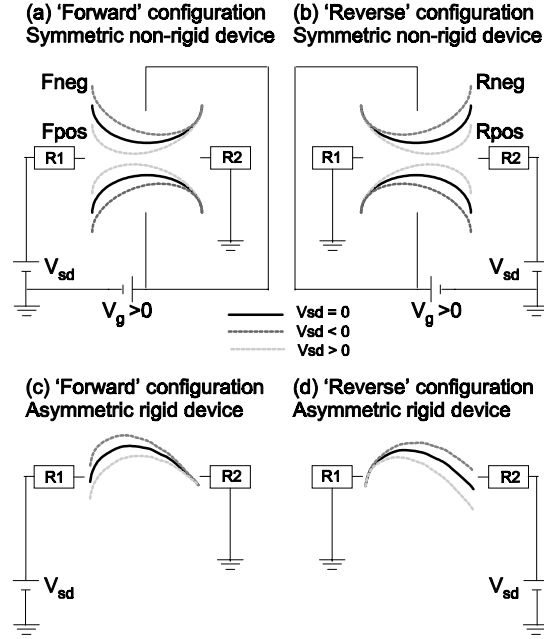


Figure 3.5: (a) and (b) show the effect of CIA on the conducting width of a symmetric, non-rigid device. The conductance of the device is different for source drain voltages of opposite sign, but the same if the source-drain contacts are reversed. For example, the width of the QPC in (a) for a positive source-drain voltage ('Fpos'), is not the same as that for a negative source-drain voltage ('Fneg'), but *is* the same as that in (b) for a positive source-drain voltage ('Rpos'). (c) and (d) show the *confinement potential* (not the width) of a rigid, asymmetric QPC under source-drain voltages of opposite sign. The conductance of the device is different if either the sign of the source-drain voltage or the device configuration is reversed, but the same if both the sign of the source-drain voltage and the device configuration is reversed. To see (qualitatively) that this can be the case, note that the *shape* of the barrier for positive source-drain voltage in (c) is different from that for negative source drain voltages in (c), but the same shape as that for negative source-drain voltages in (d), where the source and drain contacts have been switched. All this means is that if you flip the device, *and* switch the polarity of the source-drain voltage, the potential landscape in the device must be identical (in the absence of nearby, non-floating equipotential regions, i.e. as long as the device is rigid). The implication is that the effects of non-rigidity can be removed by averaging these two situations.

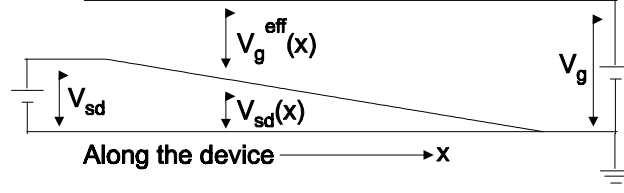


Figure 3.6: A schematic of the relationship between the variables V_{sd} , $V_{sd}(x)$, V_g and $V_g^{eff}(x)$.

of the ‘effective’ gate voltage, $V_g^{eff}(x)$, and the source-drain voltage $V_{sd}(x)$, must be constant along the device, and equal to the applied gate voltage, V_g . (See Figure 3.6 for an illustration of the relationship between these variables). The result is that the conducting width of the device is increased (for negative V_{sd}) or reduced (for positive V_{sd}) by differing amounts along the length of the device, as illustrated in Figure 3.5.

In general, the magnitude of the asymmetry in the conductance due to CIA depends on the particular QPC studied (upon, for instance, the fabrication techniques and semiconductor materials used). Following [42, 43, 45], in this thesis a device will be defined as *rigid* if CIA makes a negligible contribution to the conductance. Note that in [42, 43], the term ‘self-gating’ has been used to describe *any* dependence of the potential profile of a gated device upon the source-drain voltage. We may therefore distinguish between ‘self-gating’ and CIA, which is limited to the effect on the conductance of the variation in the width of the device due to the self-consistent interaction of the source-drain and gate voltages.

The above distinction is quite important, as it is the dependence of the *shape* of an *asymmetric* potential upon the sign of the applied source-drain voltage which is central to the effect of interest in the experimental part of this thesis, that is, the ability of a quantum ratchet to produce a net current (and net current reversals) under the application of a square-wave source-drain voltage. In a QPC, the potential barrier for the electrons arises due to quantum confinement, with a smaller width giving a higher barrier. In

Figure 3.5 (c), the shape of the confinement potential (*not* the QPC width as shown in (a) and (b)) of a *asymmetric* QPC (as in Figure 3.2) is indicated under zero, positive and negative source-drain voltages. The conductance of the asymmetric QPC is different for source-drain voltages of opposite sign because the potential barrier is deformed in a different way when tilted in opposite directions. This effect is simply that which was discussed in the introduction (§2.1.3).

3.2.2 Using Symmetry Relations to Remove CIA

We now focus upon techniques which may be used to remove the effect of CIA from experimental differential conductance measurements, leaving only the contribution from geometric asymmetry in the device. The first technique considered requires that in addition to measuring the differential conductance, dI/dV_{sd} , of a QPC for positive and negative source-drain voltages, these two measurements are repeated after switching the source and drain contacts on the device. In this work, the differential conductance of the device for each of these four measurements will be denoted g_{Fpos} , g_{Fneg} , g_{Rpos} and g_{Rneg} . Here ‘F’ stands for ‘Forward’ and ‘R’ for ‘Reverse’ measurement configuration, in which the source and drain contacts to the device have been reversed (swapped), while the ‘pos’ and ‘neg’ denote the sign of the source-drain voltage. The measurements are illustrated in Figure 3.5 (a) and (b). Certain symmetry relationships exist between these four measurements, and these may be utilised to remove the effects of CIA from the experimentally measured differential conductance.

The ‘total’ conductance $G = I/V_{sd}$ associated with the differential conductance measurements will be denoted G_{Fpos} , G_{Fneg} , G_{Rpos} and G_{Rneg} . As symmetry relationships which hold for the differential conductance can be shown to also hold for the conductance [45], we will use the conductance when deriving the symmetry relationships, as the arguments are more transparent when made for the ‘total’ conductance. Note also that for the following symmetry arguments to be valid, the resistance of the ohmic contacts

between the source and drain leads and the device, denoted R_1 and R_2 in Figure 3.5, must be equal (this can be achieved by the addition of a series resistance if necessary).

Rigid, Symmetric device

In a truly rigid (not subject to CIA) and geometrically symmetric device (denoted as R,S) the conductance depends upon the magnitude but not the sign of the source-drain voltage, so

$$G_{Fpos}(R, S) = G_{Fneg}(R, S) = G_{Rpos}(R, S) = G_{Rneg}(R, S) \quad (3.1)$$

Non-rigid, symmetric device

For a non-rigid symmetric device (NR,S), that is, one subject to CIA, the conductance depends upon the sign of the source-drain voltage, but cannot depend upon which end of the device the bias voltage is applied to, as the symmetry of the device implies that these 'Forward' and 'Reverse' configurations must be indistinguishable. In this case,

$$G_{Fpos}(NR, S) = G_{Rpos}(NR, S) \quad (3.2)$$

and

$$G_{Fneg}(NR, S) = G_{Rneg}(NR, S) \quad (3.3)$$

but

$$G_{Fpos}(NR, S) \neq G_{Rneg}(NR, S) \quad (3.4)$$

and

$$G_{Rpos}(NR, S) \neq G_{Fneg}(NR, S) \quad (3.5)$$

A measurement of the conductance as a function of source-drain voltage may be divided into a component which is symmetric ($f(x) = f(-x)$) in the sign of V_{sd} and a component which is antisymmetric ($f(x) = -f(-x)$) in the sign of the source-drain voltage, in the same way that any function can be divided into symmetric and antisymmetric components. The antisymmetric

part of the conductance which is due to CIA (to be denoted G^{CIA}) can be obtained by taking the difference of the conductance of a symmetric QPC under source-drain voltages of opposite sign.

$$G^{CIA}(NR, S) = 0.5 [G_{Fpos}(NR, S) - G_{Rpos}(NR, S)] \quad (3.6)$$

Figure 3.5 (a) and (b) shows the effect of CIA on the shape of a non-rigid, symmetric QPC. The width of the QPC at its narrowest point is different for positive and negative source-drain voltages, but the same if the source and drain leads are reversed.

Rigid, Asymmetric device

For a rigid asymmetric device (R,A), the conductance depends upon the sign of the source-drain voltage because the shape of the potential is different under source-drain voltages of opposite sign (this is not the case for a rigid symmetric device). The shape remains constant, however, if the polarity of the source drain voltage is swapped *and* the measurement configuration is also changed from 'forward' to 'reverse' (this is easily seen by considering an ordinary diode). The difference in voltage between the ends of the device in the second situation is the same as in the first, so they are physically identical, even though the absolute voltages in each case differ by a factor of $|V_{sd}|$. Figure 3.5 (c) and (d) show the confinement potential experienced by the electrons in the QPC in 'forward' and 'reverse' measurement configurations. It can be seen (qualitatively) that the confinement potential of $Fpos$ is the same shape as that of $Rneg$ (similarly, the potential of $Fneg$ is the same as that of $Rpos$). In this case

$$G_{Fpos}(R, A) = G_{Rneg}(R, A) \quad (3.7)$$

and

$$G_{Fneg}(R, A) = G_{Rpos}(R, A) \quad (3.8)$$

but

$$G_{Fpos}(R, A) \neq G_{Rpos}(R, A) \quad (3.9)$$

and

$$G_{Fneg}(R, A) \neq G_{Rneg}(R, A) \quad (3.10)$$

It follows that the *antisymmetric* part of the conductance which is due to device asymmetry (to be denoted G^{DA}) can be obtained as

$$G^{DA}(R, A) = 0.5 [G_{Fpos}(R, A) - G_{Rpos}(R, A)] \quad (3.11)$$

Non-rigid, Asymmetric device

In order that the device and circuit-induced asymmetry may be distinguished in the general case of a non-rigid, asymmetric device (NR,A) the symmetry relationships outlined for a rigid asymmetric, and a non-rigid symmetric device are used to eliminate the component of the antisymmetric part of the conductance due to CIA. This leaves only the part of the conductance which is symmetric in the sign of the source-drain voltage, G^{sym} , the antisymmetric part which is due to the geometrical asymmetry of the device, G^{DA} , and possibly a component due to the interaction between the two effects, to be denoted as G^x . As we will remove any part of the conductance with the same symmetry relations as G^{CIA} , this extra component will have the same symmetry relations as the G^{DA} , and constitutes any change in G^{DA} which would occur if a device could be changed from being ‘rigid’ to ‘non-rigid’. That is, we are allowing an extra theoretical term to describe any dependence of G^{DA} upon a non-zero G^{CIA} [45]. Such dependence might be expected given that both effects arise from the self-consistent adaptation of the electrochemical potential to a non-zero source-drain voltage.

In summary, what is needed is the conductance of the QPC with CIA effects removed, under positive and negative source-drain voltages. What we have is the conductance *with* CIA effects under positive and negative source drain voltages, measured in *both* ‘forward’ and ‘reverse’ configurations. This extra information is used to eliminate the antisymmetric part of the conductance by taking the following combinations of the experimentally measured

conductances:

$$G(+V_{sd}) \equiv 0.5(G_{Fpos} - G_{Rneg}) = G^{DA} + G^{sym} + G^x(+V_{sd}) \quad (3.12)$$

$$G(-V_{sd}) \equiv 0.5(G_{Fneg} - G_{Rpos}) = -G^{DA} + G^{sym} + G^x(-V_{sd}). \quad (3.13)$$

We then define the ‘net’ differential conductance as

$$G^{net}(|V_{sd}|) \equiv 0.5[G(+V_{sd}) - G(-V_{sd})] \quad (3.14)$$

$$= G^{DA} + G^x(+V_{sd}) + G^x(-V_{sd}). \quad (3.15)$$

These definitions of the conductance for positive and negative voltages, and their difference, the net conductance, will be used extensively in Chapter 4, which examines asymmetric QPCs as quantum ratchets.

3.2.3 The Symmetric Gating Technique

The second technique that can be used to remove the contribution of CIA to the asymmetry of the data involves applying the gate voltage with respect to half the source-drain voltage rather than with respect to ground [45]. It is the asymmetry of the grounding point of the gate voltage with respect to the centre of the QPC which results in an antiymmetric component of the conductance due to CIA.

Symmetric grounding is shown in Figure 3.7 (b), where a positive voltage applied to the source contact of the device causes that end to become narrower and the drain end wider (assuming a positive gate voltage). The opposite occurs when a negative bias voltage is applied to the source end of the device. This means that the differential conductance must be the same in both of these situations for symmetric devices, as the shape of the potential for negative bias voltages is simply the reverse of that for positive potentials.

For asymmetric devices, though the device may have the same width at its narrowest point for both positive and negative bias voltages (if half the bias voltage drops before and after the narrowest point), its asymmetry means that the shape of the potential in each configuration will be different.

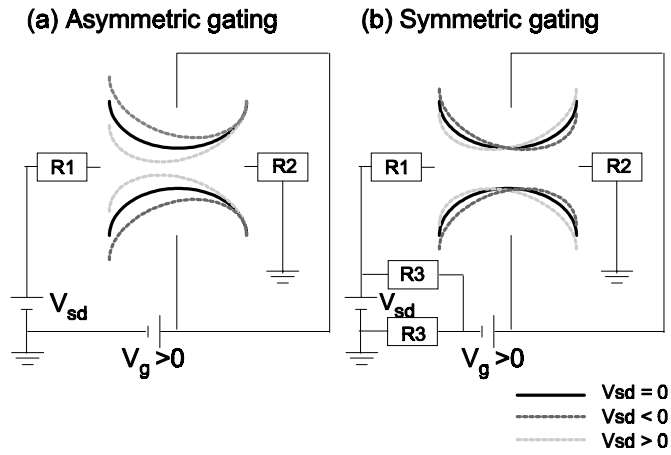


Figure 3.7: (a) The change in the shape of a QPC due to circuit-induced asymmetry when the gate voltage is applied relative to the same ground as the bias voltage. (b) The change in the shape of a QPC when the gate voltage is applied relative to the potential at the centre (or narrowest point) of the device, usually one-half of the applied bias voltage. The resistors R1 and R2 are the resistances of the ohmic contacts, which must be the same (a series resistor can be added to make sure this is the case) while R3 is the resistance used for the voltage divider, which was 100K in the experimental measurements.

As conductance in the ballistic regime is sensitive to both the height and the shape of potential barriers, CIA may still make a small contribution to the asymmetry of the data. The symmetry relationships between g_{Fpos} , g_{Fneg} , g_{Rpos} and g_{Rneg} (where small g denotes differential conductance) were tested experimentally for both asymmetric and symmetric gating and both symmetric and asymmetric devices, and the results are shown in §3.3.

3.3 Experimental Verification of Symmetry Relations

This section provides a preliminary experimental test of the theory presented in §3.2. In particular Equations 3.11 and 3.6, which relate the antisymmetric contribution to the conductance due to device asymmetry (DA), that due to circuit-induced asymmetry (CIA), and the four measurements $Fpos$, $Fneg$, $Rpos$ and $Rneg$, were tested experimentally for the four cases of

1. A symmetric device under symmetric gating. Device asymmetry, g^{DA} , (where small g denotes *differential* conductance) and circuit-induced asymmetry, g^{CIA} , are both expected to be very small, so that one expects $g_{Fpos} \approx g_{Fneg} \approx g_{Rpos} \approx g_{Rneg}$.
2. A symmetric device under asymmetric gating. Device asymmetry, g^{DA} , is expected to be small but circuit-induced asymmetry, g^{CIA} , may be large (depending upon how rigid the device is, generally dependent upon the material and fabrication techniques used), so it is expected that $g_{Fpos} \approx g_{Rpos}$ and $g_{Fneg} \approx g_{Rneg}$, but $g_{Fpos} \neq g_{Fneg}$ and $g_{Rpos} \neq g_{Rneg}$.
3. An asymmetric device under symmetric gating. Device asymmetry, g^{DA} , may be large (depending upon how asymmetric the device is) but circuit-induced asymmetry, g^{CIA} , is expected to be small by comparison, so that $g_{Fpos} \approx g_{Rneg}$ and $g_{Fneg} \approx g_{Rpos}$, but $g_{Fpos} \neq g_{Rpos}$ and $g_{Fneg} \neq g_{Rneg}$.

4. An asymmetric device under asymmetric gating. Device asymmetry, g^{DA} , may be large and circuit-induced asymmetry, g^{CIA} , may also be significant, so that $g_{Fpos} \neq g_{Fneg} \neq g_{Rpos} \neq g_{Rneg}$.

The expected relationships between g_{Fpos} , g_{Fneg} , g_{Rpos} and g_{Rneg} for these four measurement scenarios, for non-rigid devices, are summarised in Table 3.1.

	Symmetric Device		Asymmetric Device	
Symmetry Relations	Sym Gating	Asym Gating	Sym Gating	Asym Gating
$g_{Fpos} =$	$g_{Fneg}, g_{Rpos}, g_{Rneg}$	g_{Rpos}	g_{Rneg}	<i>None</i>
$g_{Fneg} =$	$g_{Rpos}, g_{Rneg}, g_{Fpos}$	g_{Rneg}	g_{Rpos}	<i>None</i>
$g_{Rpos} =$	$g_{Rneg}, g_{Fpos}, g_{Fneg}$	g_{Fpos}	g_{Fneg}	<i>None</i>
$g_{Rneg} =$	$g_{Fpos}, g_{Fneg}, g_{Rpos}$	g_{Fneg}	g_{Fpos}	<i>None</i>

(Table 3.1)

3.3.1 Data from the Symmetric Device A5

In the experiment, the DC source-drain voltage supplied by the DAC was applied over the 1K resistor, the ohmic contacts *and* the QPC (see Figure 3.4). This means that the fraction of source-drain voltage dropped over the QPC depends upon the conductance of the QPC relative to the 1K resistor and ohmic contacts. As the conductance of the device is, in general, a function of the polarity of the source-drain voltage, it is not strictly correct to directly compare the differential conductance measurements for the device under opposite polarity source-drain voltages applied over the whole setup, because different traces correspond to slightly different bias voltages. Rather what should be done is to take a number of V_g sweeps at a small spacing in V_{sd} and then using the measured conductance and a knowledge of the applied V_{sd} and the resistance of the rest of the circuit, assign to each conductance data point the appropriate source-drain voltage. Details of this procedure are given in Appendix B. The values of V_{sd} shown in figures is always the source-drain voltage drop over the device itself.

The differential conductance of the symmetric device A5 (shown in Figure 3.3) was measured at a temperature of 0.3 K as a function of gate voltage at intervals in V_{sd} of 0.2 mV, in both ‘Forwards’ and ‘Reverse’ source-drain contact configurations, that is, measurements at a particular source-drain voltage were immediately repeated with the source and drain contacts on the device swapped. The actual V_{sd} over the device was then determined for each data point as described above, producing a bias spectroscopy plot such as that shown later in this chapter for device A5 (Figure 3.11).

Data for $|V_{sd}| = 0.5$ mV and $|V_{sd}| = 1$ mV as a function of gate voltage is shown in Figure 3.8 for both symmetric and asymmetric gating. Figure 3.8 (a) shows g_{Fpos} , g_{Fneg} , g_{Rpos} and g_{Rneg} for both $|V_{sd}| = 0.5$ mV and $|V_{sd}| = 1$ mV (offset in the vertical axis by $2e^2/h$ for clarity) for symmetric gating. The main point to note about (a) is that all four curves are almost indistinguishable, as expected from Table 3.1 for a symmetric device under symmetric gating. Figure 3.8 (c) shows the asymmetric components g^{CIA} and g^{DA} of the symmetric gating measurement due to circuit-induced-asymmetry (CIA) and device asymmetry (DA), as defined by Equations 3.11 and 3.6. Physically, g^{DA} is the average of the difference between g_{Fpos} and g_{Rpos} and between g_{Rneg} and g_{Fneg} , while g^{CIA} is the average of the difference between g_{Fpos} and g_{Rneg} and between g_{Rpos} and g_{Fneg} . When the symmetric device A5 is asymmetrically gated, it can be seen from Figure 3.8 (b) that g_{Fpos} and g_{Rpos} are very similar to each other but very different from g_{Fneg} and g_{Rneg} , as expected from Table 3.1. This leads to g^{CIA} being much larger than g^{DA} in (d), meaning that the asymmetry in the differential conductance due to CIA is much more significant for A5 than the asymmetry in the differential conductance to device asymmetry, as would be expected for a lithographically symmetric device.

The main feature of g^{CIA} for asymmetric gating is the large peaks occurring on the rise to the plateaus, which are absent for symmetric gating. It is on the rise to the plateaus that the differential conductance changes most rapidly with V_g . It is also the case that, for asymmetric gating situations,

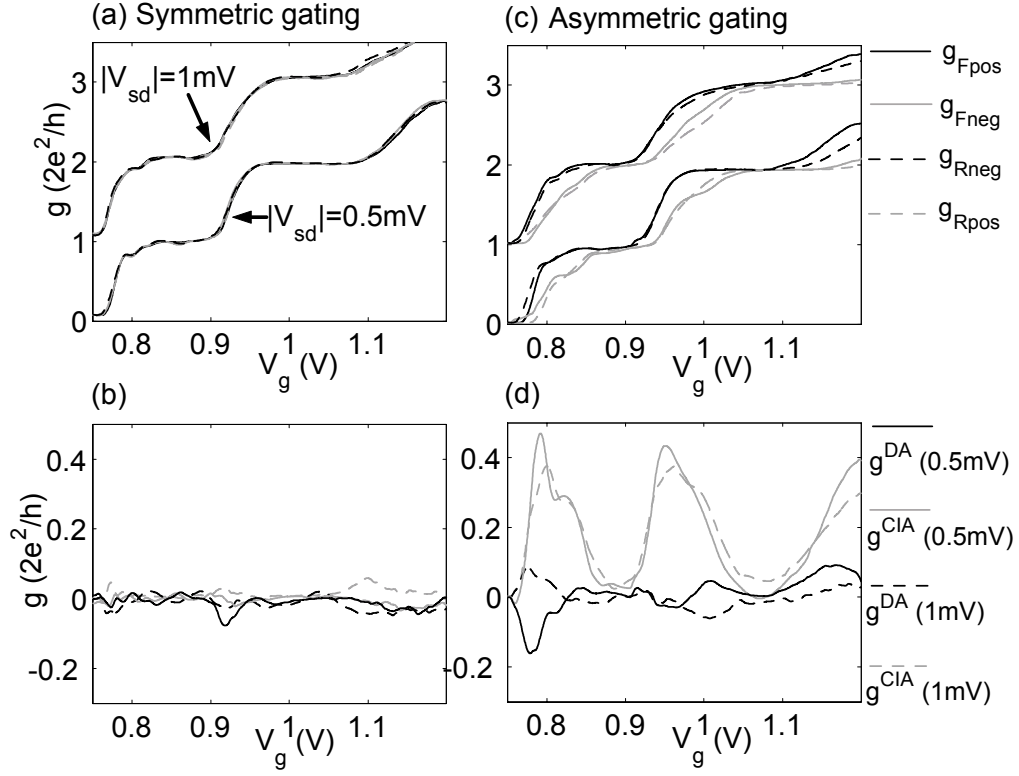


Figure 3.8: Data for the symmetric device A5. (a) shows g_{Fpos} , g_{Fneg} , g_{Rpos} and g_{Rneg} for symmetric gating, for source-drain magnitude of 0.5mV and 1.0mV, offset from the 0.5mV data by $2e^2/h$ for clarity, and included to show that results are representative of a range of source-drain voltage amplitudes. (b) shows the difference between the above measurements, the quantities g^{DA} and g^{CIA} , as defined by Equations 3.11 and 3.6. (c) g_{Fpos} , g_{Fneg} , g_{Rpos} and g_{Rneg} for symmetric gating, again for source-drain magnitudes of 0.5mV and 1.0mV. (d) g^{DA} and g^{CIA} for data in (c).

the effect of opposite polarity source-drain voltages is to change the effective gate voltage at the centre of the QPC. It is therefore expected that g^{CIA} will be largest at gate voltages for which the differential conductance is between integer values of $2e^2/h$. A second feature of the data is a difference in the magnitude of g^{DA} between (b) and (d). A possible explanation for this change is that even though A5 is lithographically symmetric, small imperfections in the lithography, or the presence of defects away from the centre of the QPC have resulted in a non-zero g^{DA} . As mentioned in §3.2.2, when both device asymmetry and circuit-induced asymmetry are present, it is expected that there may be an additional component g^x with the same symmetry as g^{DA} in the differential conductance due to the self-consistent interaction of CIA and DA. It may be this term (g^x) which causes the change in g^{DA} for symmetric and asymmetric gating. Such a change in the magnitude of g^{DA} is also seen for the asymmetric device D3 in Figure 3.9.

3.3.2 Data from the Asymmetric Device D3

Some instability in the differential conductance versus gate voltage characteristics of device D3 meant that consistent data sets could be obtained over a few hours, but not over days, the required time window to obtain the large data sets which were measured for device A5. Differential conductance data was therefore taken for the asymmetric device D3 just at two source-drain voltages, $V_{sd} = \pm 0.5$ mV and $V_{sd} = \pm 1.0$ mV, for ‘Forward’ and ‘Reverse’ source-drain contact configurations, rather than for a very large number of source-drain voltages as was done for device A5. Measurements were repeated for both symmetric and asymmetric gating situations, and are shown in Figure 3.9.

The data in Figure 3.9 shows that for an asymmetric device under symmetric gating conditions (Figure 3.9 (a) and (b)), the component of the differential conductance due to device asymmetry, g^{DA} is much larger than g^{CIA} , that is, in Figure 3.9 (a), g_{Fpos} is very similar to g_{Rneg} but differs significantly from g_{Fneg} and g_{Rpos} , as expected from Table 3.2. Under asymmetric

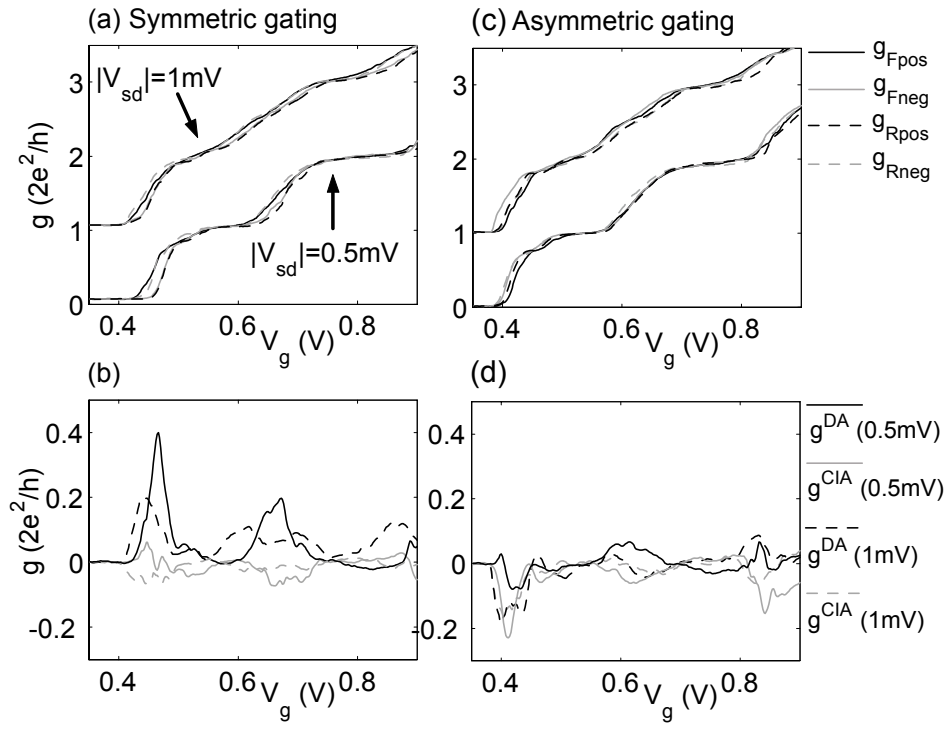


Figure 3.9: As for Figure 3.8, except for the asymmetric device, D3.

gating conditions, shown in (c) and (d) g_{Fpos} , g_{Fneg} , g_{Rpos} and g_{Rneg} all differ, as expected from Table 3.1.

	Symmetric Device		Asymmetric Device	
	Symmetric Gating (V)	Asymmetric Gating (V)	Symmetric Gating (V)	Asymmetric Gating (V)
$V_{sd}=0.5\text{mV}: \gamma^{CIA}$	0.71×10^{-2}	7.95×10^{-2}	1.06×10^{-2}	2.21×10^{-2}
$V_{sd}=0.5\text{mV}: \gamma^{DA}$	0.86×10^{-2}	1.18×10^{-2}	2.93×10^{-2}	1.25×10^{-2}
$V_{sd}=1\text{mV}: \gamma^{CIA}$	0.76×10^{-2}	8.04×10^{-2}	0.88×10^{-2}	1.44×10^{-2}
$V_{sd}=1\text{mV}: \gamma^{DA}$	0.96×10^{-2}	1.05×10^{-2}	3.46×10^{-2}	1.86×10^{-2}

(Table 3.2)

As for the symmetric device, A5, there was a substantial change in the magnitude of g^{DA} with a change from symmetric to asymmetric gating.

In order to quantify more clearly the contributions of CIA and DA to the asymmetric differential conductance, γ^{CIA} and γ^{DA} , the integrated magnitudes of g^{DA} and g^{CIA} , are defined according to Equations 3.16 and 3.17.

$$\gamma^{DA}(|V_{sd}|) \equiv \int_a^b |G^{DA}(|V_{sd}|, V_g)| dV_g \quad (3.16)$$

$$\gamma^{CIA}(|V_{sd}|) \equiv \int_a^b |G^{CIA}(|V_{sd}|, V_g)| dV_g \quad (3.17)$$

The values of γ^{DA} and γ^{CIA} calculated for the data shown in this chapter are given in Table 3.2. Figure 3.10 is a graph of the first two rows of Table 3.2, that is, γ^{DA} and γ^{CIA} for $|V_{sd}| = 0.5\text{mV}$. $|V_{sd}| = 1\text{mV}$ was not plotted as the results are very similar to those for $|V_{sd}| = 0.5\text{mV}$. Figure 3.10 illustrates three main points which have been made:

1. Symmetric gating reduces the amount of asymmetry in the differential conductance due to circuit-induced asymmetry for both the symmetric (A5) and asymmetric (D3) devices (Compare the A5, S and A Gating columns in the front row, and the D3, S and A Gating columns in the front row).

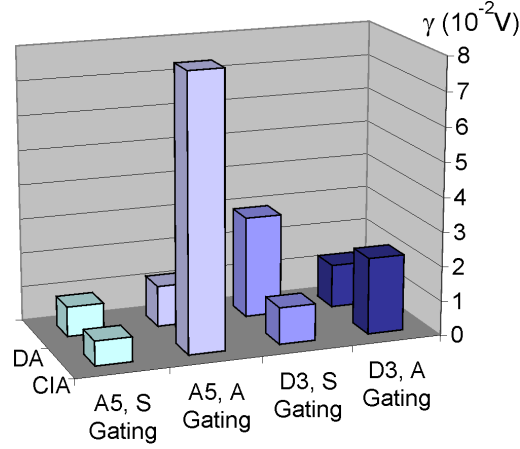


Figure 3.10: The data in the top two rows in Table 3.2 is shown graphically, with the front row of columns corresponding to γ^{CIA} and the back, γ^{DA} . The vertical axis measures 10^2 times the integrated magnitude of γ^{CIA} and γ^{DA} . From left to right, the columns represent device A5 symmetrically gated, corresponding to the integrated differential conductance data from Figure 3.8 (c), A5 asymmetrically gated, with data from Figure 3.8 (d), D3 symmetrically gated, data from Figure 3.9 (c) and finally on the far right, D3 asymmetrically gated, data from Figure 3.9 (d).

2. For symmetric gating, the device asymmetry is much larger in the lithographically symmetric device (D3) than the lithographically symmetric device (A5) (Compare the A5, S-Gating and D3, S-Gating columns in the back row)
3. It appears that the interaction of CIA and DA in asymmetric gating situations can change the magnitude of γ^{DA} , the amount of asymmetry in the differential conductance due to device asymmetry. For A5, γ^{DA} was increased when asymmetric gating was used, for D3, γ^{DA} was reduced. Whilst the existence of such an effect was allowed for in the simple model given in §3.2.2, it is likely that a self-consistent calculation would be needed to explain the magnitude of the difference in γ^{DA} between symmetric and asymmetric gating which was measured

experimentally.

3.3.3 A Zero-Bias Anomaly in the Bias Spectroscopy Measurements

This section briefly discusses a significant peak which was observed in the differential conductance of the symmetric device A5 under symmetric gating conditions around $V_{sd} = 0$. Small peaks (labelled a ‘Zero Bias Anomaly’ (ZBA) in [46]) have been recently been observed in some QPC measurements, for example by Kristensen et al. [43] at temperatures of $\sim 300\text{mK}$, and by Cronenwett et al. at temperatures of $\sim 50\text{mK}$ [46], but not in others, for example those of Reilly et al, which were also performed at temperatures of $\sim 50\text{mK}$ [47]. Cronenwett et al. [46] have suggested that this feature may be important in understanding the origins of the so-called ‘0.7 structure’, a shoulder-like feature which appears at a differential conductance value of approximately $0.7 \times 2e^2/h$.

The 0.7 Structure

The 0.7 structure appears almost ubiquitously in conductance measurements on QPCs, and has been studied experimentally by a number of groups [48, 49, 43, 50, 51, 52, 47]. What is agreed upon is that the structure is spin and density related (electron-electron interactions become significant at low densities). It has been suggested that the effect is due to spontaneous magnetisation of the one-dimensional system [53, 54, 55, 56, 57] or a two-electron bound state with non-zero total spin [58, 59].

The suggestion of Cronenwett et al. [46] that the effect originates in the formation of a Kondo-like correlated spin state has also recently been theoretically examined, finding support from Hirose et al. [60]. Seelig and Matveev find that backscattering of electrons from acoustic phonons can give rise to a zero-bias anomaly [61]. Using the unrestricted Hartree-Fock approach, Sushkov [62] has shown that the presence of a Kondo-like state

should result in a dip in the differential conductance below $0.2 \times 2e^2/h$. As dips of such magnitude are not seen in the experimental data, Suskov concludes that the 0.7 structure is not caused by a Kondo-like state. However, the calculation does confirm the existence of a few-electron bound state with total spin zero which is most pronounced for low electron densities and long contacts.

The focus of the present section this chapter is, however, not upon the 0.7 structure itself. Rather it will be shown that symmetric gating techniques appear to dramatically enhance the zero-bias anomaly. This suggests that symmetry considerations may be important in understand the origin of the ZBA in quantum point contacts.

Bias Spectroscopy Measurements on Device A5

The complete data set of conductance versus V_{sd} for the symmetric device A5 under symmetric gating conditions at a temperature of 300mK is shown in Figure 3.11 (a). The dark vertical line in the centre occurs because data was taken at a higher resolution close to $V_{sd} = 0$. This central region is shown in detail in (b). The 0.7 structure can be seen as a dark horizontal ridge just below the first conductance plateau, which is also seen as a dark ridge located at $2e^2/h$ for $V_{sd} = 0$. A structure just beneath the second conductance plateau at $2 \times 2e^2/h$ may also be seen. A similar feature has been observed by Kristensen et al. [43]. Half-plateaus at $0.5 \times 2e^2/h$ and $1.5 \times 2e^2/h$ may be seen at source-drain voltages of ~ 2 mV.

Note that the data was measured as a function of gate voltage, as this was most convenient for the purposes of the symmetry investigations of this chapter. The horizontal lines plotted in (a) and (b) were then interpolated from a large number of gate voltage sweeps. This means that the gate voltage resolution is very high, while that on the source-drain voltage axis is relatively low (varies between 0.02 and 0.1 mV). Semi-transparent lines were used in (a) to enable the plotting of data for a large number of gate voltages without making the conductance plateaus overly dark.

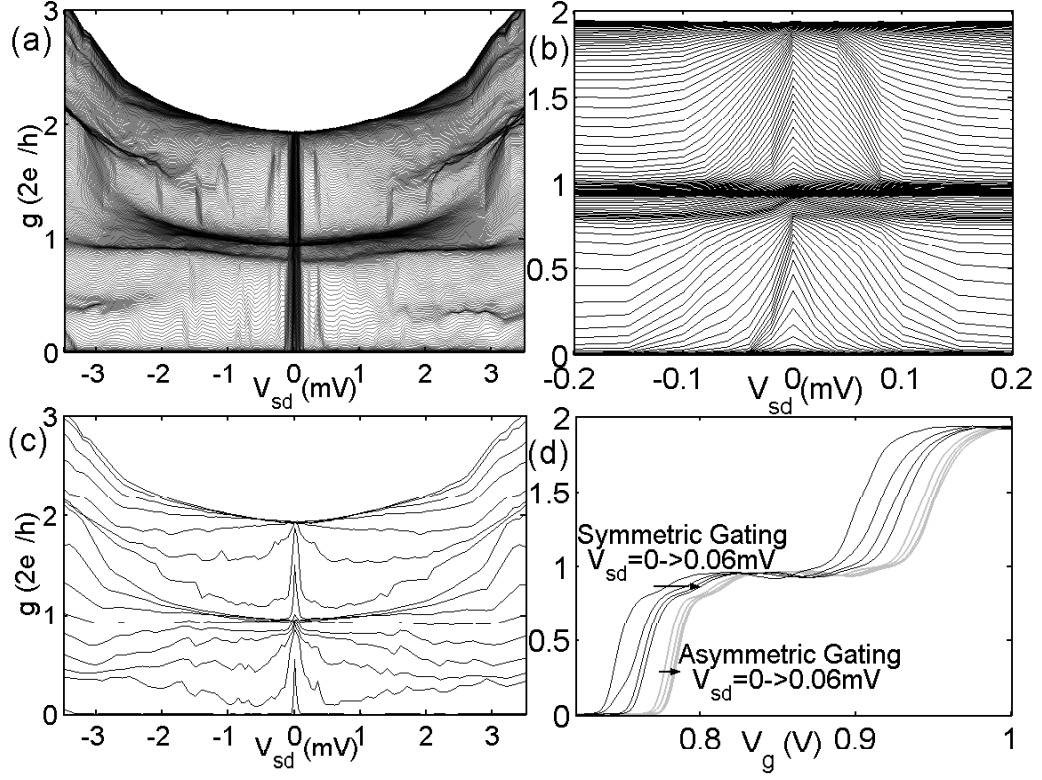


Figure 3.11: (a) Bias spectroscopy plot for device A5 under symmetric gating, for $T = 0.3$ K. (b) The same data for a very small range of source-drain voltages around zero. (c) A number of traces from (a) showing the very significant zero-bias anomaly. (d) Differential conductance as a function of gate voltage for $V_{sd} = 0, 0.02, 0.04, 0.06$ mV, for both symmetric and asymmetric gating. The zero-bias anomaly can be seen in the movement of the traces from right to left with increasing source-drain voltage. This effect is much more pronounced for symmetric, rather than asymmetric gating.

Data for a number of different gate voltages as a function of source-drain voltage, chosen from the data set in (a) are shown in (c). Here the very significant peaks in the differential conductance around $V_{sd} = 0$ are most clearly visible. Gate voltage sweeps for source-drain voltages of $V_{sd} = 0, 0.02, 0.04$ and 0.06 mV for the symmetric device under symmetric and asymmetric gating conditions are shown in (d). The ZBA is seen as a movement of the conductance traces to right for increasing V_{sd} . The ZBA seen for the device A5 under symmetric gating conditions is much larger than that observed under asymmetric gating. Zero-bias anomalies of this magnitude have not (to the authors knowledge) been observed before, and require verification on other devices measured under symmetric gating conditions. This was not done in the experimental work of this thesis due to its focus on understanding asymmetric quantum point contacts as quantum ratchets.

Interestingly, the bias spectroscopy data of Cronenwett et al. [46] appears very symmetric, and shows a noticable ZBA at low (~ 50 mK) temperatures. The bias spectroscopy data of Reilly et al. [4] is, on the other hand, very asymmetric in the sign of the source-drain voltage, and no ZBA is seen. It may be that the symmetry of a QPC (including the ohmic contacts) and its susceptibility to circuit-induced asymmetry are important considerations in understanding the origins of the ZBA. Some physical justification for why symmetric gating might be important for the study of bound states in quantum point contacts can be seen from Figure 3.7, which shows that in a device subject to CIA, the width of the centre of the point contact changes with the sign of the source-drain voltage. When symmetric gating is used, the width of the centre of the QPC is effectively 'pinned', possibly allowing bound states to persist to higher values of source-drain voltage.

The author thanks Prof. Poul-Erik Lindelof for drawing her attention to the significance of the peaks at zero bias observed in the experimental data.

3.4 Conclusions

Asymmetry in the differential conductance of quantum point contacts results from asymmetry in the grounding point of the gate voltage (called circuit-induced asymmetry, CIA), and/or asymmetry in the shape of the potential experienced by the electrons. It has been demonstrated in this chapter that these two sources of asymmetry are experimentally distinguishable. Two methods for distinguishing these effects were presented.

1. The first consisted of measuring the differential conductance under positive and negative source-drain voltages, and then repeating these two measurements with the source and drain contacts to the device switched. Symmetry relationships between these measurements were utilised to remove the linear contribution made by CIA to the asymmetry of the differential conductance. This is the technique used to treat the data presented in the following Chapter 4.
2. The second technique requires the gate voltage be applied with respect to the potential at the narrowest point in the QPC. This method ensures that the effect of CIA on the width, and thus the conductance of the device, is symmetric in the sign of the source drain voltage. The use of a 2:1 voltage divider in parallel with the device as the low of the gate voltage was successful in producing very symmetric differential conductance data for the symmetric device, implying that the potential at the narrowest point in the device is very close to half the bias voltage. This technique was suggested by Löfgren [45], and was implemented by the author after the experimental work presented in Chapter 4 had been completed. Symmetric gating has significant potential for more widespread use in quantum point contact measurements. In particular, it is very interesting that symmetric gating appears to dramatically enhance the zero-bias anomaly. This may be due to a 'pinning' of the width of the narrow region of the QPC, which allows any localised electron states in that region to persist to higher values of source-drain

voltage.

Chapter 4

Asymmetric QPCs as Quantum Ratchets

4.1 Quantum Ratchets

This chapter will describe experiments conducted on asymmetric mesoscopic quantum point contacts (the fabrication of which was described in the previous chapter and Appendix A) at cryogenic temperatures ($0.3\text{ K} \rightarrow 4.2\text{ K}$) and compare the results with the predictions of a numerical model. The aim of these experiments was to follow up an earlier experiment by Linke et al. [26] (for which the numerical modelling was performed by the author) with measurements on devices with conductance characteristics that were somewhat easier to model and interpret using Landauer-Büttiker formalism. The central result of both experiments is that asymmetric point contact devices can act as *quantum ratchets*, producing a net current when subjected to a symmetric square-wave source-drain voltage.

The ratchet system studied in [26] consisted of an array of asymmetric quantum dots realised by confining a two-dimensional electron gas in a GaAs/AlGaAs heterostructure to a channel defined by shallow wet etching. Eight periods of the ten dot array are shown in Figure 4.1. Another device consisting of just one period was also studied, and is shown in Figure 4.2.

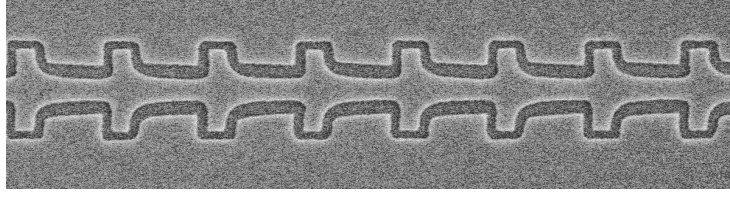


Figure 4.1: A scanning electron micrograph of device R10. The darker regions are etched lines defining the outline of the device. Electrons are confined to the central asymmetric channel, while regions to either side were used as side gates to adjust the width of the device electrostatically.

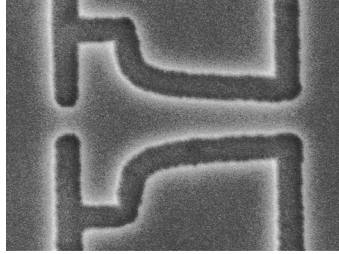


Figure 4.2: A scanning electron micrograph of R1. It is the same size as one period of the array shown in the previous figure.

The shape was chosen so that the confinement potential experienced by the electrons was an asymmetric sawtooth shape, as was also the case for the device D3 studied in this thesis.

The length of the devices ($1\text{ }\mu\text{m}$ per period) was much less than the length scales for elastic ($\sim 6\text{ }\mu\text{m}$) and inelastic ($\sim 10\text{ }\mu\text{m}$) scattering at the temperatures and voltages used in the experiment ($T < 4.2\text{ K}$, so $kT < 1\text{ meV}$, and $|eV_{sd}| < 1\text{ meV}$). The devices were rocked with a square-wave voltage (with a frequency of 191 Hz), which was 100% amplitude modulated (at a frequency of 17 Hz), with lock-in amplifiers used to measure the rectified current at the modulation frequency. These frequencies are low enough that the time between switches of the polarity are much larger than the characteristic time of electron energy-relaxation processes, so that the ratchet was in a station-

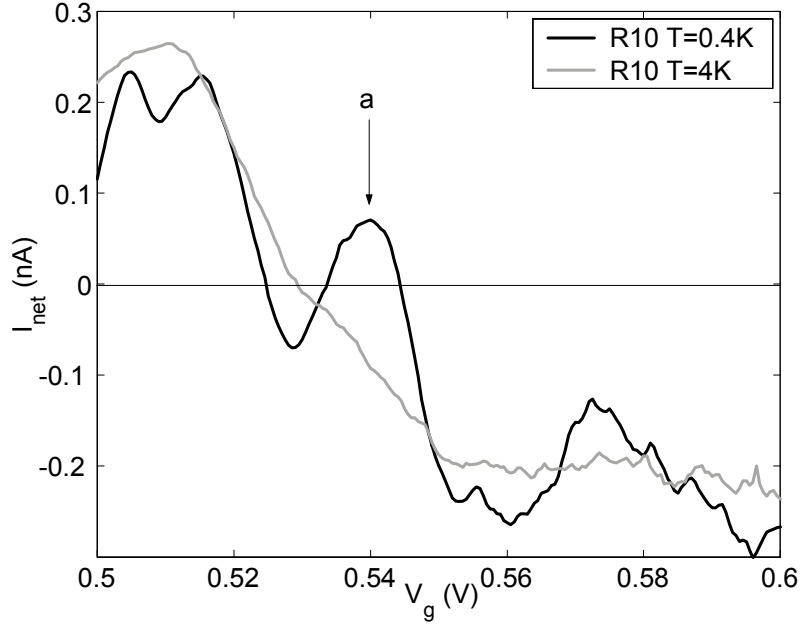


Figure 4.3: Net current as a function of gate voltage for the ten barrier device, R10, for two temperatures. The marker ‘a’ indicates an implicit reversal of the direction of the net current as a function of temperature.

ary state at all times (adiabatic rocking). Measurement of the net current was made in both ‘Forward’ and ‘Reverse’ configurations, with asymmetric gating. These measurements were then subtracted to remove effects due to circuit-induced asymmetry, according to the method described in Chapter 3. A major difference between the experiment described in this thesis and that in [26] is that in [26] the average, or net current by the ratchet over a number of AC square-wave cycles is measured directly via the current input on a lock-in amplifier. In this thesis the differential conductance is measured and compared for equal positive and negative DC source-drain voltages. This measurement technique is less direct, but means that extra information is collected, and so allows a more in-depth comparison with the numerical model developed by the author to assist in understanding the physical processes behind the operation of the quantum ratchet.

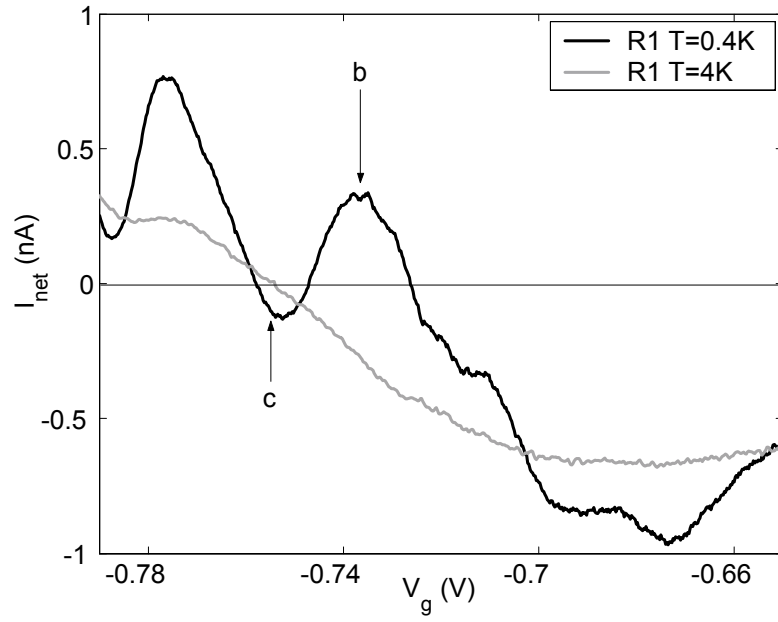


Figure 4.4: Net current as a function of gate voltage for the one barrier device, R1, for two temperatures. The markers ‘b’ and ‘c’ indicate implicit reversals of the direction of the net current as a function of temperature.

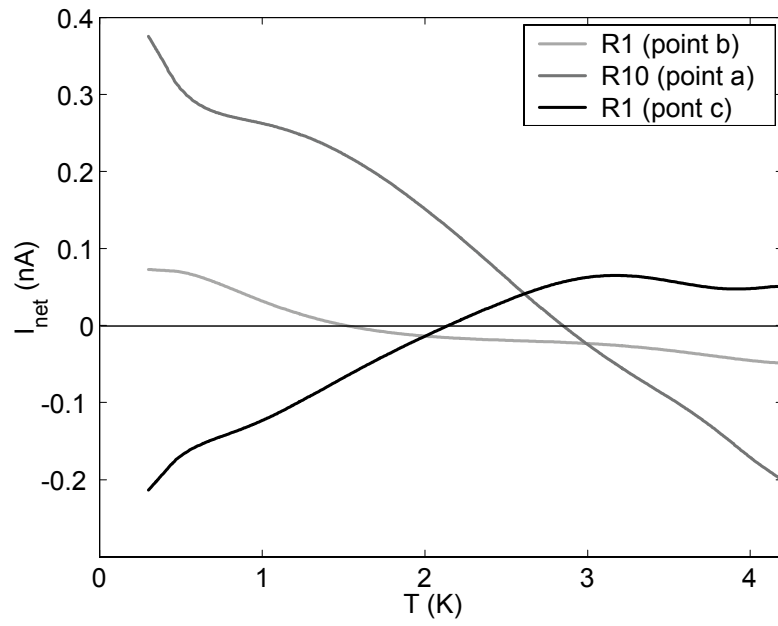


Figure 4.5: Net current measured as a function of temperature at points ‘a’, ‘b’ and ‘c’ shown in Figures 4.3 and 4.4, for a source-drain voltage amplitude of 1mV, showing explicit temperature reversals.

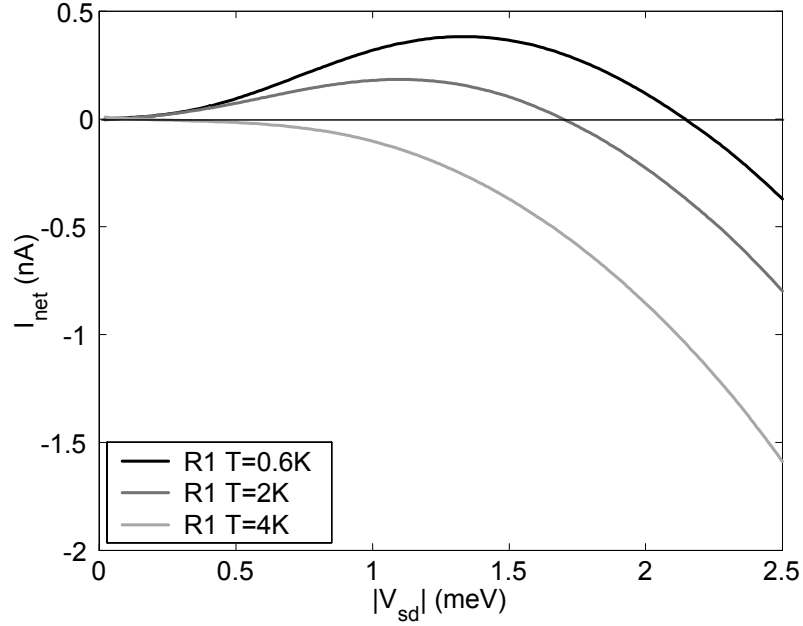


Figure 4.6: Net current as a function of source-drain voltage amplitude for the point ‘b’ in figure 4.4 for three different temperatures. Note that the reversal in the net current disappears with increasing temperature. The numerical model presented in §4.2 predicts this behaviour.

Figures 4.3 and 4.4 (data taken from [26]) show the measured net current as a function of the gate voltage for the ten- and one-period ratchets (called R10 and R1 in [26]) respectively. As for the devices already described in this thesis, the side gates are used to electrostatically tune the conducting width of R1 and R10. Figures 4.3 and 4.4 therefore show the current rectified by the ratchet as a function of increasing conducting width of devices R1 and R2. As the asymmetric potential is formed due to quantum confinement, increasing QPC width corresponds to lower potential barriers and increasing conductance. The dark lines show the net current measured at 0.4K and the lighter lines the net current measured at 4K with the amplitude of the square-wave rocking voltage being 1mV. Gate voltages at which other measurements were performed (and where a reversal of the net current occurs

with increasing temperature) are indicated with arrows and labels a (for R10) and b and c (for R1). Direct measurements of the reversal of the net current with increasing temperature of both devices were made at these gate voltages and at a rocking amplitude of 1mV, and these are shown in Figure 4.5. Figure 4.6 shows the net current measured as a function of the amplitude of the rocking voltage for the device R1, at the gate voltage denoted by the arrow labelled ‘b’ in Figure 4.4 for temperatures (from the top) of 0.6, 2 and 4K. Thus reversals in the direction of the net current were seen experimentally as a function of temperature, gate voltage and rocking amplitude.

As mentioned earlier, a numerical model of an asymmetric point contact was developed by the author to account for these reversals, and will be presented in the following sections.

4.2 Theory

This section will utilise the Landauer formalism for one-dimensional (1D) ballistic transport which was introduced in §2.2.3 to develop a numerical model of the experimental device. The purpose of this model is to provide insight into the physical processes which lead to net current reversals in rocked quantum ratchets for electrons.

As discussed in §2.1.2, a rocked ratchet is an asymmetric potential that is tilted periodically and symmetrically. A classical rocked ratchet produces a net current as the height of the asymmetric potential barrier is different when it is tilted up, compared to when it is tilted down. The distinguishing characteristic of a rocked ratchet in the *quantum* regime is that the probability of transmission over the barrier depends not only on the height, but also on the exact shape of the barrier, which changes with tilt direction. This dependence is due to the fact that electrons with energies less than the barrier height may be transmitted by tunnelling with a probability which depends sensitively upon the height *and* the width of the barrier, and electrons with energies higher than the height of the barrier may be reflected due to wave

reflection with a probability which depends upon how ‘sharp’ or steep the barrier is. These considerations, illustrated in Figure 4.7, lead to the possibility of the direction of the net current reversing as the relative contribution of tunnelling and wave-reflection processes change with variables such as the potential height, magnitude of rocking, and temperature.

The best way to understand what will happen for a particular asymmetric potential is to define the *difference* in the energy resolved transmission probabilities of electrons through the potential under opposite tilt directions (source-drain voltages of opposite sign), $\Delta\tau(E) = [\tau(E, +V_{sd}) - \tau(E, -V_{sd})]$. An example $\Delta\tau(E)$ curve is shown in Figure 4.8, along with the transmission probabilities it is derived from, $\tau(E, +V_{sd})$ and $\tau(E, -V_{sd})$. In addition, the transmission probability which would result if transmission was classical is also shown. This is simply zero transmission for all electrons with energies lower than the barrier height, and unity for electrons with energies higher than the barrier. If $\Delta\tau(E)$ changes sign as a function of energy, this indicates that electrons with some energies are more likely to be transmitted from left to right, for example, under symmetric rocking, while electrons of other energies are more likely to be transmitted in the opposite direction. This means that the overall direction of the net current depends upon the relative numbers of electrons going in each direction. Reversal of the direction of the net current can occur as the relative numbers of electrons travelling in each direction is altered by changing the barrier height, temperature or magnitude of the bias voltage.

The net current for the quantum ratchet is the average of the currents for positive and negative source-drain voltages

$$I_{net} \equiv \frac{1}{2}[I(+V_{sd}) + I(-V_{sd})] = \frac{e}{h} \int_{U_0}^{\infty} \Delta\tau(E) \Delta f(E, |V_{sd}|) dE \quad (4.1)$$

where the current under positive and negative source-drain voltages $I(+V_{sd})$ and $I(-V_{sd})$ is given by the Landauer equation 2.6, derived in §2.2.3, and where

$$\Delta f(E, |V_{sd}|) = 1 / \left\{ 1 + \exp \frac{E - \varepsilon_L}{kT} \right\} - 1 / \left\{ 1 + \exp \frac{E - \varepsilon_R}{kT} \right\}. \quad (4.2)$$

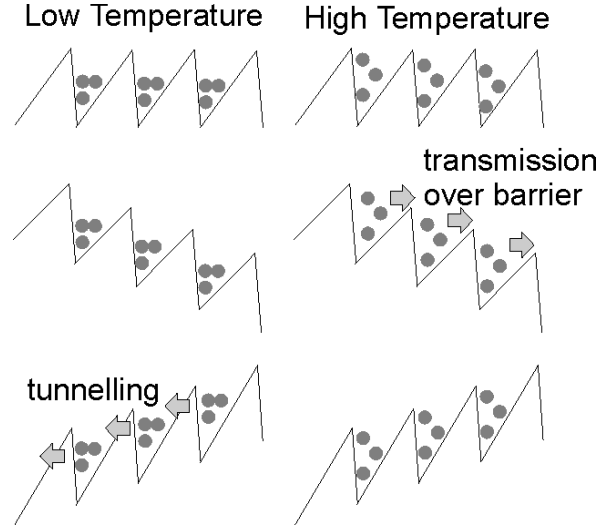


Figure 4.7: Illustration of the physical origin of net current reversals as a function of temperature in rocked quantum ratchets for electrons. In the centre, the change in shape of an asymmetric potential when it is tilted towards its steepest slope is shown. This tilt direction causes the barriers to become thicker, favouring the transmission of high energy electrons. The opposite tilt direction, shown for the bottom two potentials, causes the barriers to become thinner, and favours the transmission of low-energy electrons which have to tunnel. If the temperature is sufficiently low, there may be very few electrons with energies near the barrier top, and the net current will flow from right to left (in this example) as when the potential is tilted in this direction the barriers are thinnest. For higher temperatures, there will be more electrons with energies at and above the barrier tops. As the maximas are less ‘sharp’ in the middle figures, this tilt direction will cause less wave reflection of electrons at high energies and the net current will flow from left to right at high temperatures.

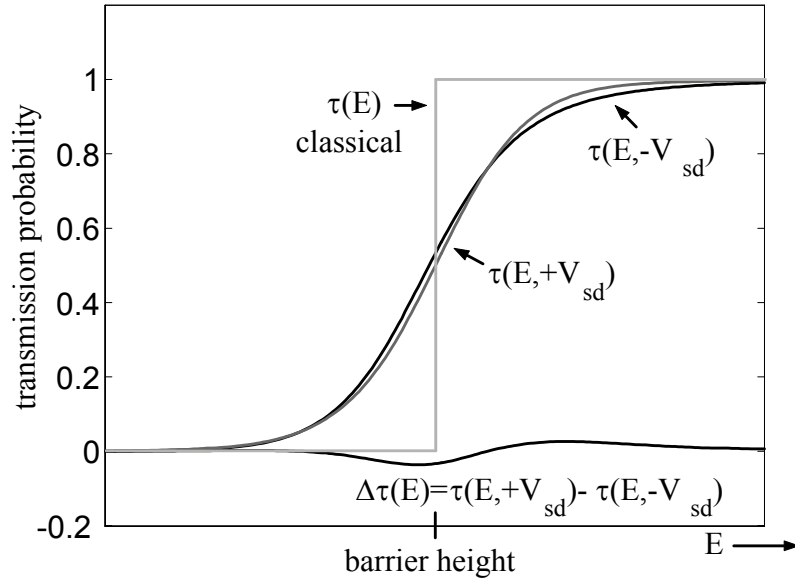


Figure 4.8: This figure shows the transmission probability as a function of energy for voltages of different sign for the asymmetric potential shown in Figure 4.10 (used here simply as an example of an asymmetric potential). The asymmetry of the potential results in a difference between these transmission probabilities, labelled $\Delta\tau$, which is non-zero, and changes sign with energy. The transmission probability for classical particles is also shown. This is zero for particles with energies lower than the barrier, and unity for particles with energies above the barrier.

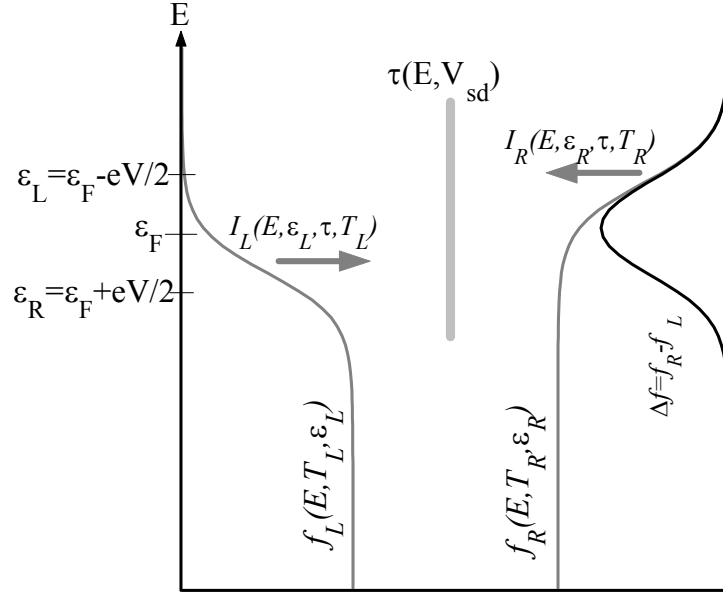


Figure 4.9: Two Fermi distributions are shown, the one on the right having a Fermi energy higher than that on the left. The current of electrons between the reservoirs is proportional to the difference between these two distributions, Δf , which is shown on the far right. The current is also proportional to the probability that electrons are transmitted between the reservoirs, τ , which in general is a function of energy as well as the sign and magnitude of the voltage across the constriction between the reservoirs.

Δf will be called the ‘Fermi window’ in this thesis. Physically, $\Delta f(E)$ gives the occupation of states (as a function of energy) which make a net contribution to transport due to the application of the source-drain voltage, and is shown on the far right in Figure 4.9. For convenience, it is assumed in the model that half of the source-drain voltage is applied to each side of the barrier. While in the experiment one side of the device was set to ground, there is no physical difference between the two situations as only differences in voltage are physically meaningful (this is simply gauge invariance). One consequence of applying the voltage in this way is that the Fermi window is centred on the equilibrium ($V_{sd} = 0$) Fermi energy, ϵ_F . Changing the Fermi

energy in the model thus entails moving the centre of the Fermi window.

4.3 Numerical Model

Landauer theory allows calculation of the current as long as the transmission probability is known. This section will describe the process undertaken to calculate $\Delta\tau(E)$ and thus to calculate I_{net} as a function of ε_F , $|V_{sd}|$, and T . There are a number of steps involved in the calculation of $\Delta\tau(E)$:

1. A model for the shape of the potential experienced by the electrons in the experimental devices must be developed.
2. Assumptions must be made as to how the source-drain voltage is distributed across the potential.
3. The transmission probability for the particular potential and voltage drop is then calculated via numerical solution of the Schrödinger equation.

Once the transmission probability of the potential is calculated for both positive and negative source-drain voltages, the net current is easily calculated via Equation 4.1, and the results are shown at the end of this section. In §4.4 these calculations are compared with experimental data from the asymmetric device D3.

4.3.1 Modelling the potential

The shape of the curved part of the lithography in device D3 (see Figure 3.2) is given by $W_y(x) = \pm(a/\sqrt{x} - b)$ for $0.1\mu m < x < 2.5\mu m$, where, lithographically, $a = 1.5\mu m^{\frac{3}{2}}$ and $b = 0.75\mu m$, and x is the direction of transport through the device. This particular lithographic shape was chosen as it ideally produces a sawtooth potential barrier in the case where $b = 0$. This can be seen by noting that the energy of a particle due to spatial

confinement (for the lowest subband) in the y-direction perpendicular to the direction of transport is given by:

$$U = \frac{\hbar^2 k_y^2}{2m^*} \quad (4.3)$$

The wavevector $k_y = 2\pi/\lambda$, where the wavelength $\lambda = 2W_y(x)$, and m^* is the effective mass of electrons in GaAs. It then follows that the confinement potential of the device is expected to be (for $b = 0$):

$$U(x) = \frac{h^2}{8a^2m^*}x \quad (4.4)$$

The actual potential shape experienced by the electrons in the experiment is affected by a number of additional factors, which include:

1. The smoothing of the above shape which occurs due to the finite width of the line created by the SEM and the subsequent etching process.
2. The smoothing of the lithographic shape due to charge buildup/depletion around the etched lines.
3. The application of a gate voltage.
4. The application of a source-drain voltage $\pm V_{sd}$.

Exact determination of the shape of the actual experimental potential would require a three-dimensional, self-consistent solution to the Schrödinger and Poisson equations. These equations model how electrons in the device respond to a potential imposed on them, and how the resulting change in electron density affects the potential, and so on. This is usually only attempted in quite ‘simple’ situations (see, for example, [63]). The approach used in this model was to make an ‘educated guess’ about the potential shape by numerically smoothing a sawtooth potential based on the lithography, and the potential thus constructed is shown in Figure 4.10 with a large (for clarity) source-drain voltage of ± 4 mV applied as described in §4.3.2. The sensitivity of the qualitative features of $\Delta\tau(E)$ to changes in the shape

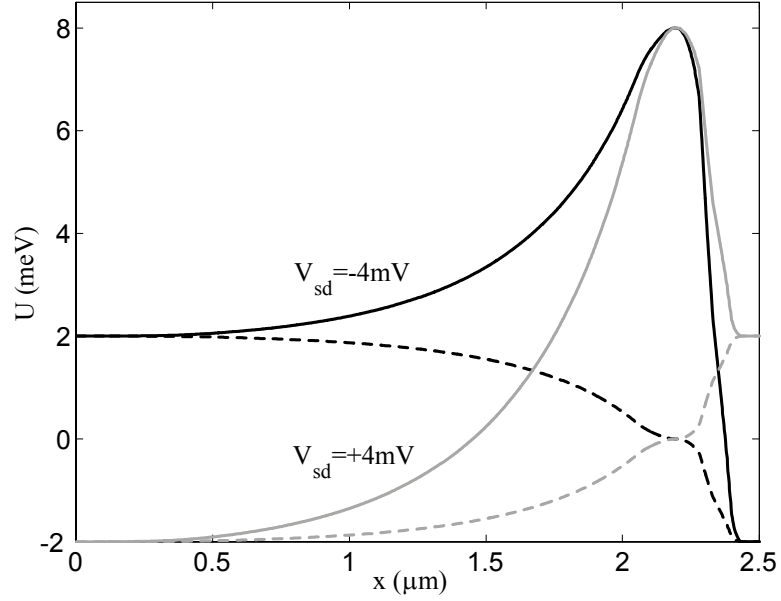


Figure 4.10: The asymmetric potential shape used in the numerical model, with an applied voltage of ± 4 mV. This voltage is much larger than that used in the experiments (± 0.5 mV) to emphasise the change in shape of the barrier under a sign change in the source-drain voltage. The spatial distribution of the 4 mV for each case is shown as dashed lines. Note that if half the potential drop is applied before and after the maxima of the potential, as has been done here, then the height of the potential remains constant. This has the consequence that all differences in the transmission probability between positive and negative voltages is due solely to quantum effects such as tunnelling and wave-reflection.

of the asymmetric potential is examined in Appendix D. It was found that while the relative size of features in $\Delta\tau(E)$ is dependent upon the amount of asymmetry present in the potential, the general shape of $\Delta\tau(E)$ is reasonably insensitive to the exact potential shape chosen for modelling.

4.3.2 Modelling the voltage drop

As a full self-consistent calculation of the shape of the potential and voltage drop has not been performed, for the reasons outlined in the section above, a decision must be made as to how the voltage is distributed across the potential barrier chosen for modelling.

The voltage V_{sd} was distributed across the potential in proportion to the local derivative of the potential, so that

$$\pm v_{sd}(x) = \pm |V_{sd}| \left[\frac{f(x)}{f(L)} - \frac{1}{2} \right] \quad (4.5)$$

where

$$f(x) = \int_0^x \left| \frac{dU(x')}{dx'} \right| dx' \quad (4.6)$$

Here $v_{sd}(0) = |V_{sd}|/2$ and $v_{sd}(L) = -|V_{sd}|/2$, where L is the length of the barrier. The shape of $v_{sd}(x)$ is shown in Figure 4.10 for the potential barrier used in the model. The reasons for choosing this method of distributing the voltage over the barrier, rather than using a linear voltage drop, are twofold. Firstly, it seems reasonable that the amount of voltage dropped at a particular place along a potential barrier is proportional to the gradient of the potential is at that point [27, 28, 64], as wave reflection is more pronounced for steep barriers. The second reason for choosing this voltage drop was that it results in a constant barrier height. If the barrier height varies with the sign of the source-drain voltage applied, as it would with a linear voltage drop (see Figure 4.7), then the current would be much greater for one polarity than the other. If such an effect occurred in the experimental devices, reversals in the direction of the net current, such as were seen in [26], would be very

difficult to observe. This is because the significant contribution to the net current due to classical effects would swamp the dependence of the current on the precise shape of the barrier, which arises due to the quantum effects of tunnelling and wave-reflection. As current reversals are clearly seen in the experimental data of [26] and that shown in this thesis for device D3, this is strong evidence in favour of using a voltage drop which ensures that the barrier height remains constant. It follows from this choice that all finite net current in the model arises from quantum, not classical effects.

4.3.3 Calculation of the transmission probability

Once a barrier and potential drop had been chosen, the transmission probability was calculated by numerical solution of the Schrödinger equation using Numerov's method [65] for solving second order differential equations with no first-order derivative term. Details of the method are given in Appendix D. In the case of a symmetric point contact, the saddle-point potential model [66, 42] (see Appendix E for a very brief outline) is usually used to analytically calculate the transmission probability. Given that the saddle-point model does not allow for the shape of the potential to change with the sign (or magnitude) of the source-drain voltage, a feature crucial to the operation of a rocked quantum ratchet, in this model the transmission probability of the asymmetric quantum point contacts will be calculated numerically.

4.3.4 Numerical Results

The net current and differential conductance as a function of ε_F , $|V_{sd}|$, and T can be calculated numerically from the transmission probability difference, $\Delta\tau(E)$, of the model asymmetric potential, shown in Figure 6.2, and the Fermi 'window', $\Delta f(E, \varepsilon_F, T)$ also shown in Figure 6.2 for three values of temperature.

Results will be presented simultaneously for the net current, I_{net} , (Equation 4.1), the quantity measured in the experiments of [26], and the net

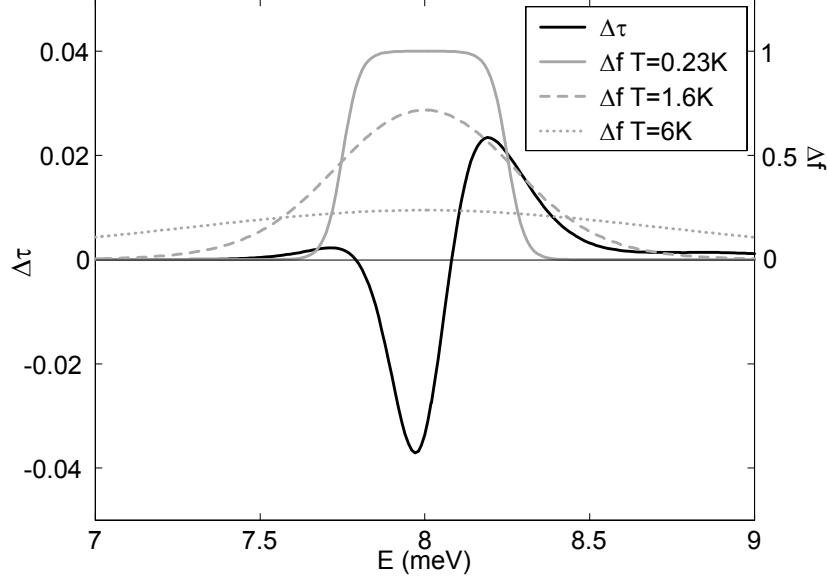


Figure 4.11: The left vertical axis shows $\Delta\tau$ for the potential in the numerical model. It is first positive, indicating the transmission probability for positive V_{sd} is larger than for negative V_{sd} . This behaviour for energies below the barrier height can be understood from Figure 4.10, where it can be seen that for positive V_{sd} the barrier is narrower, so that electrons can tunnel more easily than for negative V_{sd} . $\Delta\tau$ changes sign and becomes negative for energies around the barrier height, as electrons with these energies are more readily reflected from narrower and sharper barriers. It then changes sign again to be positive for energies much higher than the barrier height. Some discussion of the effect of potential shape on the shape of the transmission probability is given in Appendix C. The right vertical axis shows the Δf ‘window’, discussed in §4.2, for a Fermi energy equal to the barrier height of 8meV, for temperatures of 0.3K, 1.6K and 6K. The net current as a function of Fermi energy is the equivalent of the mathematical convolution of the $\Delta\tau(E)$ curve and the $\Delta f(E, \varepsilon_F, T)$ window.

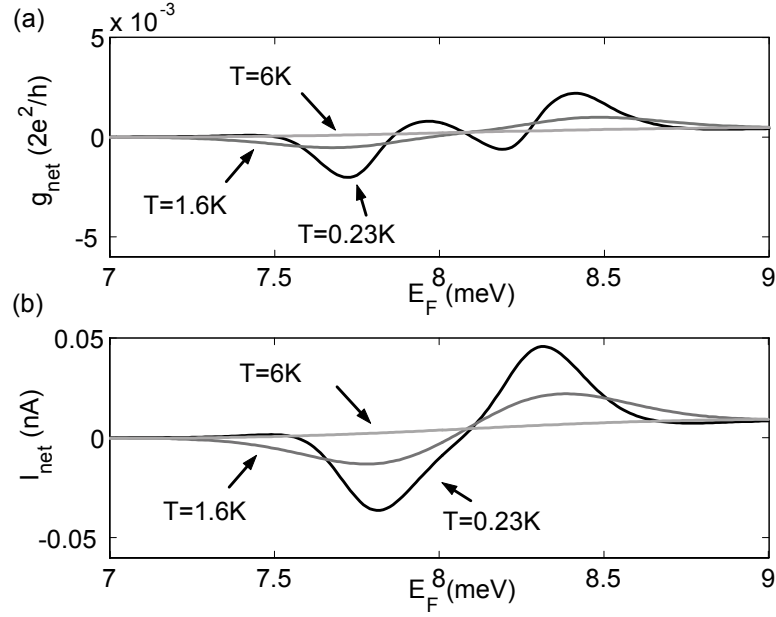


Figure 4.12: (a) The calculated net differential conductance as a function of Fermi energy for $|V_{sd}| = 0.5\text{mV}$, for temperatures $T = 0.3\text{K}$, $T = 1.6\text{K}$ and $T = 6\text{K}$. (b) The net current, parameters as for (a). The main feature to note is that the shape of the net current at $T = 0.3\text{K}$ is very similar to the $\Delta\tau$ curve shown in Figure 6.2. This feature is important for the analysis of the experimental data as it shows that by measuring the net current at a low temperature and source-drain voltage, an accurate picture of the shape of the $\Delta\tau$ curve of the experimental device can be obtained.

differential conductance, $g_{\text{net}} = dI_{\text{net}}/dV_{sd}$, which was measured in the experimental work of this thesis. g_{net} is calculated in the model simply by taking the derivative of Equation 4.1. Note that the model does not include the effects of CIA.

Figure 4.12 shows the calculated net differential conductance, g_{net} , and net current, I_{net} , as a function of the Fermi energy of the electrons, for a barrier height of 8mV and $|V_{sd}| = 0.5\text{mV}$. Sweeping the side-gate voltage in the experiment changes the barrier height relative to the Fermi energy, and this measurement is therefore approximately analogous to the situation

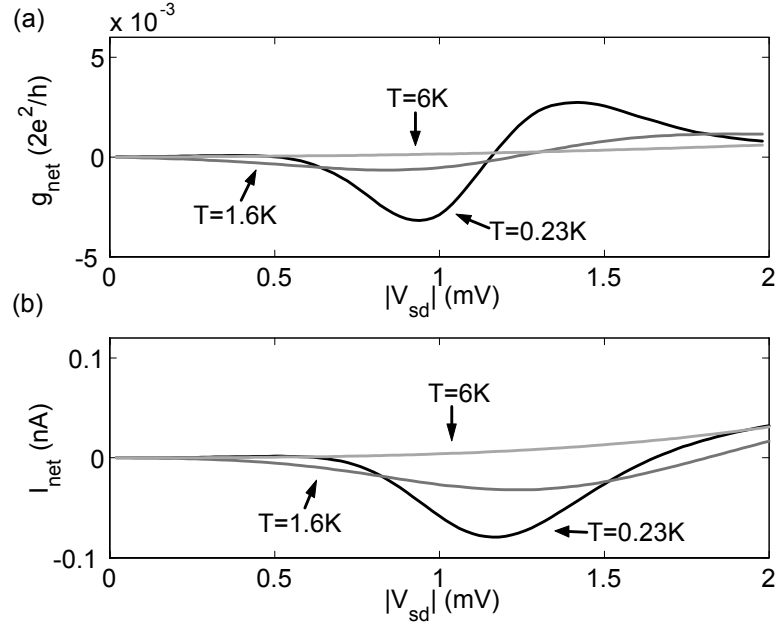


Figure 4.13: The model net differential conductance and net current as a function of $|V_{sd}|$ for a Fermi energy of $\varepsilon_F = 7.5 \text{ meV}$.

in the numerical model, where the barrier height is kept constant and the Fermi energy changed. Figure 4.12 may thus be compared with Figures 4.3, 4.4 and 4.16. The main things to note in these figures is that the shape of I_{net} strongly resembles that of the $\Delta\tau$ curve in Figure 6.2, and that this shape becomes ‘smeared-out’ with increasing temperature, as discussed at the end of §4.2.

Figures 4.13 and 4.14 show calculated net differential conductance and net current as a function of the magnitude of the DC bias voltage for $\varepsilon_F = 7.5 \text{ meV}$, $\varepsilon_F = 8.0 \text{ meV}$ and $\varepsilon_F = 8.1 \text{ meV}$, each for a range of temperatures. In Figures 4.13 and 4.14, the g_{net} curves shown in (a) are the derivatives of the I_{net} curves shown in (b). The purpose of Figures 4.13 and 4.14 is to illustrate the effect on the differential conductance and net current of an increase in the width of the Fermi window. Figure 6.2, shows the fermi window, $\Delta f(E, \varepsilon_F, T)$, and the $\Delta\tau(E)$ curve. Centering the window on

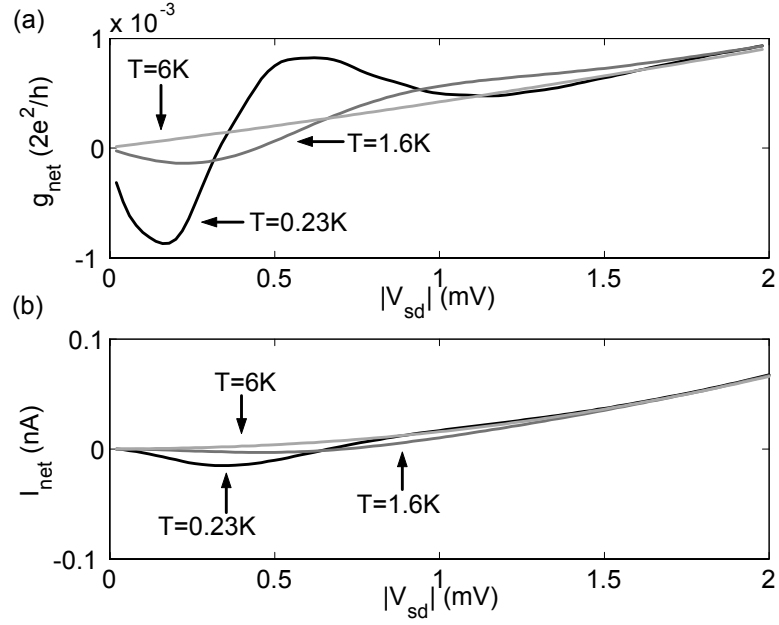


Figure 4.14: The model differential conductance and net current as a function of $|V_{sd}|$ for a Fermi energy of $\varepsilon_F = 8.0$ meV. As for figure 4.13, this plot can be understood by examining the effect of increasing the width of the Fermi window in figure 6.2. As the window initially samples the $\Delta\tau$ curve where it is negative in this case, the net current in this figure begins negative and then changes sign as the width of the window increased with increasing $|V_{sd}|$.

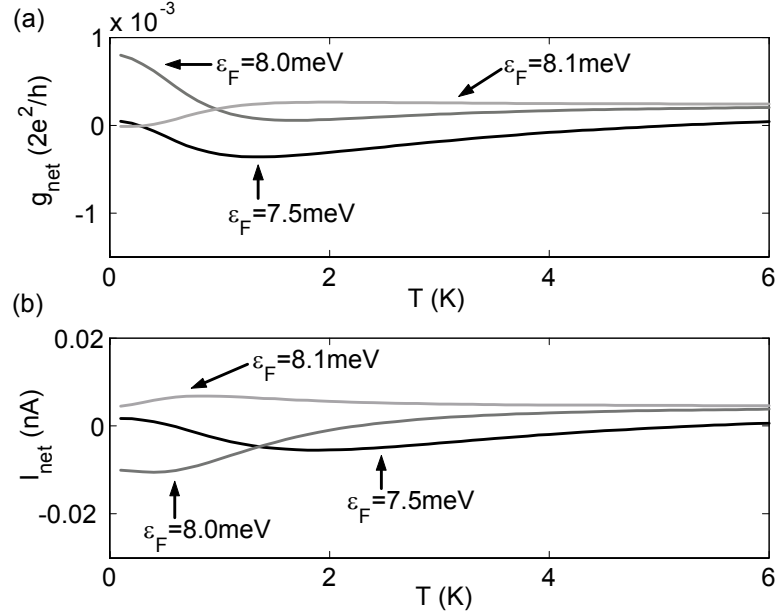


Figure 4.15: The model differential conductance and net current as a function of temperature for $|V_{sd}| = 0.5$ mV and $\varepsilon_F = 7.5, 8.0$ and 8.1 meV. The polarity of g_{net} and I_{net} at $T = 0.3$ K, 1.6 K and 6 K can be matched with those of g_{net} and I_{net} at $|V_{sd}| = 0.5$ mV in figures 4.13, 4.14. Along with the present figure, these illustrate how increasing either the source-drain voltage or the temperature mean that the Fermi window averages over more of the $\Delta\tau$ curve. Net current reversals occur when the integrated area of $\Delta\tau$ curve under the Fermi window changes sign.

an energy of 7.5 meV and then increasing the width results first in a very small positive net current, which turns negative when the window samples the minimum of the $\Delta\tau$ curve, and then positive again as it includes the entire curve. Higher temperatures contribute to the averaging over the $\Delta\tau$ curve, as the Fermi window is more smeared out at higher temperatures.

Figure 4.15 shows the calculated net differential conductance and net current as a function of temperature for the same Fermi energies as the previous figures, for $|V_{sd}| = 0.5$ mV. When the Fermi energy is placed at 7.5 meV, the model predicts two reversals of the net current as a function of temperature. The first at approximately 0.5 K, when the Fermi window (see

figure 6.2) averages over as much of the negative region of the $\Delta\tau$ curve as it does the first positive area, and the second at approximately 5.5K when the Fermi window has expanded sufficiently to sample the second positive area. The net current tends to a positive value at high temperatures for all values of the Fermi energy, as the net area of the $\Delta\tau$ curve is positive.

The central ideas of the model can be summarised as follows:

1. The difference in the transmission probability of the ratchet potential under source-drain voltages of opposite sign, $\Delta\tau$, changes sign as a function of energy. This is a purely quantum effect due to the change in the shape of the potential under source-drain voltages of opposite sign affecting tunnelling and higher energy electrons in different ways.
2. The Fermi window determines the energy spectrum of electrons participating in transport, and therefore determines what energy range of the $\Delta\tau$ curve will be integrated over, and so determines the sign of the net current.
3. As a result of points 1 and 2, it follows that changing the Fermi energy, source-drain voltage amplitude or temperature can cause net current reversals.

4.4 Experimental Data

All data shown in this section is from device D3. The effects of circuit-induced asymmetry have been removed according to the method described in §3.2.2. The technique used involves measuring the differential conductance of the device in both ‘Forward’ and ‘Reverse’ source-drain configurations. These measurements are then subtracted to remove the effects of CIA according to Equation 6.2:

$$g_{net}(|V_{sd}|) \equiv g(+V_{sd}) - g(-V_{sd}) = 0.5 [g_{Fpos} + g_{Rneg} - g_{Fneg} - g_{Rpos}] \quad (4.7)$$

where small g denotes differential conductance $g = dI/dV_{sd}$. This method was used as symmetric gating had not yet been developed as a technique for removing CIA at the time the following data was taken. The only net current data presented was calculated numerically from the differential conductance when this was measured as a function of the source-drain voltage. This is in contrast to the data reported in [26], in which the net current was measured directly as a function of magnitude of the source-drain voltage, temperature and gate voltage through use of an AC, rather than DC, source-drain voltage.

Three data sets will be presented, with selected data plotted with numerical results from the model for direct comparison.

1. Net differential conductance as a function of the gate voltage for $|V_{sd}| = 0.5 \text{ mV}$ and $T = 0.3, 1.6$ and 6 K .
2. Net differential conductance and net current as a function of the magnitude of the source-drain voltage for $T = 0.3, 1.6$ and 6 K , at $V_g = 0.7 \text{ V}$ and $V_g = 1.0 \text{ V}$.
3. Net differential conductance as a function of temperature for $|V_{sd}| = 0.5 \text{ mV}$ at $V_g = 0.7 \text{ V}$ and $V_g = 1.0 \text{ V}$.

4.4.1 Net Differential Conductance versus Gate Voltage

Figure 4.16 (a) shows the net differential conductance of device D3 for $|V_{sd}| = 0.5 \text{ mV}$ and $T = 0.3 \text{ K}$, determined via Equation 4.7 from the differential conductance for positive and negative source-drain voltages, which are shown in Figure 4.16 (b). The net differential conductance measurement was checked for repeatability by heating the sample up to 6 K then cooling it back to the base temperature of 0.3 K and repeating the measurement. The results, shown in Figure 4.17, establish that the essential shape of the net differential conductance is reproducible, and also show that heating and cooling the

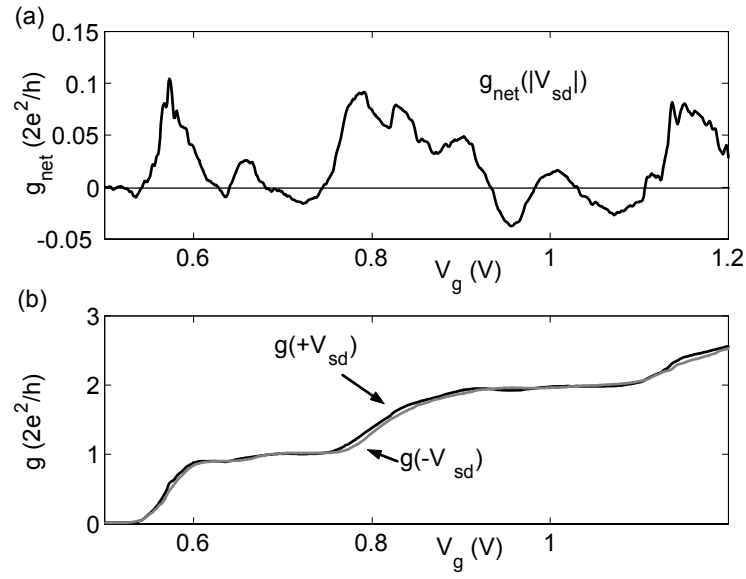


Figure 4.16: (a) $g_{\text{net}}(|V_{sd}|)$ (b) $g(+V_{sd})$ and $g(-V_{sd})$ as a function of gate voltage for $V_{sd} = 0.5$ mV. Note that the main difference between the sweeps is on the rise to the plateaus.

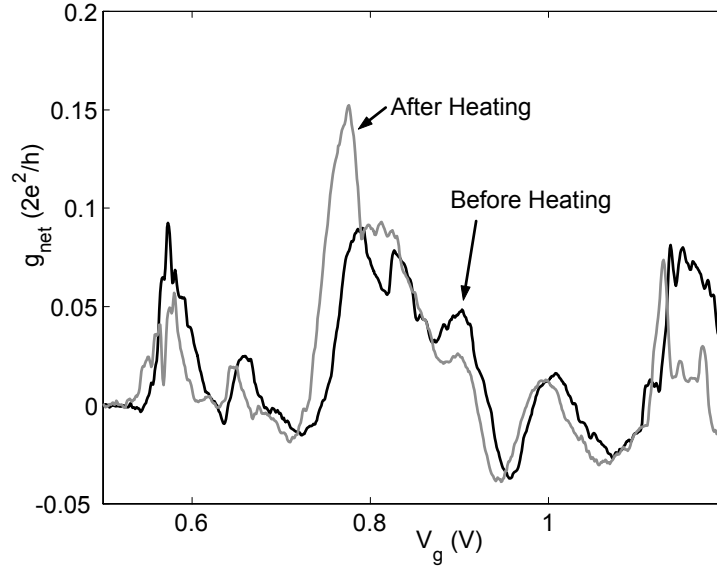


Figure 4.17: A comparison of the net differential conductance curves obtained before and after heating to 6K and then returning to base temperature (0.23K), and is likely to be due to the time delay between taking the sweeps. The gate voltage was always swept in the same direction, so the shift between the curves is not a result of hysteresis, but is rather a linear shift of the conductance curve to lower values of gate voltage. This kind of shift is not unusual in these kinds of devices. The important point to note is that all the main features of the curve are reproducible.

sample can cause a shift in the gate voltage at which particular conductance features appear.

The behaviour of the net differential conductance with temperature is shown in Figure 4.18. As predicted by the model, $g_{net}(|V_{sd}|)$ at higher temperatures is essentially a 'smeared-out' version of $g_{net}(|V_{sd}|)$ at lower temperatures. This is due to the broadening of the Fermi window with increasing temperature, and results in a change in sign of the net differential conductance at some gate voltages, such as those at $V_g \approx 0.7$ V and $V_g \approx 1.0$ V, marked A and B in Figure 4.18. There has also been some shifting in features

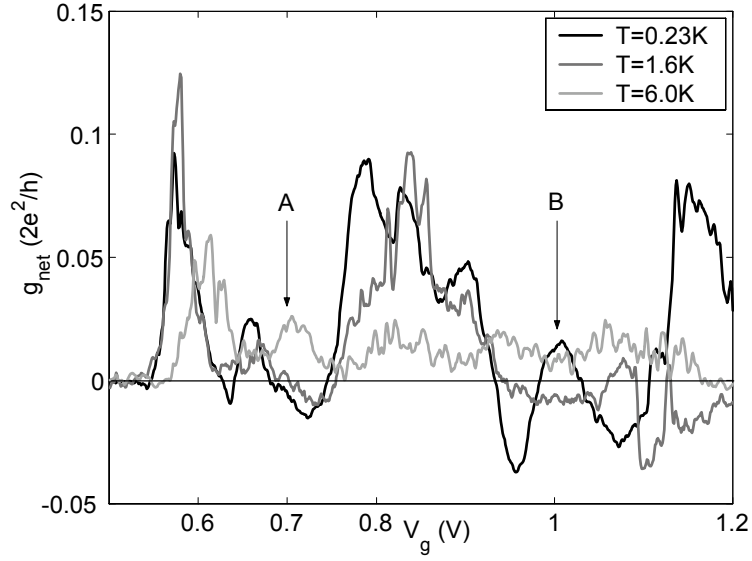


Figure 4.18: The experimental net differential conductance for temperatures 0.3K, 1.6K and 6K, showing the averaging effect of increasing temperature which was predicted by the model. The markers ‘A’ and ‘B’ indicate gate voltages at which source-drain voltage and temperatures sweeps were taken.

such as the initial peak (for the 6 K curve), due to the unavoidable time-lapse between sweeps.

To examine the relationship of the experimental results with those of the model in more detail, the first two conductance modes of the experimental measurements ($V_g = 0.5 \text{ V}$ to $V_g = 0.68 \text{ V}$, and $V_g = 0.68 \text{ V}$ to $V_g = 1.03 \text{ V}$) are plotted in Figure 4.19 adjacent to the net differential conductance predicted by the model. Firstly, it can be seen that the first two conductance modes of D3 are qualitatively very similar, each showing an initial small negative minimum followed by a large positive maximum, and a further small minimum and maximum, of similar magnitude. This demonstrates that the physics which underlies the shape of the curve is repeated for each conductance mode. The net differential conductance predicted by the model also shows the same qualitative behavior, with two maxima and minima of the same sign as those of the experiment, although the magnitude and spacing

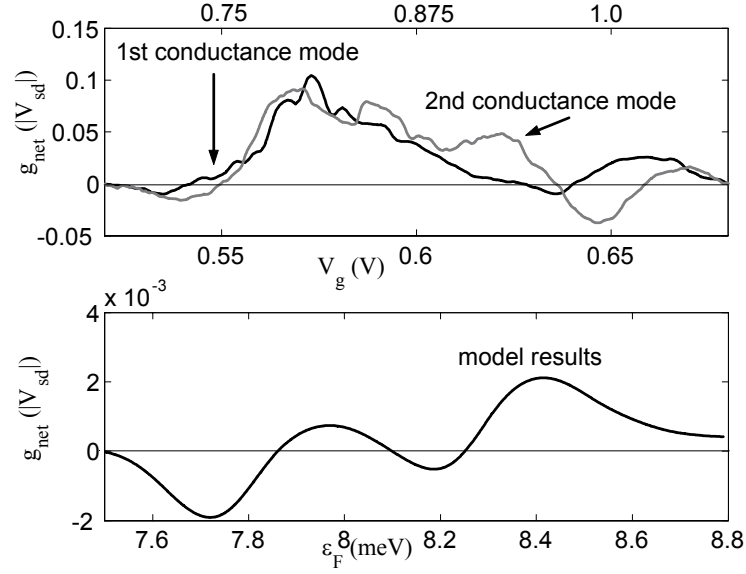


Figure 4.19: Comparison of the measured net differential conductance as a function of side-gate voltage and that predicted by the numerical model as a function of Fermi energy. Similar features are seen in both, two negative minimas between two positive maximas. The magnitudes of the first minima in the experiment and model are comparable, 0.01 and $0.002 \, 2e^2/h$ respectively. The magnitudes of the remaining features are much larger in the experimental data than in the numerical model. As mentioned in the text, this is likely to be due to the existence of larger asymmetry in the actual potential experienced by the electrons than was used in the model.

of these features is not exactly reproduced by the modelling. As it is unlikely that the shape of the barrier chosen for the modelling is exactly the same as that experienced by the electrons in the experimental device, and the relationship between gate voltage in the experiment and Fermi energy in the model is not linear, it is expected that this might lead to differences in the relative magnitudes and spacing of the features in the differential conductance.

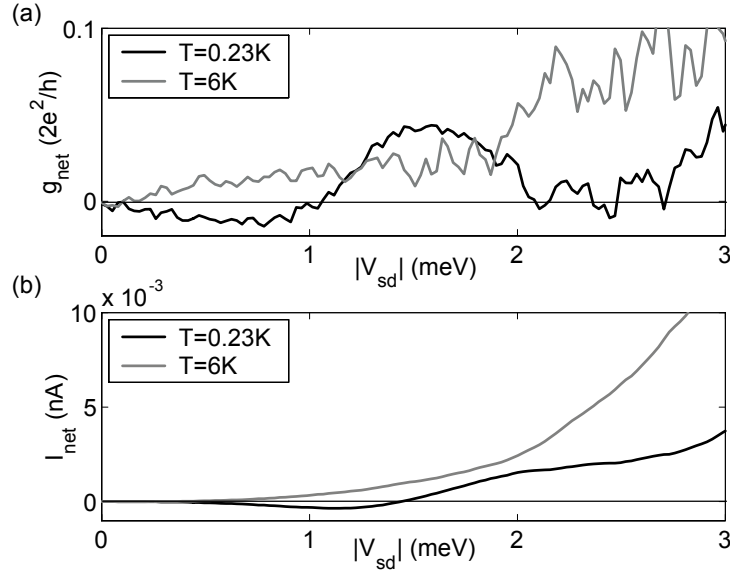


Figure 4.20: (a) A net differential conductance sweep versus source-drain voltage amplitude for $V_g = 0.7\text{ V}$ and for temperatures of 0.23 K and 6 K (b) The corresponding net current, calculated from the information in (a).

4.4.2 Net Differential conductance versus Source-drain Voltage

Figures 4.20 and 4.21 (a) show the net differential conductance and (b) the net current measured as a function of the magnitude of $|V_{sd}|$ at a gate voltages of 0.7V and 1.0V for a range of temperatures. The gate voltages at which these sweeps were measured are shown in Figure 4.18 with the markers ‘A’ and ‘B’. The behaviour with temperature in Figure 4.20, is consistent with that expected from Figure 4.18 (the behaviour in 4.21 is also consistent, but not as clear). At a source-drain voltage of $V_{sd} = 0.5\text{ mV}$ the differential conductance is negative, but becomes positive for a temperature of 6 K. This change is associated with a reversal of the direction of the net current, shown in (b), at a source-drain voltage of $\sim 1\text{ mV}$. Such net current reversals were seen in different devices in [26], and were shown in Figure 4.6 for comparison.

Figure 4.22 directly compares the experimental results for a gate voltage

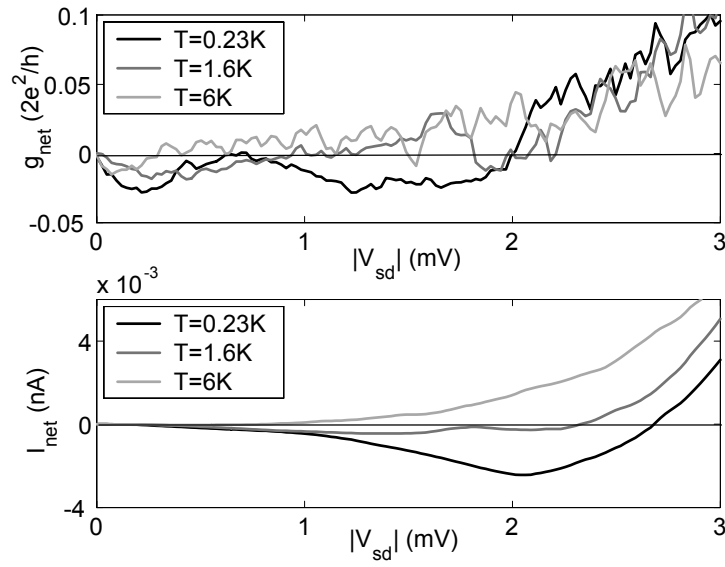


Figure 4.21: (a) A net differential conductance sweep versus source-drain voltage amplitude for $V_g = 1.0V$ for temperatures of 0.23K, 1.6K and 6K (b) The corresponding net current, calculated from the information in (a).

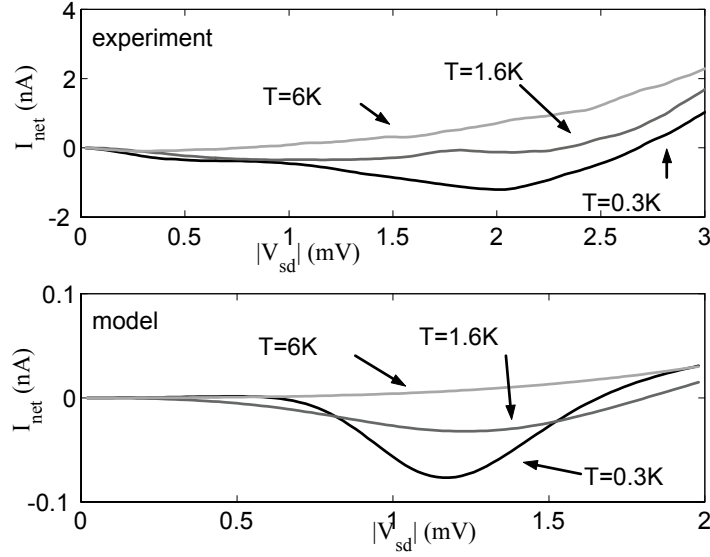


Figure 4.22: The top figure shows the net current calculated from the experimentally measured net differential conductance from Figure 4.21. The bottom figure shows the net current predicted by the model (c.f. Figure 4.13). The qualitative behaviour observed in the experimental data is very well reproduced by the numerical model.

of 1V and the model results for a Fermi energy of 8.1meV for temperatures $T = 0.23, 1.6$ and 6 K. It can be seen that again the model results show good qualitative agreement with the experimental results, but differ in the magnitude of net current observed, as was the case for the net differential conductance versus gate voltage results.

4.4.3 Net Differential Conductance versus Temperature

Figures 4.23 and 4.24 show sweeps of the differential conductance with temperature, taken at gate voltages $V_g = 1.0$ and 0.7V (points B and A respectively in figure 4.18) and for a source-drain voltage amplitude of $|V_{sd}| = 0.5\text{mV}$. Despite the noise in the data, these are shown as reversals in the net

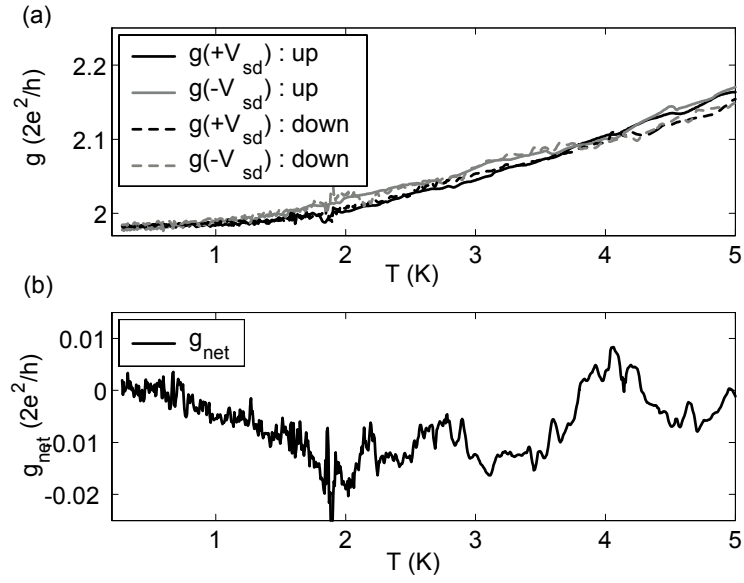


Figure 4.23: (a) g_{pos} and g_{neg} measured for both an upsweep and a downsweep of temperature for a gate voltage of $V_g = 1.0V$ and a source-drain voltage amplitude of $|V_{sd}| = 0.5mV$. It can be seen that the up and down sweeps are quite consistent. (b) g_{net} for the parameters in (a). The data from the up and down sweeps was averaged to produce this plot.

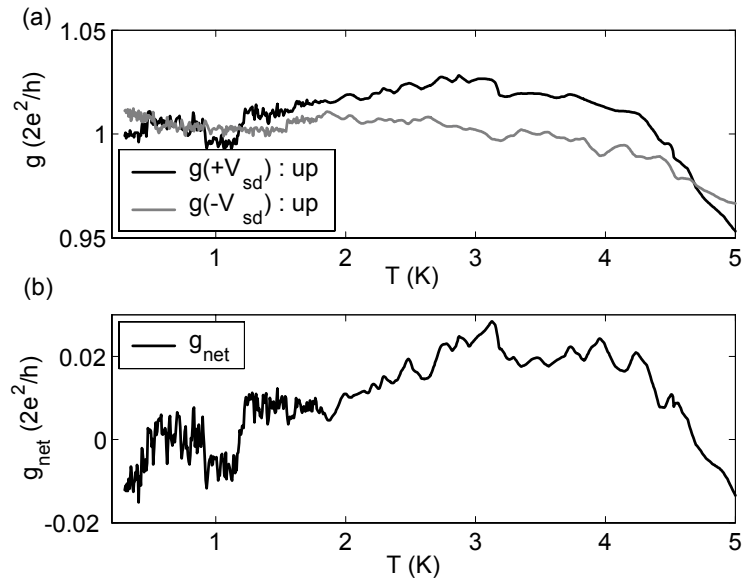


Figure 4.24: (a) g_{pos} and g_{neg} measured for a gate voltage of $V_g = 0.7\text{V}$ and a source-drain voltage amplitude of $|V_{sd}| = 0.5\text{mV}$. Time constraints in measuring this data meant that only upsweeps were taken. (b) g_{net} for the parameters in (a).

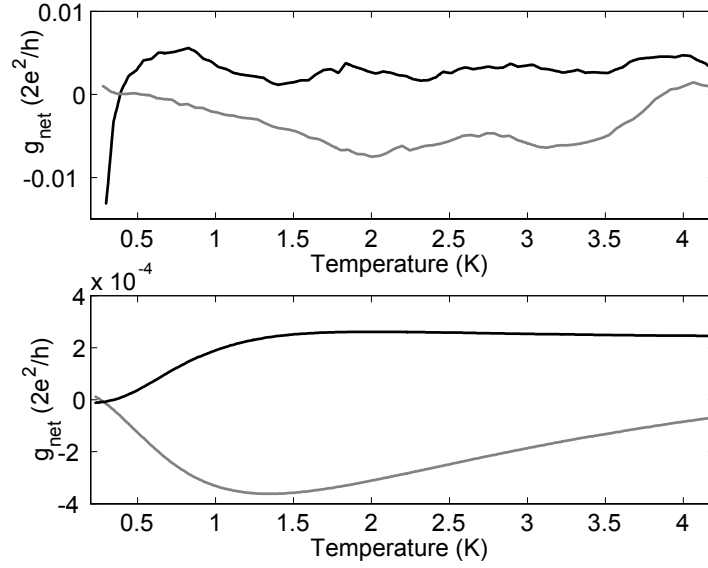


Figure 4.25: Comparison of the experimentally measured net differential conductance (top) and that predicted by the numerical model (bottom) as a function of temperature for $V_g = 0.7 \text{ V}$ and $V_g = 1.0 \text{ V}$, and $\varepsilon_F = 7.5 \text{ meV}$ and $\varepsilon_F = 8.0 \text{ meV}$ respectively. It can again be seen that the model predicts the general behaviour of the experimental data.

current with temperature are generally considered to be a hallmark of quantum behaviour in ratchets. They show explicit reversals in the net differential conductance of the device with temperature. Finally, the *smoothed* net differential conductance for $V_g = 0.7 \text{ V}$ and $V_g = 1.0 \text{ V}$ are compared directly with the net differential conductance predicted by the model for Fermi energies $\varepsilon_F = 7.5$ and 8.1 meV . As is the case for the previous data and model comparisons, there is good qualitative agreement but an order of magnitude difference in the size of the features.

4.5 Conclusions

The main ideas of this chapter can be summarised as follows:

1. The probability of tunnelling and wave-reflection of electrons through and from a barrier is very sensitive to its precise shape. As the shape of an asymmetric potential changes under source-drain voltages of opposite sign, the transmission probability as a function of electron energy is different for the two cases.
2. The difference between the transmission probabilities for positive and negative source-drain voltages, $\Delta\tau(E)$, changes sign as a function of energy. This occurs because the change in shape of the potential upon changing the polarity of the source-drain voltage affects the transmission of electrons in particular energy ranges differently, suppressing transmission in some ranges while enhancing probability of transmission in other ranges.
3. There are two important predictions of the numerical model which have been shown to be consistent with the experimental data. Firstly, that the features of the net current and differential conductance as a function of Fermi energy are determined by the shape of $\Delta\tau(E)$. Secondly, that these features are progressively smeared out with increasing temperature and source-drain voltage magnitude.
4. The data was measured on devices of different design and origin to those of Linke et al. [26], and show that the existence of net current reversals as a function of temperature, gate voltage and source-drain voltage amplitude in mesoscopic quantum electron ratchets is a robust effect, not limited to particular devices or measurement setups.

Part II

The Thermodynamics of Energy Selective Electron Heat Engines

Chapter 5

Introduction to Electron Heat Engines

The second and main part of this thesis is entirely theoretical. Chapter 6 is an exploration of the heat-pumping abilities of quantum ratchets. It covers numerical calculations of the heat pumped by the asymmetric quantum point contact (QPC) studied in the first part of the thesis, along with that pumped by an asymmetric double barrier ratchet potential through which resonant tunnelling occurs, leading to sharp features in $\tau(E)$. The latter is determined to be much more efficient at pumping heat than the asymmetric QPC potential, to the extent that it exhibits refrigeration of one electron reservoir. Chapter 6 can be viewed as motivating Chapter 7, which examines both analytically and numerically the properties of idealised energy selective electron heat engines and refrigerators. Even though the idealised devices studied may be viewed as quantum Brownian heat engines, the questions answered by this chapter apply to ballistic electron heat engines in general. Conditions for reversibility and Carnot efficiency, along with behaviour in the maximum power regime are obtained and discussed in relation to previous work on other quantum and electron heat engines such as thermionic and thermoelectric refrigerators and power generators. To provide background information for Chapter 7 in particular, some basic thermodynamic theory

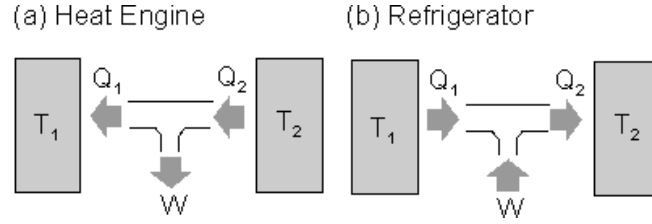


Figure 5.1: (a) A schematic of the operation of a heat engine. Heat Q_2 is drawn from a reservoir at a high temperature, useful work is done, and the remaining heat Q_1 is rejected into a reservoir at lower temperature. (b) A schematic of the operation of a refrigerator. It is essentially a heat engine run in reverse, with an input of work used to draw heat out of the cold reservoir T_1 , cooling it at the expense of adding heat $Q_1 + W$ to the hot reservoir.

will be mentioned here, and an introduction will be given to thermionics, thermoelectrics and other relevant work on quantum heat engines.

5.1 The Thermodynamics of Heat Engines and Refrigerators

5.1.1 What is a Heat Engine?

Essentially, a heat engine is any process which receives heat from a reservoir at a high temperature, does some work on its surroundings, and then rejects heat into a reservoir at a lower temperature [67]. The work done is only some part of the initial input of heat, equal to the difference in the absolute magnitudes of the heat flows from the hot reservoir and to the cold reservoir, $Q_2 - Q_1$, as shown schematically in Figure 5.1 (a).

The efficiency of a heat engine is the ratio of the work out to the heat supplied, that is,

$$\eta_{HE} = \frac{W}{Q_2} = \frac{Q_2 - Q_1}{Q_2} \quad (5.1)$$

In a refrigerator, the cycle is reversed. Heat Q_1 is extracted from a

reservoir at a low temperature using work W . Heat Q_2 , equal to the sum of Q_1 and W , is then deposited into a reservoir at a higher temperature. The coefficient of performance of a refrigerator is equal to the ratio of the heat removed from the cold reservoir to the work input W .

$$\eta_R = \frac{Q_1}{W} = \frac{Q_1}{Q_2 - Q_1} \quad (5.2)$$

This is illustrated in Figure 5.1 (b).

5.1.2 Carnot Efficiency and Reversibility

In 1824 Sadi Carnot, a French engineer, approached the problem of improving the steam engine by examining the basic physical principles upon which efficiency depended, rather than the mechanical details as others had done before him [67, 68]. Although incorrectly believing heat to be a fluid, he correctly derived an expression for the maximum possible efficiency of a heat engine which draws heat from a reservoir at a temperature T_2 and deposits waste heat into reservoir with a lower temperature T_1 as

$$\eta_{HE}^{Carnot} = \frac{T_1 - T_2}{T_2} \quad (5.3)$$

The corresponding Carnot efficiency for a refrigerator which removes heat from a reservoir at temperature T_1 and deposits heat into a hotter reservoir T_2 is

$$\eta_R^{Carnot} = \frac{T_1}{T_2 - T_1} \quad (5.4)$$

The Carnot efficiency provides an upper limit to the efficiency of any heat engine or refrigerator, regardless of the physical systems involved. If a system is working at Carnot efficiency, then this necessarily implies that it is working *reversibly*. Reversibility means that the entropy of the system does not increase with time, and that with an *infinitesimal* change in the system parameters, the direction of heat flow in the system may be reversed [67].

5.2 Electronic Systems as Heat Engines and Refrigerators

Electronic systems used as heat engines and refrigerators may be classed, for the purposes of this thesis, into those which are designed to operate at ambient temperatures, that is at $T \approx 300$ K and above, and those intended to operate at cryogenic temperatures. Into the first category fall thermionic and thermoelectric refrigerators and power generators [69, 70, 71], and into the second NIS (Normal-Insulating-Superconductor junction) [72] and the Quantum Dot refrigerator [73]. The common feature of all electronic refrigeration systems is that cooling is achieved by physically removing high energy electrons from the reservoir to be cooled, it is essentially ‘evaporative cooling’ [74]. For this reason, all the devices incorporate barriers or other energy selection mechanisms such as resonant tunnelling or gaps in the density of states, to limit the current flowing in the device to electrons in particular energy ranges. It is from this idea, that all electronic refrigerators and power generators are energy selective in some way, that the title of the second half of this thesis is derived.

5.2.1 Thermoelectric Power Generators and Refrigerators

In 1822-23, around the same time that Sadi Carnot was studying the limiting efficiency of the steam engine, Thomas Seebeck described in the Journal of the Prussian Academy of Sciences a discovery he called "the magnetic polarisation of metals and ores produced by a temperature difference". Seebeck was interested in this phenomena as supposed evidence in support of his belief that the existence of the earths magnetic field could be explained in terms of the temperature difference between the equator and the polar ice cap. However it is clear that what Seebeck actually discovered was the existence of an electrical current in a closed circuit made up of different conductors in

which the junctions of the materials are held at different temperatures [69]. The real significance of the discovery was in the potential to generate power from low-grade heat. Had Seebeck developed a device to produce electricity using the best materials he found (ZnSb and PbS), he might have made a heat engine with an efficiency of $\approx 3\%$, equal to the best steam engines of his time [69]. The complementary effect, that a current will induce a temperature difference at a junction of two different conductors, was discovered by Jean Peltier, a French watchmaker, twelve years later.

Thermoelectric refrigerators and power generators operate in the regime where electron transport is diffusive rather than ballistic [74]. This means that the distance the electrons must travel to move between the hot and cold reservoirs is large compared with the average distance an electron would travel before colliding inelastically with other electrons or the lattice. Devices are generally made by creating two junctions of n- and p-type semiconductor materials [69]. These materials have different Fermi energies in their bulk state, so when a junction is made between them, band-bending occurs as charge builds up until a constant Fermi energy is established across the junction, as shown in Figure 5.2.

To achieve refrigeration using the Peltier effect, a voltage is applied between the materials to lift the potential of the n-type material, as shown in Figure 5.3 (a). Under the influence of this voltage, the most energetic, or ‘hot’ electrons and holes will flow away from the junction area, thus cooling it. The barrier which accomplishes this energy selection is the step up to the conduction band in the p-type material. Figure 5.3 (a) corresponds to the top junction next to the ‘cooled’ reservoir in Figure 5.3 (c). The electrons and holes removed flow to the other p-n junction across which a voltage of the opposite sign is necessarily established, where they deposit their excess energy as heat. This is shown in Figure 5.3 (b), and corresponds to the lower junction in Figure 5.3 (c).

The device can be run in reverse as a power generator when the top junction is heated to a temperature above that of the heat sink. This utilises the

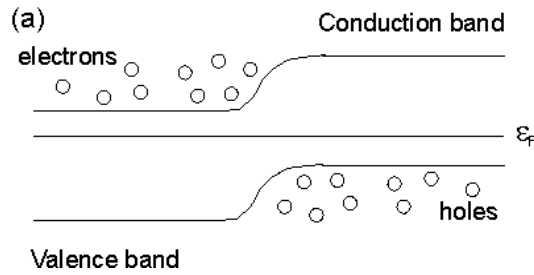


Figure 5.2: A p-n junction. Semiconductor material on the left is doped with atoms with one more electron in the conduction band than the atoms which constitute the semiconductor itself. The extra electrons from the ‘donor’ atoms increase the Fermi energy of the material, shifting it from the centre of the band-gap to close to the valence band. The opposite occurs in p-type material, which is doped with atoms with one less electron in their conduction band. The donor atoms capture electrons from the conduction band to create ‘holes’. The Fermi energy in p-type materials is shifted towards the conduction band. At the junction between these materials the conduction and valence bands of the semiconductor are bent due to charge build-up, so that a constant Fermi energy is maintained across the junction. If this did not occur, there would be a flow of electrons from the n-type, which has more electrons, to the p-type, until a constant Fermi energy was established.

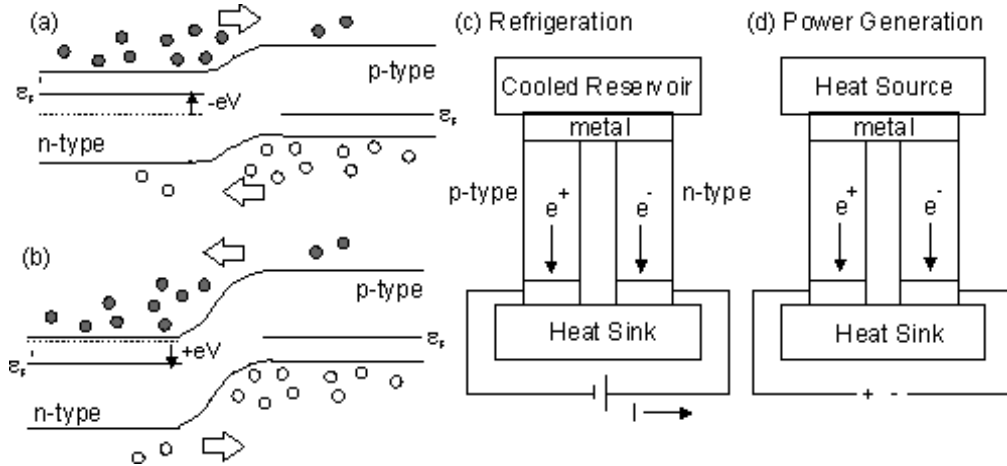


Figure 5.3: (a) A p-n junction which is cooled via the removal of hot electrons. This corresponds to the top junction in (c). (b) A p-n junction at which heat is deposited. It corresponds to the lower junction in (c). Schematic of thermoelectric refrigeration, (c), and power generation, (d). Both schemes work by joining n- and p-type semiconductor materials via a metal junction (which does not change the behaviour of the junction). If a voltage is applied between the materials (shown at the bottom of c), then electrons and holes with higher-than-average energies are drawn from the junction, cooling it (this is the Peltier effect) and depositing waste heat into the reservoir labelled 'heat sink'. If on the other hand, as shown in (d), the junction is maintained at a higher temperature than the heat sink, electrons and holes again flow from the junction and establish a voltage differential between the materials. This is known as the Seebeck effect.

Seebeck effect, in which a temperature differential induces a voltage differential, and is shown schematically in figure 5.3 (d).

All thermoelectric materials are characterised by a parameter $z = S^2\sigma/\kappa$, where $S \equiv dV/dT$ is the thermoelectric power or the Seebeck coefficient, σ is the specific electrical conductivity of the material, and $\kappa = \kappa_{el} + \kappa_{ph}$ is the sum of the specific thermal conductivity due to electrons and phonons. z is a very important parameter for thermoelectric devices as the efficiency of thermoelectric power generators and refrigerators depends only upon the temperature of the heat reservoirs and $M = \sqrt{1 + zT}$, where $T = 0.5(T_H + T_C)$ as [69, 71]

$$\eta_{HE}^{TE} = \frac{(T_H - T_C)(M - 1)}{MT_H + T_C} \quad (5.5)$$

and

$$\eta_R^{TE} = \frac{MT_C - T_H}{(T_H - T_C)(M + 1)} \quad (5.6)$$

The development of high efficiency thermoelectric power generators and refrigerators has not been achieved to date because the best thermoelectric materials discovered to date have a value of $Z \equiv zT$ lower than 4, leading to efficiencies of only a few percent. A significant problem in the development of materials with a high Z value is that the electrical and thermal conductivities are closely related. Increasing the electrical conductivity of a material would increase its z value through σ , however such an increase in σ is usually accompanied by a corresponding increase in the value of the thermal conductivity due to electrons κ_{el} , which decreases z . Despite the lack of materials with a high Z value, the theoretical limit on Z is infinity in the limit of zero phonon conductivity and an infinite bandgap. Reviews of the current state of thermoelectric technology are given in [75, 76, 77, 71].

5.2.2 Thermionic Power Generators and Refrigerators

In contrast to the thermoelectric devices discussed so far, in thermionic devices electron transport is ballistic, that is, the distance electrons must travel between the hot and cold reservoirs is less than the mean-free path between

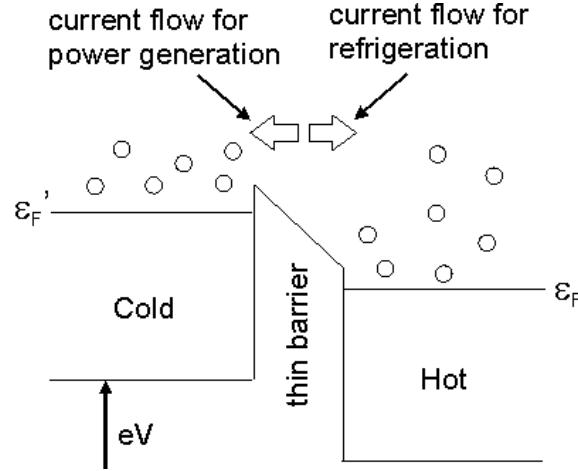


Figure 5.4: A thermionic device utilises a barrier which is not wider than the mean-free path of an electron, either using the work-function of a material in vacuum devices, or a band engineered barrier in solid state devices. When the device is operated as a heat engine, there are sufficient high energy electrons in the hot reservoir that many are transported over the barrier, producing a potential difference between the reservoirs. When operated as a refrigerator, a voltage is applied to one side until the highest energy electrons are removed, thus cooling one side of the device.

inelastic scattering events. In these devices, shown schematically in Figure 5.4, the barrier may be the work function of a material [70], that is, the finite energy required for an electron to escape the material in the case of vacuum devices, or more recently, a barrier constructed via band engineering in semiconductor materials [74].

Vacuum thermionic power generators employ the work function of materials as a barrier, and use the voltage generated across a vacuum between a heated emitter and a collector at a lower temperature. They generally operate at temperatures of $\sim 1500^\circ\text{C}$ with Cesium metal surfaces whose work function is $\sim 2\text{ eV}$ [70]. Most applications for refrigerators are for achieving temperatures below 300 K , and so far no vacuum thermionic refrigerators exist due to a lack of stable materials with a sufficiently low work function,

which would need to be ~ 0.3 eV or less to maintain a useful refrigerating power [71]. The lowest attained is in semiconductors such as Si and GaAs, with a value of $0.7 - 0.8$ eV. A recent development has been the proposal to use nanometer sized gaps, such as can be produced using an AFM tip, to overcome the need for such low work functions [78, 79].

While vacuum designs have the obvious advantage of very low thermal conduction between the emitter and collector electrodes, thermionic refrigerators implemented in semiconductor heterostructures can easily achieve the low barrier heights essential to a significant refrigeration power. It has been shown that due to the increased heat leaks associated with having a barrier narrower than the mean free path, single barrier solid state thermionic devices are out-performed by thermoelectric devices for all known materials [80, 81]. Recently Mahan [74, 75] proposed a multilayer thermionic refrigerator and power generator, dealing with the problem of high thermal conductance in the semiconductor material by having a small temperature differential between a large number of barriers to achieve a finite temperature differential over the entire device.

5.2.3 Cryogenic Electron Refrigerators

Thermoelectric and thermionic refrigerators and power generators are designed to work at ambient and elevated temperatures. Quantum Dot and NIS-based refrigerators on the other hand, are designed to cool at cryogenic temperatures below 1 K, where thermal conduction via phonons is suppressed. The heat flow between the lattice and electrons is proportional to $T_p^5 - T_e^5$ [82], so below 1 K this heat flow is very small, and electrons can be refrigerated below the temperature of the lattice without heating occurring via phonon-electron interactions.

Normal-insulating-superconductor junction (NIS) refrigerators utilise the energy gap in a superconductor as the barrier which selects only high energy electrons for transport. A ‘sandwich’ of normal metal, insulating material and superconducting material is created and biased with a voltage. Electrons

with energies higher than the superconducting gap leave the metal, and thus cool it, by tunnelling through the insulator into the superconductor. Cooling by NIS and SINIS has been experimentally demonstrated [72, 83, 84, 85, 86]. For example, a SINIS structure was recently shown to be able to achieve an electronic temperature of 100mK from an initial temperature of 300mK [86].

Edwards et al. have proposed a quantum-dot refrigerator (QDR) [73, 82] which could potentially be fabricated by etching and gating a 2DEG in a GaAs/AlGaAs heterostructure. The QDR is shown schematically in Figure 5.5 (a), based on the corresponding Figure in [82]. The whole structure is biased as shown in (b) and the central electron reservoir is cooled via the removal of hot electrons and holes. This is done through the resonant levels of quantum dots which have been tuned to a desired energy using electrostatic gates. Figure 5.5 (b) indicates the Fermi occupation in each of the reservoirs via the intensity of shading, and the resonant energy levels of the dots with dark horizontal lines. The resonances are situated above and below the Fermi energy of the cold reservoir to remove hot electrons and holes, respectively.

The practical considerations such as phonon heat leaks and optimum operational temperatures (to name but two) of such a refrigerator are examined in great depth in [82], however an analytic approach to determine fundamental limits to the efficiency and power was not attempted. This gap is addressed in Chapter 7 of this thesis.

5.3 Brownian Heat Engines

The term ‘Brownian motors’ is generally applied to any ratchet which does some work against a load (a recent comprehensive review is given in [87]). A sub-class of Brownian motors are thermal Brownian motors, also called Brownian heat engines, in which the source of non-equilibrium used to power the ratchet is a temperature differential. The most famous example of a Brownian heat engine is the Feynman ratchet, which rectifies the difference between thermal fluctuations in two reservoirs at different temperatures (it

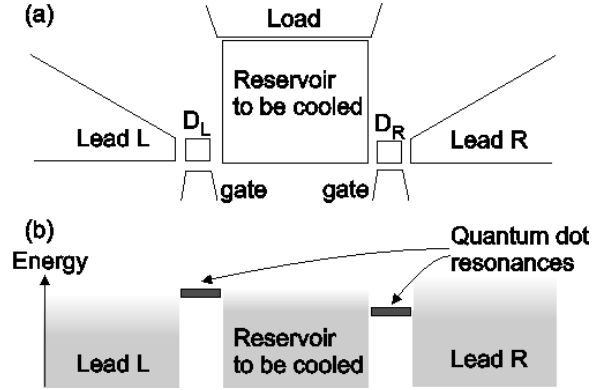


Figure 5.5: The quantum dot refrigerator proposed by Edwards et al. It is designed to be fabricated by surface-gating or otherwise confining a two-dimensional electron gas (2DEG) created at a GaAs/GaAlAs interface. (a) The central reservoir is cooled by the removal of high energy electrons and low energy holes via the quantum dots D_L and D_R to leads L and R . The energy at which electrons are removed is controlled by influencing the energy levels inside the quantum dots by adjacent gates. (b) A schematic of the QDR refrigerator as a function of energy, showing the resonant energy levels in each of the quantum dots. The highest and lowest levels are assumed to be too far away from the Fermi energies of the reservoirs to contribute to transport. Figure based on that in [82].

may be distinguished from the Smoluchowski-Feynman ratchet, discussed in Chapter 2, in which the vane and ratchet mechanism are kept at the same temperature, so cannot therefore do any useful work). While Feynman believed that the ratchet could operate with Carnot efficiency in the quasistatic limit, Parrondo and Español showed that in fact the efficiency of the Feynman ratchet tends to zero in the quasistatic limit. Sekimoto has also analysed the Feynman ratchet analytically and numerically, with the same finding [88, 89, 90].

Similar results are found for Brillouin's Diode [91]. Brillouin considered a diode subject to thermal electrical noise, and showed that in thermal equilibrium, it could not produce a current by rectifying noise. Recently Sokolov

has studied the case where a resistor and an ideal diode are kept at different temperatures, concluding that the efficiency of this system was limited to an efficiency below the Carnot value in the quasistatic limit [92]. If however the resistor is swapped for a second ideal diode, then Sokolov showed that Carnot efficiency can be obtained in the limit that the back-resistance of the diodes tends to infinity [93].

Another important Brownian heat engine is the Büttiker-Landauer model [94, 95]. Figure 5.6 shows Brownian particles subject to a periodic potential gradient (of which only one period is shown). Work is done by the engine by utilising a periodic temperature modulation along the potential to transport particles up a linear potential gradient. It should be noted that the electron heat engine which will be analysed in Chapter 7 can be thought of as a ballistic analogue of this diffusive thermal motor.

The efficiency of the Büttiker-Landauer model has been analysed in detail by Derényi and Astumian in [96]. Splitting the heat transfer into two components, that due to the potential energy of the particles and that due to their kinetic energy, they demonstrated that the transfer of heat from the hot to the cold reservoir via the potential energy of particles is reversible when the ratchet operates quasistatically (when the height of the potential barriers is infinite). The heat transfer via the kinetic energy of the particles was found to be intrinsically irreversible. It could however be made small by invoking a gating mechanism to prevent particles crossing temperature boundaries multiple times before reaching a potential minima. As this second source of irreversibility can in principle be made negligibly small, they found that the efficiency can approach Carnot efficiency. It will be seen in Chapter 7 that the efficiency of the ballistic analogue of this motor also achieves Carnot efficiency when operated in the quasistatic limit of infinitely high barriers. As a result of the use of energy filtering, it will be shown that the energy selective electron heat engine also operates with Carnot efficiency in the regime where, for electrons of one particular energy, the effects of the thermal gradient are exactly countered by those of the potential gradient [97].

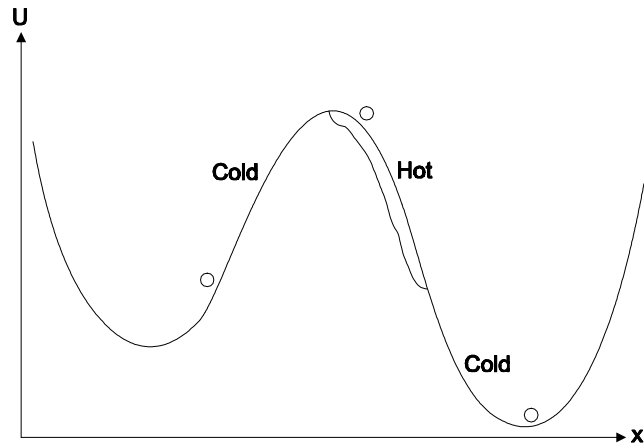


Figure 5.6: The Büttiker-Landauer thermal ratchet consists of overdamped (always thermalised) particles subject to a potential with an (on average) linear slope. A periodic thermal modulation is applied such that the wall of the lower potential well is at a higher temperature than that of the higher well. This means that even though the difference in potential energy between the bottom of the left well and the top of the barrier is smaller than that between that of the right well and the top of the barrier, particles on the right are subject to a higher temperature, and obtain large amounts of thermal energy more frequently than particles on the left. The direction of transport therefore depends on the relative magnitudes of these competing gradients.

5.4 Finite Time Thermodynamics

5.4.1 What is Finite Time Thermodynamics?

To achieve Carnot efficiency, a heat engine must operate reversibly. For cyclic heat engines such as those based on the Carnot cycle, this means that there must be only infinitesimal differences in the temperatures of the working gas and the reservoirs, and in this case it takes an infinite time for the heat engine to perform any work. Practically, heat engines and refrigerators need to perform useful work in a finite amount of time. This requirement leads to the question of how the performance of heat engines and refrigerators which work in finite-time, with finite temperature differences between their working gas and their heat reservoirs, may be optimised. It is this question that the field of finite-time thermodynamics attempts to answer systematically [98, 99, 100, 101, 102].

5.4.2 Endoreversibility and the Curzon-Ahlborn Efficiency

The easiest situation to deal with theoretically is that where the internal changes of state of the working substance occur reversibly, but the exchange of heat between the working substance and the reservoirs occurs irreversibly due to the finite temperature difference between them. A heat engine or refrigerator which operates in this way is generally called *endoreversible*, meaning ‘internally reversible’, and is illustrated schematically in Figure 5.7. A heat engine could be non-endoreversible if, for example, there was non-negligible friction, non-uniform pressure or temperature in the working gas during a cycle.

In what is regarded as the seminal paper of the field, Curzon and Ahlborn [98] examined a heat engine in which the heat transferred between the working gas and the reservoirs was Newtonian, that is, linearly proportional to their temperature difference. They found that the efficiency of the heat en-

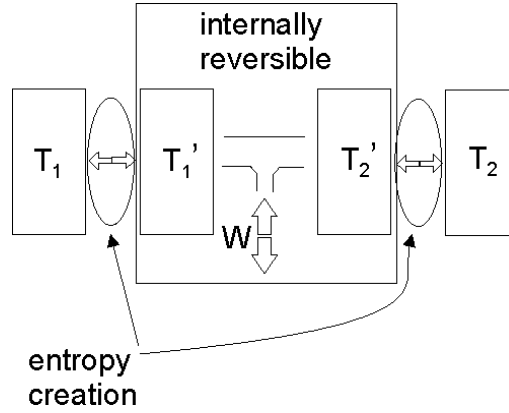


Figure 5.7: Illustration of an endoreversible heat engine. A finite temperature difference exists between the working gas and the reservoir it is in thermal contact with. This finite temperature difference allows a finite amount of heat to be transferred in a finite amount of time. This differs from the reversible situation in which the the working substance and the reservoirs are only infinitesimally different in temperature. The internal changes in state of the working gas are still assumed to be reversible, leading to the name *endoreversible*, meaning "internally reversible".

gine under maximum power conditions was dependent only on the ratio of the temperatures of the reservoirs, $\tau = T_C/T_H$ as

$$\eta_{HE}^{CA} = 1 - \sqrt{\tau} \quad (5.7)$$

As discussed in §5.1.3, the Carnot efficiency is $\eta_{HE}^C = 1 - \tau$, which is greater than the Curzon-Ahlborn (CA) efficiency for all values of τ . The CA efficiency is a very good approximation to the efficiency of many power plants [98], and applies to heat engines which employ a variety of thermodynamic cycles, for example, Carnot, Otto, Joule and Diesel, as long as the heat transfer between the reservoirs and the working substance depends linearly upon the temperature difference between them [103, 104, 105]. Studies have also been done on heat engines in which the heat transfer between the working substance and the reservoirs is not linear with the temperature difference [106], and for

non-endoreversible realisations of heat engines which utilise a Carnot cycle [107, 108]. Velasco et al. recently obtained a τ dependent upper bound on the performance of a Carnot refrigerator working in the finite time regime by maximising the per-unit-time coefficient of performance [109, 110, 111].

5.4.3 Brownian Heat Engines in Finite Time

Velasco et. al. [112] have also been active in examining the performance of the Feynman ratchet [2] in the finite-time regime of operation. The Feynman ratchet consists of a working system which is simultaneously in contact with two thermal reservoirs. Parrondo and Español [3] have shown that this leads to unavoidable irreversibilities in its operation which limit its efficiency to below the Carnot value, as heat leaks from the hot to the cold reservoir even when no work is done due to the fact that thermal fluctuations are dissipated in both reservoirs. Velasco et al. examined the efficiency and power of the Feynman ratchet as a function of an ‘irreversibility parameter’, proportional to this heat leak between the hot and cold reservoir. When the ratchet is operating in the linear regime (when the energy required to lift the pawl is much less than the temperature of the cold reservoir) it was found that the efficiency at maximum power was $\eta_F = (1-\tau)/(1+\tau)$ when the ‘irreversibility parameter’ of the ratchet was set to zero. The behaviour of the ratchet was also examined for finite values of the irreversibility parameter, in which case loop-shaped power versus efficiency curves were found, as well as an upper bound for the power output of the ratchet which was dependent upon the ratio of the energy needed to lift the pawl and the temperature of the hot reservoir.

Salas and Hernández [113] have analysed Sokolov’s version [92] of Brillouin’s diode [91], consisting of a diode and a linear resistor held at different temperatures, and emphasised the similarity of the loop-shaped behaviour of the power versus efficiency found in this system to that found in other real engines. They suggested that the heat transported from the hot to the cold reservoirs due to the dissipation of thermal fluctuations in the diode engine

under the condition of no current (zero power and zero efficiency) plays formally the same role as that of the heat leak in models of real heat engines such as that studied by Curzon and Ahlborn.

In the second part of Chapter 7, an energy selective electron heat engine, which may be viewed as a ballistic analogue of the Büttiker-Landauer Brownian heat engine, will also be examined in the maximum power regime. Unlike the Feynman ratchet and Brillouin diode heat engine (consisting of a diode and a linear resistor), the energy selective heat engine is not fundamentally irreversible, but it will be seen that loop-like behaviour in power versus efficiency curves can still be obtained in particular (non-optimal) operating regimes. The fundamental difference between the electron heat engine studied in this thesis and the Brownian heat engines studied in the maximum power regime to date is the energy selectivity of the electron heat engine, which can be used to avoid heat leaks in situations of zero power.

Chapter 6

Quantum Ratchets as Heat Pumps

In Chapter 4 it was established that rocked quantum electron ratchets can exhibit net current reversals as a function of temperature, magnitude of rocking voltage, and barrier height. In this chapter the implications of this result for the *heat currents* flowing in the device will be examined. The crucial observation that underlies this chapter is that at parameter values where the net electron current changes sign, equal numbers of electrons are being transported in opposite directions through the device, *but the energy distribution of these two currents is not the same*. The quantum ratchet is thus able to transfer heat between the reservoirs even though there is no net transfer of electrons.

The potential barrier used to model the experimental quantum point contact ratchet in Chapter 2 (hereby known as the ‘experimental potential’) is shown in Figure 6.1 under negative (left) and positive (right) source-drain voltages. The spectral distribution of the electron current is indicated qualitatively in both cases via arrows. The width of the arrows signifies the relative contribution of high and low energy electrons to the current in each case.

Quantum ratchets based on asymmetric quantum point contacts can thus

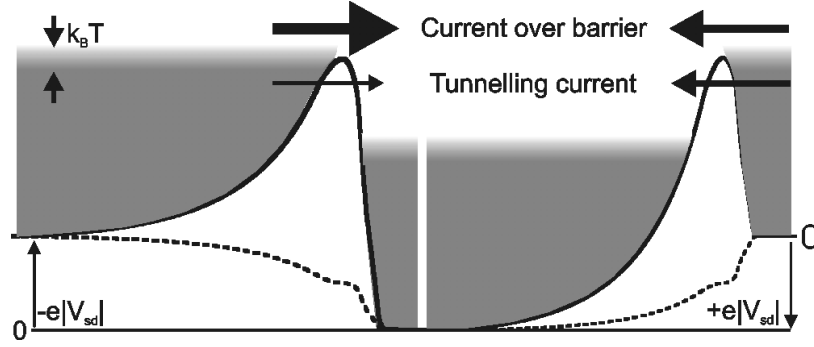


Figure 6.1: The left picture shows the experimental potential under negative source-drain voltage, where it is thicker and smoother than under positive source-drain voltage (shown in the right picture, note that the vertical axis is offset by $e|V_{sd}|$ from that of the left figure). This change in shape means that the transmission of tunnelling electrons is favoured for positive source-drain voltages, while transmission of electrons with energies higher than the barrier is more likely to occur in the opposite direction, that is, for negative source-drain voltages. At parameter values where the number of left and right going electrons exactly cancels, heat is still transported across the device due to the fact that the energy transported by electrons travelling in opposite directions across the barrier is, on average, not the same.

be described as heat pumps [114]. It will, however, be shown in this chapter that asymmetric point contacts are not particularly effective at pumping heat, with the rocking action of the ratchet heating both sides of the device, one less than the other. In the second part of this chapter (§6.3), a design which incorporates an asymmetric resonant tunnelling double barrier structure will be shown to be much more effective at pumping heat, so much so that it can behave as a refrigerator, cooling one reservoir at the expense of heating the other.

6.1 Adaptation of Landauer Theory to Heat Currents

In §2.2.3, the Landauer equation for electrical current through a one-dimensional conductor was derived (Equation 2.6), and is repeated here for the convenience of the reader.

$$I(V_{sd}, T) = \frac{2e}{h} \int_0^\infty \tau(E, V_{sd}) \{f_L(E, \varepsilon_L, T_L) - f_R(E, \varepsilon_R, T_R)\} dE \quad (6.1)$$

This equation relates the current between two electron reservoirs to the product of the difference in the Fermi occupation functions f_L and f_R in the left and right reservoirs and the probability, τ , that an electron will be transported through an intervening constriction.

The analysis will be limited to parameter values where $I_{net} = 0$ in order to avoid any net transfer of electrons between the reservoirs which would entail a ‘trivial’ heat flow. The heat deposited in a reservoir by an electron with energy E can be determined from the first law of thermodynamics for an open system, in which volume and pressure is constant [67]

$$\dot{U}_{L/R} = \dot{Q}_{L/R} + \mu_{L/R} \dot{N}. \quad (6.2)$$

The change in the internal energy of the left reservoir is $\dot{U}_L = -E\dot{N}$ and that of the right reservoir is similarly $\dot{U}_R = E\dot{N}$. The chemical potentials $\mu_{L/R}$ can be approximated by the Fermi energies of the reservoirs, as long as $kT \ll \varepsilon_F$. We can therefore obtain an expression for the heat flux into the left and right reservoirs $\dot{Q}_{L/R}$ (where L/R indicates the left or right reservoirs) from Equation 7.9 as

$$\dot{Q}_L(\pm V_{sd}) = \pm \frac{2}{h} \int_0^\infty [E - \varepsilon_L] \tau(E, \pm V_{sd}) \{f_L[E, \varepsilon_L, T] - f_R[E, \varepsilon_R, T]\} dE \quad (6.3)$$

$$\dot{Q}_R(\pm V_{sd}) = \mp \frac{2}{h} \int_0^\infty [E - \varepsilon_R] \tau(E, \pm V_{sd}) \{f_L[E, \varepsilon_L, T] - f_R[E, \varepsilon_R, T]\} dE \quad (6.4)$$

$E - \varepsilon_{L/R}$, will not be the same for the left and right reservoirs as their Fermi energies differ by $+eV_{sd}$ (see Figure 6.1) when a positive source-drain

voltage is applied, and $-eV_{sd}$ for a negative source-drain voltage. In the analysis it will be assumed that the source-drain voltage is applied equally to the left and right sides of the device. This is done for analytic simplicity, and as only differences in potential are meaningful, this assumption does not alter the results obtained. The equilibrium ($V_{sd} = 0$) Fermi energy of the left and right reservoirs will be denoted ε_F . Then $\varepsilon_L = \varepsilon_F \pm eV_{sd}/2$ and $\varepsilon_R = \varepsilon_F \mp eV_{sd}/2$ are the Fermi energies of the reservoirs when a source-drain voltage of $\pm V_{sd}$ is applied.

Defining

$$\Delta f(E, |V_{sd}|, T) \equiv \{f_L[E, \varepsilon_F + e|V_{sd}|/2, T] - f_R[E, \varepsilon_F - e|V_{sd}|/2, T]\}$$

and

$$\dot{Q}_{L/R}^{net}(|V_{sd}|) = 0.5[Q_{L/R}(+V_{sd}) + Q_{L/R}(-V_{sd})]$$

we can write the time-averaged heat flux into each reservoir when a square wave voltage is applied to the device as

$$\dot{Q}_L^{net}(|V_{sd}|) = 0.5[\Omega - \Lambda]$$

and

$$\dot{Q}_R^{net}(|V_{sd}|) = 0.5[\Omega + \Lambda] \quad (6.5)$$

where

$$\Omega = \frac{2}{h} \int_{U_0}^{\infty} e|V_{sd}| \Gamma(E, |V_{sd}|) \Delta f(E, |V_{sd}|, T) dE \quad (6.6)$$

and

$$\Lambda = \frac{2}{h} \int_{U_0}^{\infty} [E - \varepsilon_F] \Delta \tau(E, |V_{sd}|) \Delta f(E, |V_{sd}|, T) dE \quad (6.7)$$

Here $\Gamma(E) = 0.5[\tau(E, +|V_{sd}|) + \tau(E, -|V_{sd}|)]$ is the average transmission probability. Λ is the amount of heat pumped from the left to the right side of the ratchet over one full rocking cycle, and is non-zero only for asymmetric devices. Ω is the ohmic heating that any symmetric mesoscopic device would experience under a symmetric square wave source-drain voltage of $|V_{sd}|$, and is equally distributed in the two reservoirs.

The coefficient of performance of a refrigerator was defined in Chapter 5. Assuming that the action of the ratchet will be to remove heat from the left side, we define the appropriate coefficient of performance (COP) as:

$$\eta_R = \frac{\frac{|\dot{Q}_L|}{\dot{Q}_R - |\dot{Q}_L|}}{\frac{\Lambda - \Omega}{\Omega}}. \quad (6.8)$$

When Λ is zero there is no heat pumped from one reservoir to the other and $\eta_R = -1$. As some heat is pumped from the left to the right reservoir, that is, as the magnitude of the difference in the transmission probabilities $|\Delta\tau|$ becomes comparable to the average of the transmission probabilities, Γ , η_R grows less negative and approaches zero as the ratchet pumps all the ohmic heat to the right side of the ratchet. If the device actually *cools* the left reservoir, with $\Lambda \geq \Omega$, η_R becomes positive.

6.2 Numerical Calculations for the Experimental Ratchet

The coefficient of performance (COP), η_R , of the experimental potential as a heat pump may be calculated for parameter sets where the numerically calculated net current experiences a sign change, that is, where the integral of $\Delta\tau(E)\Delta f(E, \varepsilon_F, |V_{sd}|, T)$ with respect to E is non-trivially zero. $\Delta f(E, \varepsilon_F, T)$ and $\Delta\tau(E)$ (calculated for the ‘experimental’ potential) are shown in Figure 6.2). For each value of T and $|V_{sd}|$, the Fermi energy (or energies) for which the net current equalled zero was numerically determined, and the COP then calculated for this parameter triplet.

Figure 6.3 shows the Fermi energy and temperature pairs for which the net current through the ratchet was zero for bias voltages of 0.1, 1.0 and 2.5mV, which correspond to increasing Fermi window widths. There are two ‘branches’ for each value of source-drain voltage. This occurs because there are two Fermi energies at which the centre of the Fermi window may be placed so that the net current equals zero. For zero source-drain voltage, these Fermi

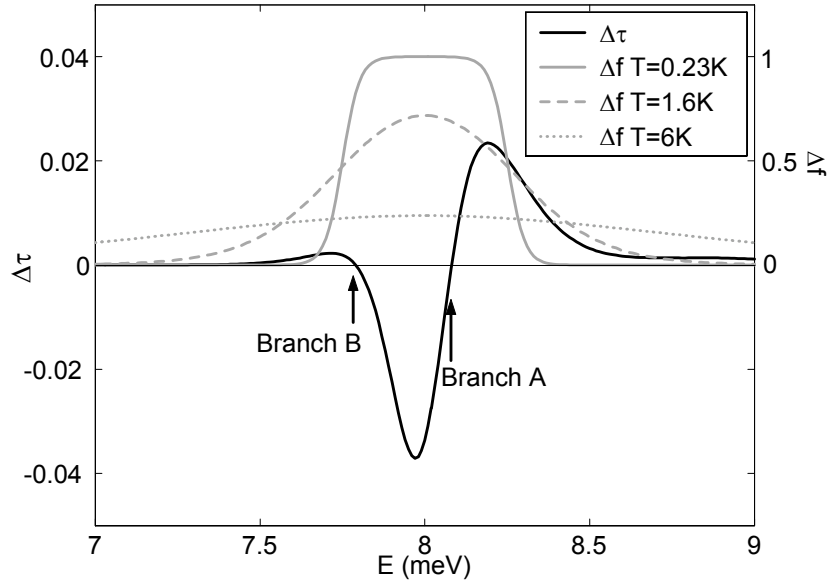


Figure 6.2: The left vertical axis shows $\Delta\tau$ for the experimental potential (shown in Figure 4.10). The right vertical axis shows the Δf ‘window’ for a Fermi energy equal to the barrier height of 8meV, for temperatures of 0.3K, 1.6K and 6K, and a source-drain voltage amplitude of 0.5meV (which determines the width of the window at $T = 0$ K). When the Δf window samples the $\Delta\tau$ curve over an area where the integral of the $\Delta\tau$ curve is zero, then the net current will be zero. There are two energies at which the $\Delta\tau$ curve changes sign. These are associated with the two ‘branches’ of Fermi energies which yield zero net current, marked ‘A’ and ‘B’ in ensuing Figures.

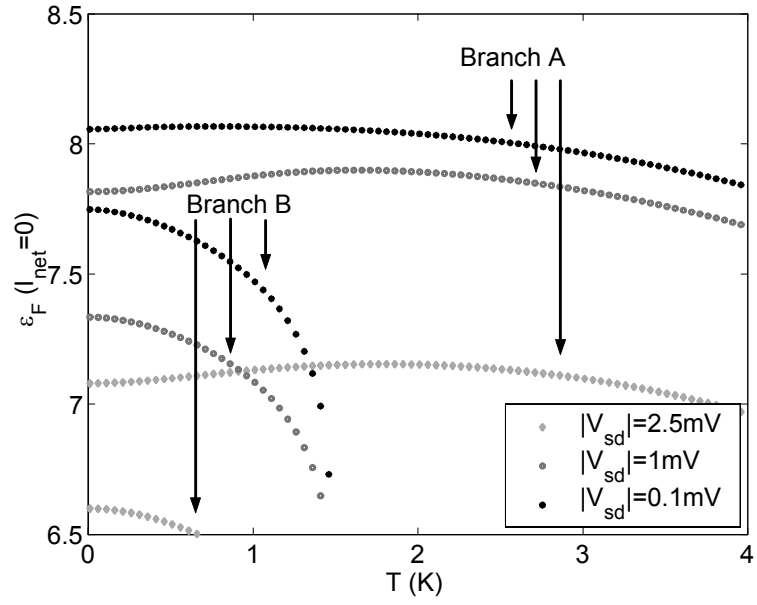


Figure 6.3: Fermi energy and temperature pairs which yield zero net current for $|V_{sd}| = 0.1, 1.0$ and 2.5meV . There are two ‘branches’ for each value of $|V_{sd}|$ because there are two separate Fermi energies at which the Fermi window can be placed to sample equal positive and negative areas of the $\Delta\tau$ curve, one around 7meV , and one around 8meV (see Figure 6.2).

energies correspond to the energies at which the $\Delta\tau$ curve changes sign, and are marked on Figure 6.2.

Figure 6.4 shows $\eta + 1$ for the ε_F , T and $|V_{sd}|$ parameter triplets plotted in Figure 6.3. The two branches which appear in Figure 6.3 are again apparent. The negative branch (Branch A of figure 6.3) corresponds to heat being pumped from the right reservoir to the left reservoir, and is associated with the sign change in $\Delta\tau$ around 8.2 meV. The positive branch (Branch B of Figure 6.3) corresponds to the pumping of heat in the opposite direction, and is associated with the sign change in $\Delta\tau$ around 7.8 meV.

The direction of heat transfer can be understood by recalling firstly that where the $\Delta\tau$ curve is positive, electrons are transmitted, on average, from the right to the left reservoir over a full rocking cycle. Secondly, if the positive part of the $\Delta\tau$ curve sampled by the Fermi window is higher in energy than the negative part, then the total energy of the electrons flowing from right to left is higher than that of the electrons which flow from left to right when the net current is zero, and so heat is pumped from right to left (in this example).

Figure 6.4 shows that the coefficient of performance is actually negative for the experimental potential, $\eta \approx -1$, because the amount of heat pumped from one reservoir of the device to the other due to the action of the ratchet, Λ , is much smaller than the amount of heat created in each reservoir, Ω . The underlying reason for the low COP for the experimental potential is that it depends upon the ratio of $|\Delta\tau(E)|$ to the *average* probability $\Gamma(E)$. In the case of the experimental potential this ratio is of the order of 0.05. This means that the difference in the spectral distribution of the current for positive and negative source-drain voltages is very small, and many electrons participate in the current and cause ohmic heating while there is only a small difference in the energy currents accross the barrier under a change in sign of the source-drain voltage. The preferable situation is where $|\Delta\tau(E)|$ is the same order of magnitude as $\Gamma(E)$, that is where *only* low energy electrons are transmitted into the reservoir to be cooled under one sign of the source-drain

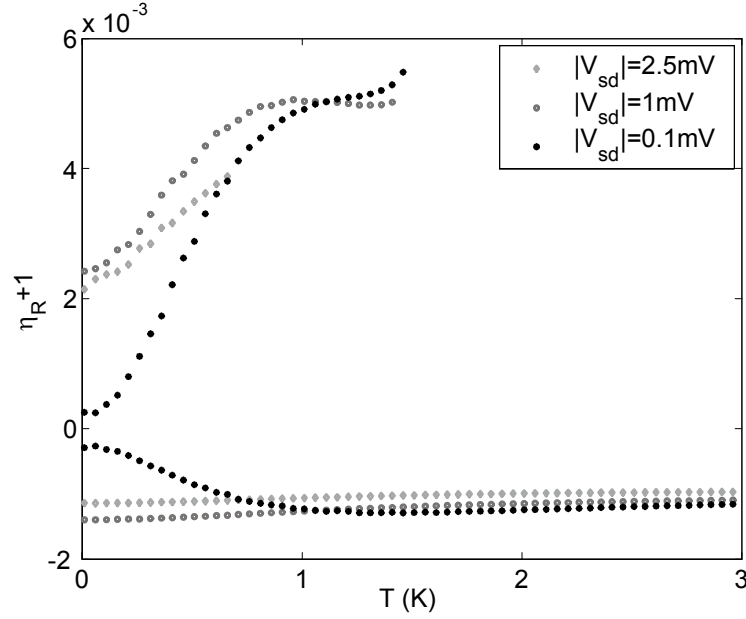


Figure 6.4: $\eta + 1$ for the 'experimental' potential for the Fermi energy, temperature and bias voltage triplets shown in Figure 6.3. The positive branches correspond to Branch B in Figure 6.3, in this case heat is being pump from the left to the right reservoirs of the ratchet. The negative branches to correspond to Branch A marked on the same figure, and in this case heat is pumped in the opposite direction, from the right to the left reservoirs. $\eta + 1$, rather than η is plotted as in both cases the amount of heat pumped from one reservoir to the other is still less that the ohmic heating which occurs in each reservoir due to the rocking action of the ratchet, meaning that η is negative in both cases.

voltage, and *only* high energy electrons are transmitted out of the reservoir under the opposite sign. In this way all electrons which are transported perform heat transfer, that is, contribute to cooling one of the reservoirs. This situation can be attained using sharp energy selective features such as resonant tunnelling states, and will be discussed in the next section.

6.3 Numerical Calculations for a Double Barrier Ratchet

It has been established that an efficient quantum ratchet heat pump would transmit *only* low energy electrons when tilted in one direction, and *only* high energy electrons when tilted in the opposite direction. An asymmetric quantum dot in the resonant tunnelling regime of transport can, in principle, be designed to have these properties. Landauer formalism can be used to describe transport in this regime as long as there is no electron-electron interactions. If phase-breaking scattering is present, then the sequential tunnelling picture, described via a rate equation approach is used [40, 115]. It can, however, be shown [40] that these two approaches yield identical expressions for the current per mode around resonance. Note that often the term ‘quantum dot’ is more closely associated with devices whose dimensions are sufficiently large that the spacing of the resonant energy levels is much smaller than kT , but which have a very small capacitance so that peaks in the conductance occur at an energy spacing given by integral multiples of e^2/C , where C is the capacitance of the dot. In this thesis the term ‘quantum dot’ will be used to refer to devices with dimensions of the order of an electron wavelength, in which confinement effects are the primary consideration.

A quantum dot (1D-0D-1D system) has been chosen for study, rather than an alternative resonant tunnelling system such as band engineered $\text{GaAl}_{1-x}\text{As}_x$ (a 3D-2D-3D system), because the quasi-0D confinement gives the desired transmission of electrons in a very narrow range of energies. In comparison, 3D-2D-3D systems transmit electrons with a wide range of total

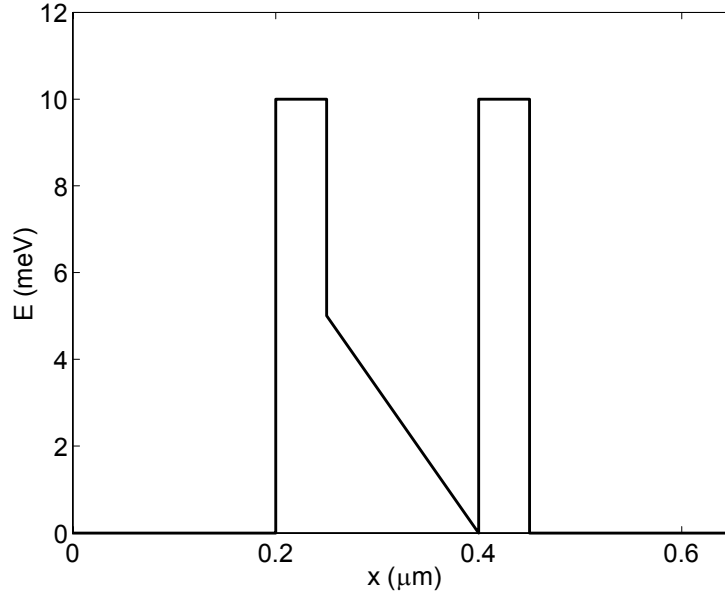


Figure 6.5: The rocked resonant tunnelling ratchet potential under zero source-drain voltage. The essential feature for pumping heat is the asymmetric base of the well. This ensures that the resonances shift in energy when the device is subject to a square wave source-drain voltage. Note that the effective mass of electrons used in these calculations is that for GaAs, as has been used throughout this thesis

energies, as the momentum of the electrons is only confined in one dimension in this case. 3D-0D-3D transport, where the leads connecting the dot to the reservoirs are three-dimensional, is dealt with in detail in Appendix H.

In this section the COP of a hypothetical ratchet based on the potential profile of an asymmetric quantum dot (to be called a Rocked Resonant Tunnelling Ratchet, RRTR) will be calculated. It is found that this device configuration is much better at pumping heat than the asymmetric QPC potential used in the calculations of the previous section, to the extent that it can actually remove heat from one reservoir, so cooling it (at the expense of heating the other reservoir). The dimensions of the potential chosen for study were determined by an iterative process to optimise the coefficient of performance (COP) of the RRTR, and are shown in Figure 6.5.

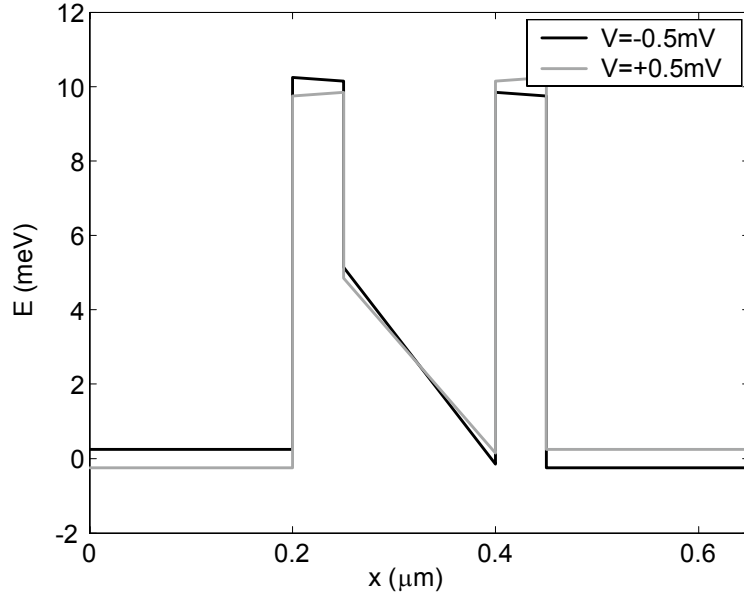


Figure 6.6: The resonant tunnelling quantum ratchet potential under $V_{sd} = \pm 0.5 \text{ mV}$, where 0.25 mV is applied to each side of the ratchet.

The important feature of the potential shown in Figure 6.5 is that the base of the double barrier structure is asymmetric. This means that the shape of the potential is different under source-drain voltages of opposite sign, and thus ensures that the resonance energy is an asymmetric function of V_{sd} , and allows heat to be pumped from one side to the other. The width of the structure was chosen so as to give well spaced resonances.

A linear voltage drop was applied to the potential (Figure 6.6) and the transmission probability as a function of energy calculated for $V_{sd} = \pm 0.5 \text{ mV}$. The results are shown in Figure 6.7. It can be seen that the asymmetry of the potential has shifted the energy at which resonances occur. This shift means that the magnitude of the difference of the two transmission probabilities, $\Delta\tau(E)$, is almost the same as that of their average, $\Gamma(E)$, around the first two resonances. This is beneficial for the efficiency, as it depends upon the ratio of the integrals of $\Delta\tau(E)$ and $\Gamma(E)$ through Λ and Ω .

In the same manner as in the previous section, Fermi energies were found

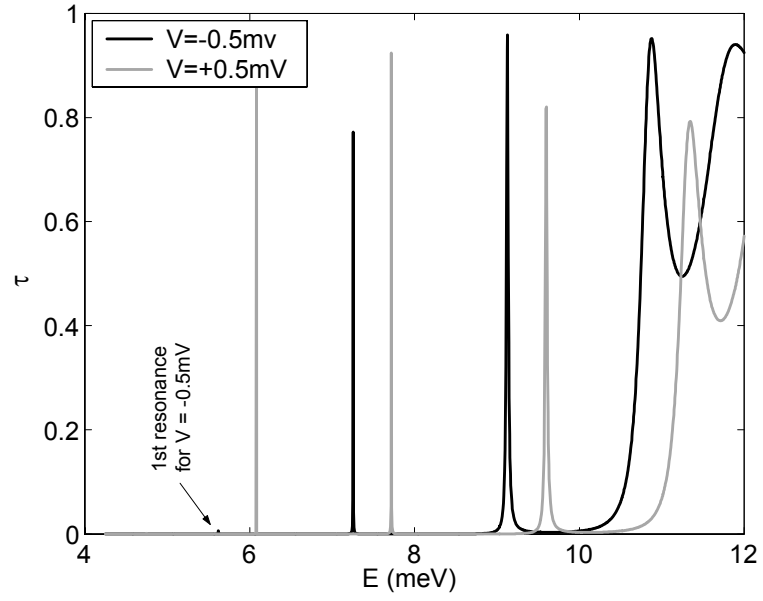


Figure 6.7: The transmission probability of the double barrier potential under a bias voltage of ± 0.5 mV.

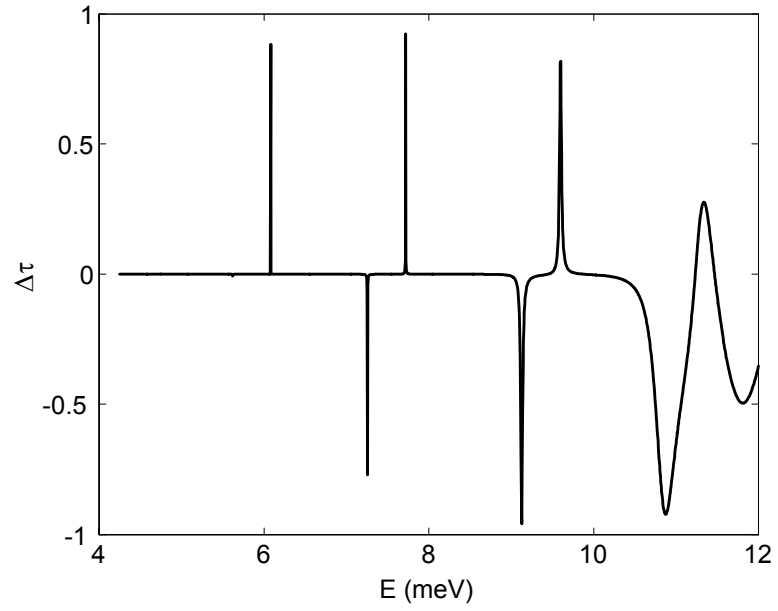


Figure 6.8: $\Delta\tau$ for the double barrier potential under $|V_{sd}| = \pm 0.5$ mV.

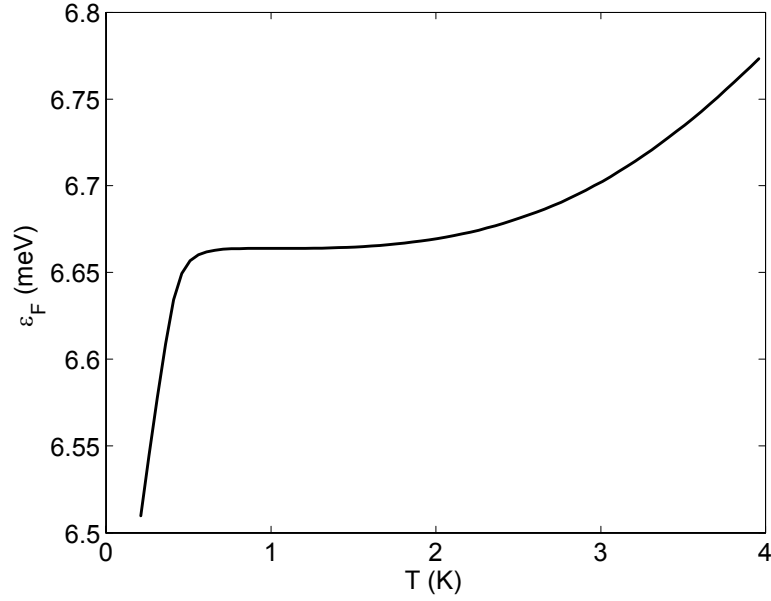


Figure 6.9: Fermi energies for which the net current through the ratchet is zero (for $|V_{sd}| = 0.5\text{mV}$) as a function of temperature.

(as a function of temperature) for which the net current through the device was zero (at a set bias voltage of $|V_{sd}| = 0.5\text{mV}$) and these are shown in Figure 6.9. The power and efficiency of the RRTR will be calculated for Fermi energies between 6.5 and 6.8 meV, which places the Fermi window between the first positive and second negative peak in the $\Delta\tau$ curve shown in Figure 6.8. A number of regions could have been chosen, but for clarity we focus on just this first region. For example, if the Fermi window is placed between the second negative and second positive resonance, the device will pump heat from the right to the left reservoir.

For each parameter triplet in the region chosen for study, the COP of the RRTR as a refrigerator was calculated as a function of temperature, and is shown in Figure 6.10.

The main point to note in Figure 6.10 is that the coefficient of performance is *positive* for some range of temperature, indicating that the RRTR is able to remove heat from the left reservoir. The asymmetric quantum point contact

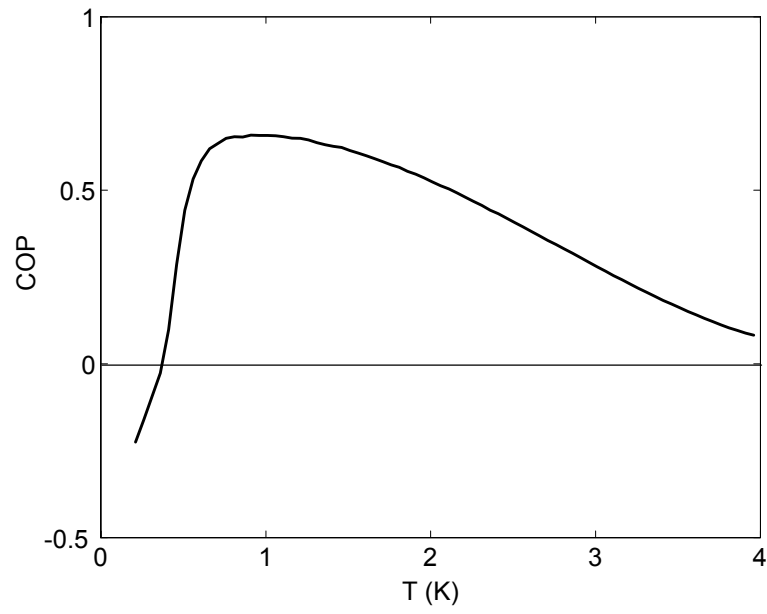


Figure 6.10: The coefficient of performance of the RRTR for the parameter triplets shown in the previous figure. For temperatures where the COP is greater than zero the RRTR is refrigerating the left reservoir of electrons.

barrier used to model the experiments was not able to achieve this.

6.4 Conclusions

In this chapter it has been shown that mesoscopic rocked electron ratchets can act as heat pumps. This can occur when the ratchet rectifies the motion of low energy electrons in a direction opposite to that of high energy electrons, so as to create a net flow of heat in the absence of a net current of particles, that is, where the net current exhibits a reversal.

The second conclusion drawn in this chapter is that the amount of heat transported depends upon the ratio of the integrals of $|\Delta\tau(E)|$ to $\Gamma(E)$, the difference between the transmission probability of the ratchet under bias voltages of opposite sign to the average of these transmission probabilities. As the transmission probabilities of the quantum point contact potential are very similar under positive and negative bias voltages, the coefficient of performance of the experimental potential as a refrigerator is negative. This means that operating the ratchet heats both reservoirs of electrons either side of the ratchet, but one less than the other.

Finally, it was shown in this chapter that one way of increasing $|\Delta\tau(E)|$ with respect to $\Gamma(E)$ is to use a rocked asymmetric quantum dot as the quantum ratchet. This introduces resonance peaks into the transmission probability which shift in energy under positive and negative bias voltages. It was found numerically that the coefficient of performance of the RRTR was high enough to cool one side of the device.

Given that it has been shown that a particular rocked resonant tunnelling ratchet can in principle remove heat from an electron reservoir, it is interesting to determine what limits the operating efficiency of an *idealised* RRTR. An idealised RRTR has resonances which may be made arbitrarily sharp and may be arbitrarily located as a function of energy. It will be shown analytically in the next chapter that the efficiency of such an idealised rocked resonant tunnelling ratchet as a refrigerator, or as a heat engine in the case

that the electron reservoirs have different temperatures, is limited only by the Carnot value.

Chapter 7

Energy Selective Electron Heat Engines

7.1 Using Energy Filtering in an Electron Heat Engine

In the previous chapter, a rocked resonant tunnelling ratchet was shown by numerical simulation to be significantly better at pumping heat than the potential used to model the experimental asymmetric QPC ratchet. This chapter is motivated by Chapter 6 in that it describes the fundamental analytical limits of the efficiency and power of the rocked resonant tunnelling ratchet. However, the fundamental efficiency and power limits obtained actually have a much broader applicability, with implications for all of the electron heat engines and refrigerators which were reviewed in Chapter 5. As mentioned in that chapter, electron heat engines and refrigerators work by employing energy selectivity in electron transport, usually by means of an energy barrier in the direction of transport. One of the important conclusions of the present chapter is that the efficiency of electron heat engines and refrigerators can be increased to the Carnot value if energy selectivity is increased to the point where the only electrons transported are those with an energy equal to that at which the Fermi occupation of states in the two

electron reservoirs is equal [97].

7.1.1 The Energy Selective Electron Heat Engine

The system which will be the focus of this chapter is shown in Figure 7.1, and will be called an energy selective electron (ESE) heat engine. It consists of two infinitely large electron reservoirs with different temperatures and chemical potentials. They are perfectly thermally insulated from each other, and interact only via an ‘energy filter’, which freely transmits electrons in a specified energy range and blocks the transport of all others. Three regimes of behaviour will be considered in this chapter, the first where only electrons with one particular energy (shown in Figure 7.1 as E_R) are transmitted, the second where electrons in a wide range, optimised for maximum power, are transmitted. The final regime considered is intermediate to these two, and corresponds to the transmission of a small, but finite range of energies. Such a filter could in principle be implemented in a 1D-0D-1D system such a quantum dot connected to the reservoirs via one-dimensional (1D) leads. Assumptions that will be used throughout this chapter are as follows:

1. That transport between the reservoirs through the energy filter is ballistic. This means that the mean free path of the electrons between inelastic collisions is greater than the distance the electrons have to travel between the reservoirs. This assumption has been used throughout this thesis.
2. The reservoirs are much larger than the mean-free-path of an electron, so that transmitted electrons quickly relax to the Fermi energy once in a reservoir, thus maintaining an equilibrium distribution. This, and the previous assumption allow Landauer formalism to be applied the system and means all entropy generation in the system occurs in the two electron reservoirs.
3. $kT_C \ll \varepsilon_C$, and $kT_H \ll \varepsilon_H$. In this case the chemical potential of a

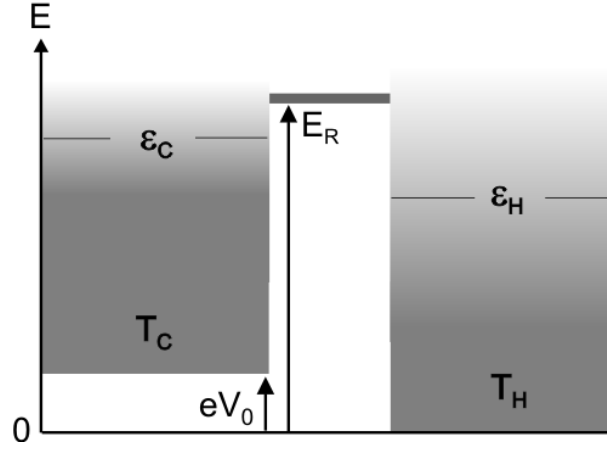


Figure 7.1: The ESE heat engine. It consists of just one hot and one cold reservoir. The reservoirs have Fermi energies ε_H and ε_C , and temperatures T_C and T_H respectively. The ‘energy filter’ allows the reservoirs to exchange electrons with a specified range of energies. In this case, only electrons with energy E_R are transmitted.

free electron gas may be accurately approximated by the Fermi energy, making the derivations in this chapter analytically tractable.

7.1.2 The Idealised Rocked Resonant Tunnelling Ratchet

To see how the the ESE heat engine is related to the RRTR described in Chapter 6, note that the ESE heat engine can be viewed as operating as one half-period of the rocked resonant tunnelling ratchet. In this case it is assumed that the resonant tunnelling energy filter is asymmetric so that its shape changes to have a resonance at $E_R = \varepsilon_C + \phi$ when a bias voltage of eV_0 is applied to the right reservoir, and a resonance identical in width and height at $\varepsilon_C - \phi$ when a bias voltage of $-eV_0$ is applied to the right reservoir. These two situations are illustrated schematically in Figure 7.2 (a) and (b).

It is shown in Appendix F that the heat flux into either reservoir in the idealised RRTR is the same under positive and negative source-drain voltages. This is a result of the symmetry of the resonance shift, which means

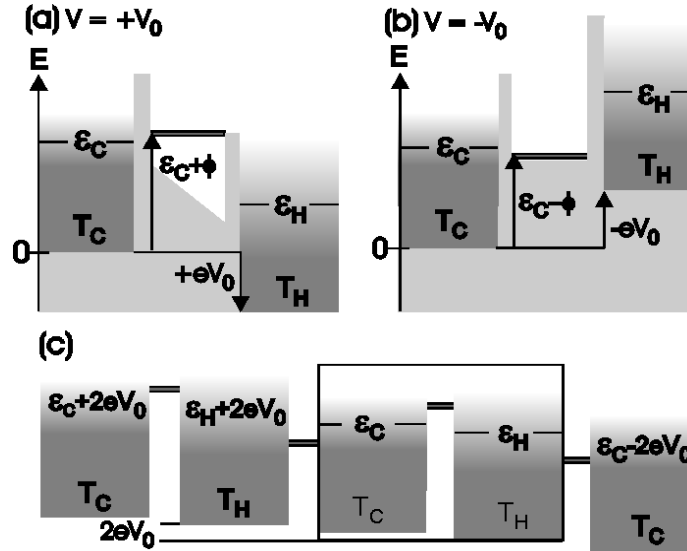


Figure 7.2: (a) The idealised RRTR with a positive bias voltage applied to the right reservoir. (b) with a negative voltage applied to the right reservoir. (c) an equivalent "static" resonant tunnelling ratchet, consisting of an array of alternately hot and cold reservoirs which move particles against a constant potential slope. This type of ratchet is generally known as a "Seebeck" ratchet [4], or alternatively as a Brownian Heat Engine (see, for example, [96, 87]). The Büttiker-Landauer ratchet [94, 95] is also of this type. To model the behaviour of the two devices it is sufficient to analyse just two reservoirs and the filter/resonance between them. Two such reservoirs which comprise an ESE heat engine have been highlighted with a box.

that during one half of the cycle electrons carrying heat ϕ are transported out of the cold reservoir into the hot reservoir, during the other half the same number of electrons, this time carrying heat $-\phi$, are transported out of the hot reservoir and into the cold reservoir.

7.1.3 The Seebeck Resonant Tunnelling Ratchet

An array of ESE heat engines may also be examined, and is shown in Figure 7.2 (c). This system is interesting to mention, as it bears a strong *prima facie* resemblance to the Büttiker-Landauer model [94, 95], discussed in §5.3. Such ratchets are generally known as "Seebeck ratchets" [4]. It is interesting that although this 'Seebeck' resonant tunnelling ratchet operates in the ballistic transport regime and the Büttiker-Landauer heat engine in the diffusive regime, the efficiency of both is limited only by the Carnot value in principle [96, 97]. In the same manner as for the RRTR, it can be shown that the heat change in a reservoir in this ratchet due to its interaction with the reservoir on the right is the same as the heat change due to its interaction with the reservoir on the left. This means that it is sufficient to analyse the fundamental limits of the efficiency and power of the ESE heat engine to understand those of both the Rocked and the Seebeck resonant tunnelling ratchets. Therefore, only the ESE heat engine will be discussed in the remainder of this chapter.

7.2 Reversible Regime of Operation

In this section it will be shown that electrons with a particular, very narrow range of energies may be reversibly transported between electron reservoirs at different temperatures and potential energies. This result is surprising as it is impossible to reversibly transfer electrons between reservoirs which differ only in temperature (except at the Fermi energy, where no useful work can be done) or between reservoirs which differ only in potential energy. However, when both differences in potential energy *and* temperature exist between two electron reservoirs, reversible transport *is* possible away from the Fermi

energy, at the energy where the Fermi distributions in the two reservoirs are equal.

The approach will be to derive the entropy change per electron transferred between the reservoirs as a function of energy, then to use the Landauer expression for the current between two 1D reservoirs to calculate the entropy change in the system per unit time due to the transfer of electrons in an infinitesimally narrow energy range about E_R . The heat flux into each reservoir may then be calculated and the efficiency derived from the expressions for the heat flux into the hot and cold reservoirs as discussed in §6.1.

7.2.1 Entropy Change due to Transfer of Electrons between Electron Reservoirs

In this section, an analytic expression will be found for the entropy change in the ESE heat engine when a small number δN of electrons each with total energy E , are transferred between the two reservoirs. This expression will then be solved to find the energy at which electrons may be transferred between the reservoirs with no increase in the entropy of the composite system.

The change in entropy of a free electron gas consisting of N electrons at a temperature T and having a Fermi energy ε_F is [67]

$$S = Nk \frac{\pi^2}{2} \left(\frac{kT}{\varepsilon_F} \right) \left[1 - \frac{\pi^2}{10} \left(\frac{kT}{\varepsilon_F} \right)^2 + \dots \right] \quad (7.1)$$

If $kT \ll \varepsilon_F$ then

$$S \approx Nk \frac{\pi^2}{2} \frac{kT}{\varepsilon_F} \quad (7.2)$$

It is shown in Appendix G that the change in entropy of a free electron gas under the addition of δN electrons is then

$$\delta S = \frac{E - \varepsilon_F}{T} \delta N \quad (7.3)$$

In writing this expression it is also assumed that the reservoirs are sufficiently large that the change in temperature of the reservoir upon the addition of δN

electrons in very small compared to the temperature of the reservoir, that is, $\delta T \ll T$.

Electron transport through the energy filter does not contribute to the change in entropy of the composite system as it has been assumed to take place elastically. This means that there is no change in the energy of the electrons traversing the filter, so no heating and thus no increase in entropy of the system occurs in the filter. If \dot{N} is the rate at which electrons with total energy E flow *from* the cold reservoir in the ESE heat engine *to* the hot reservoir, then the change in entropy of the system per unit time is

$$\dot{S}_{tot} = \left[\frac{E - \varepsilon_H}{T_H} - \frac{E - \varepsilon_C}{T_C} \right] \dot{N}. \quad (7.4)$$

Two important results follow from Equation 7.4. The first is that Equation 7.4 changes sign at an energy which will be denoted E_0 , given by

$$E_0 \equiv \frac{T_H \varepsilon_C - T_C \varepsilon_H}{T_H - T_C}. \quad (7.5)$$

This means that the transfer of electrons with energy E_0 between the two reservoirs is a reversible process, resulting in no increase of the entropy of the composite system. In the next section it will be shown that, physically, E_0 is the energy at which the Fermi distributions in the two reservoirs cross. If allowed to interact only through the exchange of electrons with this energy, the reservoirs will remain in a state of quasi- or unstable equilibrium with each other, even though they have different temperatures and chemical potentials.

The second result is that Equation 7.4 specifies the thermodynamically spontaneous direction for electron flow between the reservoirs as a function of energy. For energies larger than E_0 , the expression in the brackets is positive. This means that electrons with energies larger than E_0 must spontaneously flow from the hot to the cold reservoirs, so $\dot{N} > 0$ for $E > E_0$. For energies less than E_0 the expression in the brackets is negative, so electrons with these energies must, in fact, flow spontaneously from the cold to the hot reservoirs in order to obey the second law of thermodynamics, which requires that $\dot{S}_{tot} \geq 0$.

7.2.2 Number Flux between Electron Reservoirs

We will at this stage assume a specific model for our energy filter, that it is an idealised quantum dot connected to the two electron reservoirs via 1D leads. Datta notes on page 248 of [40] that if the dimensions of a quantum dot are small enough that only one resonant state lies between the Fermi energies in the adjacent reservoirs, "the structure then acts as a filter that only lets electrons with energy E transmit".

In §6.3 a potential profile was assumed for the asymmetric quantum dot which was analysed, and the transmission probability calculated for this potential under the assumption of no electron-electron interactions. Here, the focus is not on the details of transport through quantum dots, but rather with determining the limiting efficiency and maximum power that could be obtained from a heat engine or refrigerator incorporating an energy filter realised using a quantum dot. *Idealised* quantum dots will therefore be assumed, in which the two tunnel barriers are exactly the same width, that is, the transmission probability and the tunnelling rates through the barriers are the same. This means that the transmission probability of the quantum dot may be set to unity over an infinitesimally small range of energies δE around the energy of the resonance E_R and zero elsewhere.

The Landauer equation, with a transmission probability of unity over the specified range of energies and zero elsewhere, will therefore be used to describe the theoretical maximum for the current through a quantum dot energy filter (in this energy range).

Over a very narrow energy range δE , the integral can be evaluated at energy E_R as

$$\dot{N}(E_R) = \frac{2}{h} [f_C(E_R, \varepsilon_C, T_C) - f_H(E_R, \varepsilon_H, T_H)] \delta E \quad (7.6)$$

Substituting Equation 7.6 into Equation 7.4 we can obtain an expression for

the total entropy flux of the composite system as

$$\dot{S}_{tot}(E_R) = \frac{2}{h} \left(\frac{E_R - \varepsilon_H}{T_H} - \frac{E_R - \varepsilon_C}{T_C} \right) \quad (7.7)$$

$$\left\{ \frac{1}{\left[1 + \exp \left(\frac{E_R - \varepsilon_C}{kT_C} \right) \right]} - \frac{1}{\left[1 + \exp \left(\frac{E_R - \varepsilon_H}{kT_H} \right) \right]} \right\} \delta E \quad (7.8)$$

Equation 7.7 shows that in the case of 1D-0D-1D ballistic transport through an infinitesimally narrow energy filter, between reservoirs at different temperatures and potential energies, both the number and entropy flux are zero at the energy where the occupation of states is the same in both reservoirs. This energy is given by Equation 7.5, easily obtained by solving Equation 7.7 for $\dot{S}_{tot}(E_R) = 0$. Whenever \dot{S}_{tot} is zero, heat is reversibly transported between the reservoirs, and operation of the heat engine does not increase the entropy of the system.

7.2.3 Heat Flux and Calculation of the Efficiency

In this section it will be explicitly demonstrated that the ESE heat engine can operate with Carnot efficiency as either a heat engine or a refrigerator. To calculate the efficiency, it is necessary to obtain an expression for the heat flux into each reservoir, \dot{Q} , which occurs upon a flux of \dot{N} electrons with energy E into the reservoir. As was done in §6.1, we use the first law of thermodynamics for an open system at constant volume and pressure [67]

$$\dot{U}_{C/H} = \dot{Q}_{C/H} + \mu_{C/H} \dot{N}. \quad (7.9)$$

The change in the internal energy of the cold reservoir is $\dot{U}_C = -E\dot{N}$ and that of the hot reservoir $\dot{U}_H = E\dot{N}$, and the chemical potentials $\mu_{C/H}$ can be approximated by the Fermi energies of the reservoirs if (as has been assumed so far) $kT_{C/H} \ll \varepsilon_{C/H}$. We can obtain an expression for $\dot{Q}_{C/H}$ (where C/H indicates the cold (C) or hot (H) reservoirs) from Equation 7.9 as

$$\dot{Q}_{C/H} = \mp (E - \varepsilon_{C/H}) \dot{N}. \quad (7.10)$$

Note that this is exactly equal to the entropy change of an electron reservoir upon a flux of \dot{N} electrons derived in Equation 7.3, multiplied by the temperature of the reservoir. That is, even though the exchange of electrons between the hot and cold reservoirs is in general not a reversible process, $\dot{Q}_{C/H} = T_{C/H} \dot{S}_{C/H}$ for this system as long as $kT_{C/H} \ll \varepsilon_{C/H}$.

Substituting the expression for the flux of electrons between the reservoirs given by Equation 7.6 into Equation 7.10, we can obtain an expression for the heat change per unit time in each of the reservoirs as a function of the energy of the filter E_R as

$$\dot{Q}_C = -\frac{2}{h}(E_R - \varepsilon_C)(f_C - f_H)\delta E \quad (7.11)$$

$$\dot{Q}_H = \frac{2}{h}(E_R - \varepsilon_H)(f_C - f_H)\delta E \quad (7.12)$$

The negative sign appears in Equation 7.11 as the electron flux, \dot{N} , is defined as positive for electrons flowing from the cold to the hot reservoir.

The heat engine operates using heat, \dot{Q}_H , from the hot reservoir to transport electrons up the potential gradient to the cold reservoir, depositing some waste heat, \dot{Q}_C , into the cold reservoir at the same time. Its efficiency, η_{HE} , is defined as the ratio of the work output to the heat input. The work done is given by the difference between the heat removed from the hot reservoir and the heat deposited into the cold reservoir, $-(\dot{Q}_H + \dot{Q}_C)$. For a monoenergetic filter, the efficiency is then given by

$$\eta_{HE} = \frac{\varepsilon_C - \varepsilon_H}{E_R - \varepsilon_H} \quad (7.13)$$

The numerator of the expression in Equation 7.13 is just the difference in the Fermi energies of the reservoirs. It is the amount of work done by the ESE heat engine every time an electron is transmitted against the potential gradient between the reservoirs. This work is done by drawing heat from the hot reservoir equal to the difference between the energy of the electron transmitted and the Fermi energy of the hot reservoir, and this factor appears as the denominator.

When the device is behaving as a refrigerator, electrons following the potential gradient from the cold to the hot reservoir remove heat, $-Q_C$, from the cold reservoir and deposit it in the hot reservoir at the expense of a reduction in their potential energy. The coefficient of performance of the device as a refrigerator is given by the ratio of the heat removed from the cold reservoir, and the work done to achieve this cooling, $\dot{Q}_H + \dot{Q}_C$, so that

$$\eta_R = \frac{E_R - \varepsilon_C}{\varepsilon_C - \varepsilon_H} \quad (7.14)$$

In this expression, the numerator is the heat removed from the cold reservoir per electron with energy E transmitted from the hot to the cold reservoirs. The denominator is the work expended in achieving this cooling, and is equal to the potential energy lost by the electron travelling from the cold to the hot reservoirs, which is simply the difference in the Fermi energies of the reservoirs.

If the energy of the filter is set to the energy at which the Fermi distributions in the reservoirs are equal (Equation 7.5), $E_R = E_0 \equiv (T_H \varepsilon_C - T_C \varepsilon_H)/(T_H - T_C)$, then simple substitution of the expression for E_0 into Equations 7.13 and 7.14 yields the Carnot efficiencies of

$$\eta_{HE} = \frac{T_H - T_C}{T_H} = \eta_{HE}^{Carnot} \quad (7.15)$$

and

$$\eta_R = \frac{T_C}{T_H - T_C} = \eta_R^{Carnot} \quad (7.16)$$

This demonstrates explicitly that the ESE heat engine can operate with Carnot efficiency at the energy at which the Fermi distributions in the reservoirs are equal, as implied from the demonstration of reversibility given in the previous section.

7.3 Maximum Power Regime of Operation

In the previous section, it was established that the ESE heat engine could operate with Carnot efficiency when the energy of an ideal filter is situated

where the Fermi distributions in the reservoirs are equal. However, at this filter energy the device operates with zero power, or in other words, quasi-statically (a necessary condition for reversible operation). This section will address the questions:

1. Under what conditions is the power of this device as a heat engine or refrigerator maximised?
2. What is the efficiency of the device under maximum power conditions?

In the first part of this section, expressions for the power and efficiency of the ESE heat engine when operated under maximum power conditions, will be derived analytically. In this regime of operation, transport in a large, clearly defined range of energies is allowed. The efficiency at maximum power is then compared with the Curzon-Ahlborn expression for the efficiency of an endoreversible heat engine operating at maximum power. The situation intermediate to maximum power and maximum efficiency will then be considered. In this regime, we assume a filter with a finite width that may be continuously varied from zero, to yield maximum efficiency, up to the width which yields maximum power. In final section of this chapter, the results obtained for the ESE heat engine in the maximum power regime will be compared with results obtained by Geva and Kosloff [116] for the three-level maser, an energy selective heat engine which utilises photons rather than electrons. It will be shown that although the fully quantum approach used to describe the dynamics of their system is very different to the semiclassical approach used to describe the ESE heat engine in this thesis, many of the results obtained in [116] can be easily reproduced for the ESE heat engine. It will be seen that the ESE heat engine and three-level amplifier appear to be the same *sort* of quantum heat engine, fundamentally different to the classical cyclical engines such as the Stirling, Otto, Brayton or Diesel heat engines which are generally well-described by endoreversible, finite-time thermodynamics.

7.3.1 Maximum Power Achievable with a 1D System

To determine the maximum power obtainable from an ESE heat engine it is noted that the power of the ESE heat engine over an infinitesimal energy range δE is given by

$$P_{HE}(E) = - \left[\dot{Q}_H(E) + \dot{Q}_C(E) \right] = -\frac{2}{h}(\varepsilon_C - \varepsilon_H)[f_C(E) - f_H(E)]\delta E \quad (7.17)$$

where $\dot{Q}_H(E)$ and $\dot{Q}_C(E)$ are the heat flux into the hot and cold electron reservoirs respectively. ε_H and ε_C are the Fermi energies of each reservoir and $f_C(E)$ and $f_H(E)$ are the Fermi distributions in the cold and hot reservoirs respectively. Similarly, the power of the ESE refrigerator is given by

$$P_R(E) = -\dot{Q}_C(E) = \frac{2}{h}(E - \varepsilon_C)[f_C(E) - f_H(E)]\delta E \quad (7.18)$$

If $P_{HE}/\delta E$ and $P_R/\delta E$ are plotted as a function of E , we can determine which electrons (as a function of their total energy) contribute *positively* to the power of the system as a heat engine or refrigerator, and which electrons *reduce* the power. Maximum power per filter will be achieved when all electrons which contribute positively to the power are permitted to be transmitted, and all electrons which reduce the power are blocked. Figure 7.3 shows a plot of Equations 7.17 and 7.18 for system parameters $T_C = 1$ K and $T_H = 2$ K and $(\varepsilon_C - \varepsilon_H)/k = 2$ K, where k is Boltzmann's constant, as a function of the energy of electrons relative to the Fermi energy of the cold reservoir in units of temperature, $(E - \varepsilon_C)/k$. The units of temperature were chosen for convenience, to allow easy comparison between the relative magnitudes of the thermal and potential gradients. These particular temperatures and Fermi energies were chosen as appropriate parameters for a cryogenic electron refrigerator. These parameters are, of course, not those which would be chosen for operating the device as a heat engine. However the figures shown are simply intended to illustrate the analytic work, and any temperature range could have been chosen for this purpose.

For the chosen parameter set, $(E_0 - \varepsilon_C)/k = 2$ K, and this value is marked on Figure 7.3. It can be seen that $P_{HE}/\delta E$ and $P_R/\delta E$ are pos-

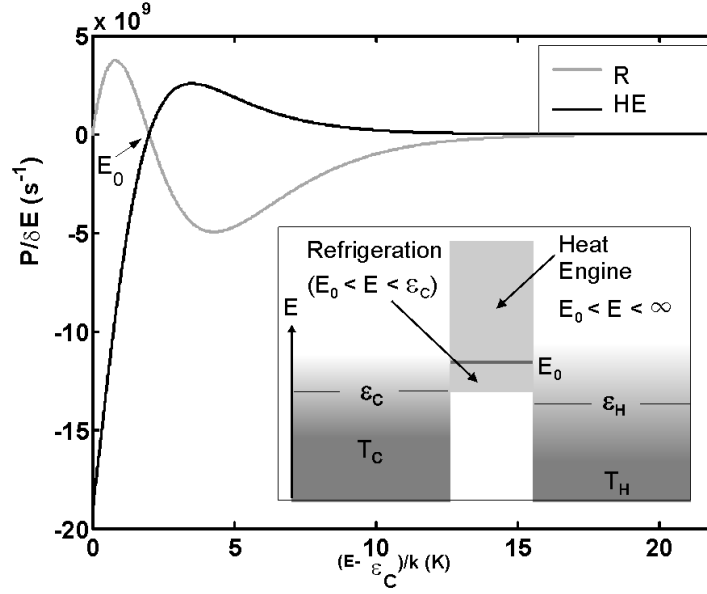


Figure 7.3: Inset: A schematic of the energy ranges of electrons which contribute positively to the power of the device as either a refrigerator or heat engine. Main: $P/\delta E$ as a function of the potential gradient in units of temperature, $(E - \varepsilon_C)/k$, for reservoir temperatures $T_H = 2$ K, $T_C = 1$ K, $(\varepsilon_C - \varepsilon_H)/k = 2$ K and $\varepsilon_C/k = 12$ K. In this figure ‘R’ stands for the refrigerating power of the device and ‘HE’ for the power as a heat engine. Electrons with total energies in the range $\varepsilon_C < E < E_0$ contribute positively to the power of the device as a refrigerator, and negatively to the power of the device as a heat engine. The opposite is true for electrons with energies in the range $E_0 < E < \infty$, they contribute positively to the power of the device as a heat engine and negatively to its power as a refrigerator. To obtain the maximum power from the ESE heat engine, all electrons with energies higher than E_0 should participate in transport, while all electrons with energies below this should be blocked. Conversely, to obtain maximum power from the ESE refrigerator, only electrons with energies between the ε_C and E_0 should contribute to the current, and all others blocked.

itive in the ranges $E > E_0$, and $\varepsilon_C < E < E_0$ respectively. It is clear that maximum power for the system as heat engine or refrigerator will be achieved when all electrons with total energies within these respective ranges are transmitted and no others. This maximum power can then be expressed as

$$P_{HE}^{\max}(E) = -\frac{2}{h} \int_{E_0}^{\infty} (\varepsilon_C - \varepsilon_H) [f_C(E) - f_H(E)] dE \quad (7.19)$$

$$P_R^{\max}(E) = \frac{2}{h} \int_{\varepsilon_C}^{E_0} (E - \varepsilon_C) [f_C(E) - f_H(E)] dE \quad (7.20)$$

These integrals yield the maximum power in the particular case where the magnitudes of the potential and thermal gradients, $\varepsilon_C - \varepsilon_H$ and $kT_H - kT_C$ respectively, may be chosen *independently*. Both the integrals in Equations 7.19 and 7.20 may be solved analytically. The derivation has been placed in Appendix I, as it is somewhat lengthy. The analytic solutions for the power and the efficiency of the device as a heat engine at maximum power are (from Appendix I)

$$P_{HE}^{\max} = -\frac{2}{h} (kT_H - kT_C)^2 \gamma_0 \ln \left(\frac{\exp(\gamma_0)}{1 + \exp(\gamma_0)} \right) \quad (7.21)$$

$$\eta_{HE}^{\max} = \frac{1 - \tau}{1 + \tau} \frac{-\gamma_0 \ln \left(\frac{\exp(\gamma_0)}{1 + \exp(\gamma_0)} \right)}{\left[\frac{1}{2} \left[\ln \left(\frac{\exp(\gamma_0)}{1 + \exp(\gamma_0)} \right) \right]^2 + \text{di} \log \left(\frac{\exp(\gamma_0)}{1 + \exp(\gamma_0)} \right) - \frac{1}{1 + \tau} \gamma_0 \ln \left(\frac{\exp(\gamma_0)}{1 + \exp(\gamma_0)} \right) \right]} \quad (7.22)$$

where the notation $\gamma_0 = (\varepsilon_C - \varepsilon_H)/(kT_H - kT_C)$ and $\tau = T_C/T_H$ has been introduced to simplify the appearance of the equations. The power of the device as a refrigerator in the maximum power regime is given analytically

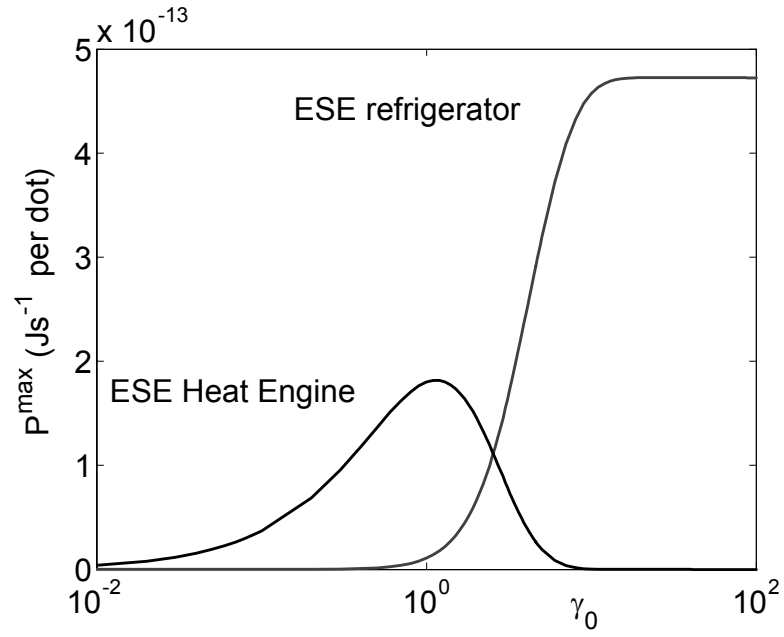


Figure 7.4: The maximum power of the ESR as a heat engine and refrigerator calculated numerically as a function of γ_0 , the ratio of the potential gradient to the thermal gradient. The reservoir temperatures are $T_H = 2$ K and $T_C = 1$ K.

by

$$P_R^{\max} = \frac{2}{h} \left[\begin{aligned} & -\gamma_0 k T_C (k T_H - k T_C) \ln \left(\frac{\exp(\gamma_0)}{1 + \exp(\gamma_0)} \right) \\ & + [(k T_H)^2 - (k T_C)^2] \left[\frac{1}{2} \left[\ln \left(\frac{\exp(\gamma_0)}{1 + \exp(\gamma_0)} \right) \right]^2 + \text{di log} \left(\frac{\exp(\gamma_0)}{1 + \exp(\gamma_0)} \right) \right] \\ & + (k T_C)^2 \left[\frac{1}{2} \left[\ln \left(\frac{1}{2} \right) \right]^2 + \text{di log} \left(\frac{1}{2} \right) \right] \\ & - (k T_H)^2 \left[\frac{1}{2} \left[\ln \left(\frac{\exp[(\varepsilon_C - \varepsilon_H)/k T_H]}{1 + \exp[(\varepsilon_C - \varepsilon_H)/k T_H]} \right) \right]^2 \right. \\ & \quad \left. + \text{di log} \left(\frac{\exp[(\varepsilon_C - \varepsilon_H)/k T_H]}{1 + \exp[(\varepsilon_C - \varepsilon_H)/k T_H]} \right) \right] \end{aligned} \right] \quad (7.23)$$

and the efficiency by

$$\eta_R^{\max} = \left[\frac{P_R^{\max}}{\dot{Q}_R} \right] \quad (7.24)$$

where

$$\dot{Q}_R = \frac{2}{h} (k T_H - k T_C)^2 \gamma_0 \ln \left(\frac{\exp(\gamma_0)}{1 + \exp(\gamma_0)} \right) \quad (7.25)$$

$$- \frac{2}{h} (k T_H - k T_C) \gamma_0 \left[\begin{aligned} & k T_H \ln \left(\frac{\exp[(\varepsilon_C - \varepsilon_H)/k T_H]}{1 + \exp[(\varepsilon_C - \varepsilon_H)/k T_H]} \right) \\ & - k T_C \ln \left(\frac{1}{2} \right) \end{aligned} \right] \quad (7.26)$$

P_{HE}^{\max} , P_R^{\max} , η_{HE}^{\max} and η_R^{\max} , calculated numerically from Equations 7.19 and 7.20, and corresponding equations for the efficiency, are plotted in Figures 7.4 and 7.5 as a function of γ_0 for reservoir temperatures of $T_H = 2$ K and $T_C = 1$ K. The behaviour in these Figures may be compared to that predicted analytically for limiting values of γ_0 , as discussed in the next sections.

Limiting behaviour of the power for heat engine operation

It can be seen in Figure 7.4 that the power of the ESE heat engine exhibits a maximum at a finite value of γ_0 , slightly larger than unity, and goes to zero for both small and large values of γ_0 . The existence of a maximum is to be expected, as if γ_0 is zero, no useful work is done by the device even though electrons are transported from the hot to the cold reservoirs (this is equivalent to short circuit conditions). If γ_0 tends to infinity, then the engine ‘stalls’ with the potential difference being too large compared to the

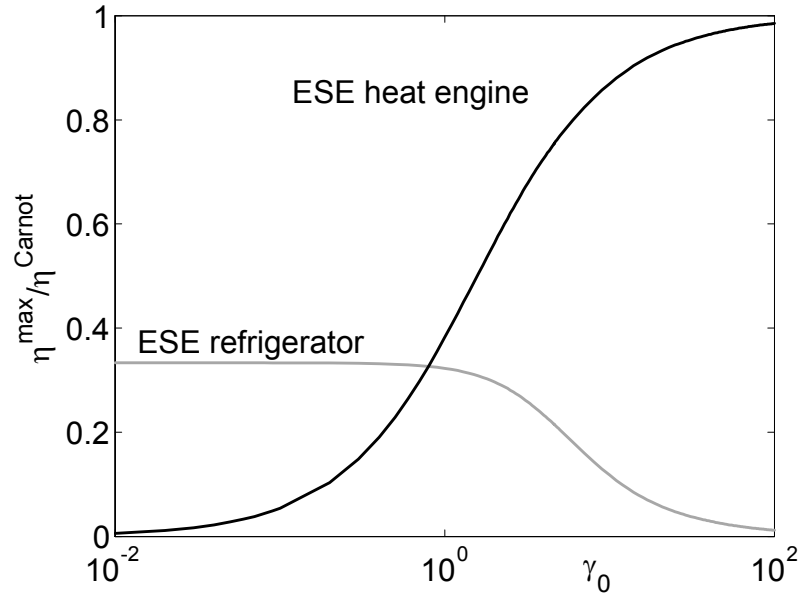


Figure 7.5: The efficiency of the ESR as a heat engine and refrigerator calculated as a function of $(\varepsilon_C - \varepsilon_H)/k$ for $T_C = 1$ K and $T_H = 2$ K. It can be seen that the efficiency of the ESR as a heat engine tends to zero for small values of $(\varepsilon_C - \varepsilon_H)$, and tends to the Carnot value of $T_H/(T_H - T_C) = 1/2$ for large values of $(\varepsilon_C - \varepsilon_H)$. The efficiency of the device as a refrigerator tends to one-third of the Carnot value $(1/3)T_C/(T_H - T_C) = 1/3$ for small values of $(\varepsilon_C - \varepsilon_H)$.

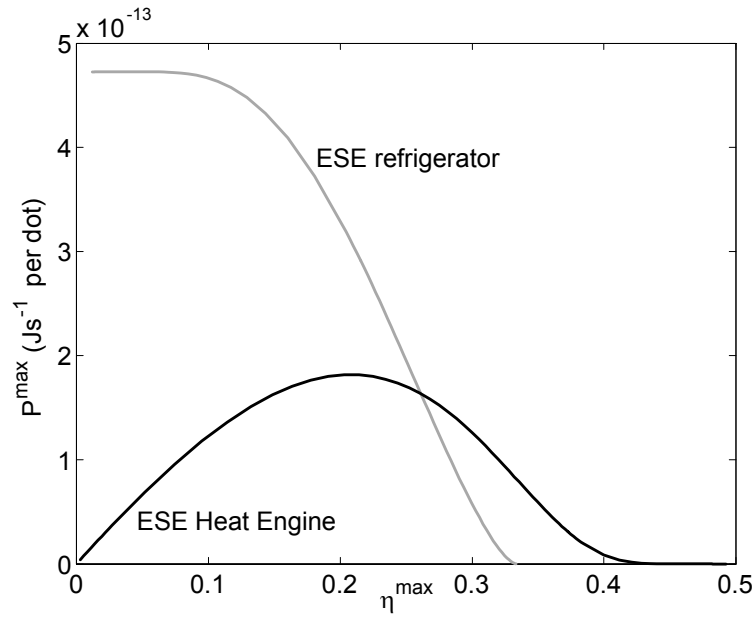


Figure 7.6: The maximum power in Figure 7.4 plotted against the efficiency from Figure 7.5. This figure explicitly shows that the ESE heat engine may be operated at the same power with two different efficiencies, indicating that it is best to choose a ratio of potential to thermal gradients which is greater than or equal to that at which the maximum occurs in Figure 7.4. The ESE refrigerator curve however, is monotonic, so there is no optimum value of $(\varepsilon_C - \varepsilon_H)/(kT_H - kT_C)$. Power is maximised when the efficiency is minimised, and vice-versa.

temperature difference for electrons to be transported against it (open circuit conditions).

The limiting behaviour of the power may also be analysed analytically as follows.

If $(\varepsilon_C - \varepsilon_H) \rightarrow 0$ then by noting that

$$\lim_{x \rightarrow 0} [x \ln (\exp (x) / (1 + \exp (x)))] = 0 \quad (7.27)$$

it can be shown that Equation 7.21 will tend to zero, that is,

$$\lim_{(\varepsilon_C - \varepsilon_H) \rightarrow 0} P_{HE}^{\max} = 0 \quad (7.28)$$

If $(\varepsilon_C - \varepsilon_H) \rightarrow \infty$, and given that

$$\lim_{x \rightarrow \infty} [\ln (\exp (x) / (1 + \exp (x)))] = 0 \quad (7.29)$$

it can also be shown that Equation 7.21 will again tend to zero in this limit.

$$\lim_{(\varepsilon_C - \varepsilon_H) \rightarrow \infty} P_{HE}^{\max} = 0 \quad (7.30)$$

Between these extremes of potential gradient, the power reaches a maximum value, given by the potential gradient for which the derivative of Equation 7.21 with respect to $(\varepsilon_C - \varepsilon_H)$ is zero. The result, after some algebra, and given that $\gamma_0^{\max} = (\varepsilon_C - \varepsilon_H)^{\max} / (kT_H - kT_C)$, where $(\varepsilon_C - \varepsilon_H)^{\max}$ is the potential gradient for which Equation 7.21 is maximised, we obtain the following closed form for the solution

$$\gamma_0^{\max} = -[1 + \exp (\gamma_0^{\max})] \ln \left[\frac{\exp (\gamma_0^{\max})}{1 + \exp (\gamma_0^{\max})} \right] \quad (7.31)$$

This expression may be solved numerically to yield

$$\gamma_0^{\max} \approx 1.1446 \quad (7.32)$$

Limiting behaviour of the efficiency for heat engine operation

It is expected that in the short-circuit limit, where $\gamma_0 = 0$, the efficiency will go to zero as the device does no useful work, but still removes heat

from the hot reservoir. In the open-circuit limit, where the device operates quasistatically and no electrons are transported, $\gamma_0 = \infty$, it is expected that the device should also operate reversibly. It is interesting to note that, as discussed in the introduction (§5.3), Carnot efficiency has been predicted for the diffusive analogue of the ESE heat engine, the Büttiker-Landauer model, by Derenyi and Astumian [96] in the quasistatic limit of infinitely high barriers (under certain conditions).

To derive these limits analytically for the ESE heat engine, note that Equation 7.22 can be written as

$$\eta_{HE}^{\max}(\gamma_0) = \frac{A(\gamma_0)(1 - \tau)}{1 + A(\gamma_0) + \tau} \quad (7.33)$$

where

$$A(\gamma_0) = \frac{-\gamma_0 \ln \left(\frac{\exp(\gamma_0)}{1 + \exp(\gamma_0)} \right)}{\frac{1}{2} \left[\ln \left(\frac{\exp(\gamma_0)}{1 + \exp(\gamma_0)} \right) \right]^2 + \text{di log} \left(\frac{\exp(\gamma_0)}{1 + \exp(\gamma_0)} \right)} \quad (7.34)$$

Given that

$$\lim_{x \rightarrow 0} [\text{di log}(\exp(x) / (1 + \exp(x)))] = -\ln(1/2)^2 / 2 + \pi^2 / 12 \quad (7.35)$$

it may be seen that in the limit of $(\varepsilon_C - \varepsilon_H) \rightarrow 0$, the efficiency given by Equation 7.33 tends to zero

$$\lim_{(\varepsilon_C - \varepsilon_H) \rightarrow 0} \eta_{HE}^{\max} = 0 \quad (7.36)$$

Given that

$$\lim_{x \rightarrow \infty} [\text{di log}(\exp(x) / (1 + \exp(x)))] = 0 \quad (7.37)$$

it can be shown that in the limit that $(\varepsilon_C - \varepsilon_H) \rightarrow \infty$, that Equation 7.33 for the efficiency of the ESE heat engine tends to the Carnot value of $1 - \tau$.

$$\lim_{(\varepsilon_C - \varepsilon_H) \rightarrow \infty} \eta_{HE}^{\max} = 1 - \tau \quad (7.38)$$

Using the numerical value of γ_0^{\max} to fix the ratio of potential to thermal gradients to that which maximises the power, an expression can be obtained

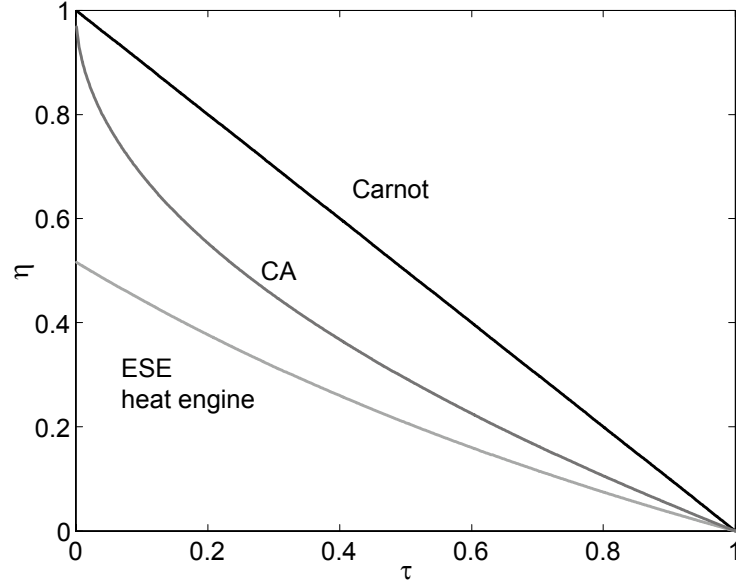


Figure 7.7: The maximum power of the ESE heat engine per filter, given by Equation 7.39, is shown, together with the Carnot efficiency and the Curzon-Ahlborn efficiency (marked CA) for comparison.

for the efficiency of the ESE heat engine in terms of the ratio of reservoir temperatures τ as

$$\eta_{HE}^{\max}(\gamma_0^{\max}) = \frac{A(\gamma_0^{\max})(1 - \tau)}{1 + A(\gamma_0^{\max}) + \tau} \quad (7.39)$$

where

$$A(\gamma_0^{\max}) = \frac{-\gamma_0^{\max} \ln \left(\frac{\exp(\gamma_0^{\max})}{1 + \exp(\gamma_0^{\max})} \right)}{\frac{1}{2} \left[\ln \left(\frac{\exp(\gamma_0^{\max})}{1 + \exp(\gamma_0^{\max})} \right) \right]^2 + \text{di} \log \left(\frac{\exp(\gamma_0^{\max})}{1 + \exp(\gamma_0^{\max})} \right)} \quad (7.40)$$

$$\approx 1.0685 \quad (7.41)$$

Once the ratio of the potentials has been fixed, the efficiency of the ESE heat engine depends only upon the ratio of the reservoir temperatures. In this regime it is always smaller than the Carnot efficiency, $1 - \tau$. A plot of $\eta_{HE}^{\max}(\gamma_0^{\max})$ as a function of τ is shown in Figure 7.7 together with the Carnot

efficiency, and the Curzon-Ahlborn (CA) efficiency for an endoreversible heat engine, $\eta^{CA} = 1 - \sqrt{\tau}$, for comparison.

Is the ESE Heat Engine Endoreversible?

The CA efficiency was described in §5.4.2, but will be briefly discussed again here for the convenience of the reader. The Curzon-Ahlborn efficiency accurately describes the efficiency at maximum power of many types of heat engines (e.g. Stirling, Otto, Brayton or Diesel) in which there is a finite temperature difference between the working substance and the temperature reservoirs, which allows the engine to perform work in a finite amount of time. The internal working of the Curzon-Ahlborn heat engine is assumed to be reversible, that is, there is no entropy generated by the working gas moving through its cycle of compression and expansion. Such an engine, where the only irreversibilities arise through interaction with the external heat reservoirs is generally called an *endoreversible* heat engine. It is described by the Curzon-Ahlborn efficiency when the rate of heat transfer is linearly dependent upon the difference between the working gas and each reservoir. In such a heat engine the temperatures of the reservoirs can be significantly different, but heat is transferred between them via a working gas whose temperature is always intermediate to the temperatures of the reservoirs.

In contrast to the case for conventional cyclic heat engines, in the ESE heat engine the hot and the cold reservoirs exchange heat *directly* via the transfer of electrons with a well-defined range of energies. No temperature can be defined for these electrons, as their energy distribution is not described by a Fermi function. The efficiency *at maximum power* of the ESE heat engine cannot, therefore, be expected to approach the Carnot value for small τ , as this situation involves reservoirs at radically different temperatures directly exchanging heat. In fact, the efficiency differs dramatically from both the CA and Carnot values in this limit, $\eta_{HE}^{\max} \rightarrow 0.512$ while $\eta^{CA} \rightarrow \eta^{Carnot} = 1$ as $\tau \rightarrow 0$. In the case where the ratio of reservoir temperatures tends to unity, that is, the temperature difference approaches zero,

the efficiency of the ESE heat engine tends to zero linearly in τ , as does the Carnot efficiency, while the CA efficiency tends to zero faster, as $\sqrt{\tau}$.

In summary, the ESE heat engine is not endoreversible, in that it does not consist of an internally reversible cycle with all irreversibilities linked to the interaction of a working gas with heat reservoirs. Rather, in the ESE heat engine, the reservoirs interact *directly*, exchanging electrons in a particular range of energies with each other, making it quite distinct from conventional cyclic engines. It will be seen in a later section that the ESE heat engine shares this characteristic with another energy selective engine, the three-level amplifier.

It is important to note that here the maximum power regime is defined as is the maximum power per energy filter. Any implementation of the ESE heat engine would be likely to include many such quantum dots or energy filters, so the power obtained from such a device per unit area would depend upon the density of filters or quantum dots. The same power could in principle be obtained from a low density of quantum dots with very broad resonances, or a higher density of quantum dots with narrow resonances. The latter setup would operate at a higher efficiency, limited in principle only by the Carnot value, while the former would be limited to a lower efficiency, as shown by the above discussion.

Figure 7.8 shows the maximum power of the ESE heat engine per quantum dot for a range of thermal gradients, when $\gamma_0 = \gamma_0^{\max} \approx 1.1446$ is substituted into Equation 7.21.

Limiting behaviour of the power for refrigerator operation

The performance of the ESE refrigerator will now be analysed in the same limiting regimes as the ESE heat engine. The power of the ESE refrigerator (shown in Figure 7.4) must tend to zero for small γ_0 , as the window of energies for which the refrigerating power is positive, between ε_C and E_0 , closes as $\gamma_0 \rightarrow 0$. In the other limit, as $\gamma_0 \rightarrow \infty$, the ‘window’ between ε_C and E_0 tends to infinity, so the behaviour of the refrigerating power is not

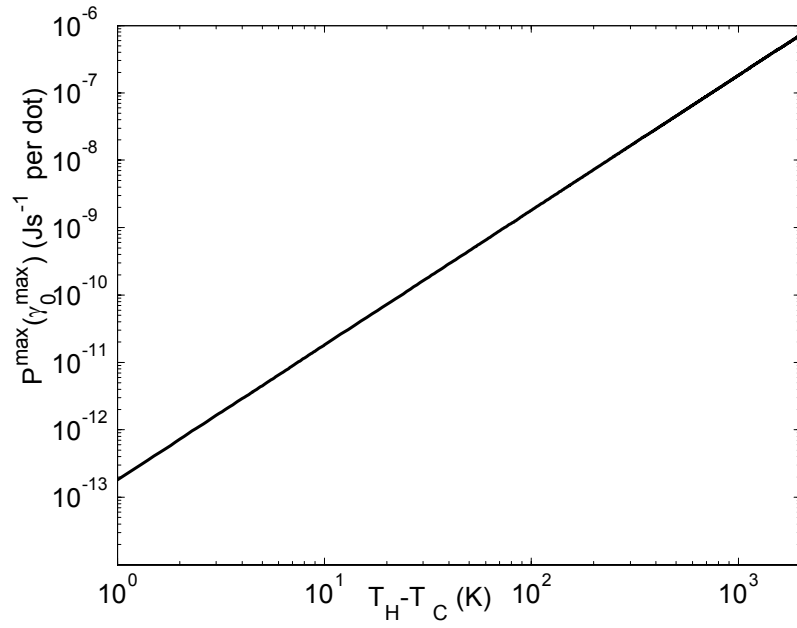


Figure 7.8: The maximum power of the ESE heat engine when $(\varepsilon_C - \varepsilon_H)/(kT_H - kT_C) = \gamma_0^{\max}$, as a function of the temperature difference, $T_H - T_C$. The power at $T_H - T_C = 1$ K equates to the maximum power shown in Figure 7.4 for the ESE heat engine for reservoir temperatures $T_H = 2$ K and $T_C = 1$ K.

so intuitively clear. It turns out that the power tends to a maximum value, for although the extra electrons removed from the cold reservoir in this limit remove a lot of heat due to their high energy, there are exponentially less of them to remove. This means that increasing γ_0 (essentially eV) beyond a certain limit does result in a corresponding improvement of the refrigerating power.

Writing this analytically, in the limit that $(\varepsilon_C - \varepsilon_H) \rightarrow 0$, Equation 7.23 will tend to zero as the potential gradient is not sufficiently large to remove heat from the hot reservoir.

$$\lim_{(\varepsilon_C - \varepsilon_H) \rightarrow 0} P_R^{\max} = 0 \quad (7.42)$$

In the limit $(\varepsilon_C - \varepsilon_H) \rightarrow \infty$ there is only one term in Equation 7.23 which does not go to zero, giving the analytic result

$$\lim_{(\varepsilon_C - \varepsilon_H) \rightarrow \infty} P_R^{\max} = k^2 T_C^2 \frac{2 \pi^2}{h 12}. \quad (7.43)$$

This limiting behaviour can be seen from the numerical solution, shown in Figure 7.4.

Limiting behaviour of the efficiency for refrigerator operation

The limiting behaviour of the efficiency at maximum power of the device as a refrigerator may also be examined. The software package Maple was used to evaluate the limit of equation 7.24 as $(\varepsilon_C - \varepsilon_H) \rightarrow 0$, which was found to be

$$\lim_{(\varepsilon_C - \varepsilon_H) \rightarrow 0} \eta_R^{\max} = \frac{1}{3} \left[\frac{\tau}{1 - \tau} \right] \quad (7.44)$$

in agreement with the trend observed in the numerical calculation shown in Figure 7.5. The physical reason for the factor of $1/3$ which appears multiplying the Carnot efficiency in Equation 7.44 is, as yet, not entirely clear. It may be that while the range of energies of the electrons which contribute to transport, $E_0 - \varepsilon_C$, does decrease as $\varepsilon_C - \varepsilon_H$ becomes small, reversible operation is still not approached, as electrons with energies at or very close

to ε_C which remove no heat from the cold reservoir but contribute to heating in the hot reservoir, are still transported. This may be contrasted with the situation which occurs when the device operates as a heat engine and $(\varepsilon_C - \varepsilon_H) / (kT_H - kT_C)$ is very large. As E_0 becomes large and the difference in the Fermi distributions becomes small, a vanishingly small number of electrons with a wide range of energies are transported, but every electron transported against the potential gradient performs a finite amount of useful work, and the efficiency approaches the Carnot value. It is, however, still very intriguing that the limiting efficiency of the device as a refrigerator should be exactly *one third* of Carnot efficiency as the potential gradient tends to zero.

The efficiency of the device as a refrigerator in the opposite limit, where $(\varepsilon_C - \varepsilon_H) \rightarrow \infty$, can be shown to be

$$\lim_{(\varepsilon_C - \varepsilon_H) \rightarrow \infty} \eta_R^{\max} = 0 \quad (7.45)$$

Although the power of the device tends to a finite value in this limit, the heat deposited in the hot reservoir tends to infinity, so that the ratio of these, the efficiency, tends to zero.

7.3.2 The Intermediate Case: Between Maximum Power and Maximum Efficiency

The next case analysed is that where electrons in a limited range of energies ΔE are transmitted, and where the central energy of the range, E_R , is the primary variable of the system. This regime can be understood to be intermediate to those of maximum efficiency and maximum power which were considered previously, as the width ΔE may be tuned to be small, thus yielding small power and high efficiency, or very wide, to yield high power and low efficiency. The situation resembles a resonance in a quantum dot, the central energy of which might be tunable with a gate voltage, as is the case in the quantum dot refrigerator envisaged by Edwards et al. [73, 82]. It is again assumed for simplicity that the transmission probability of electrons

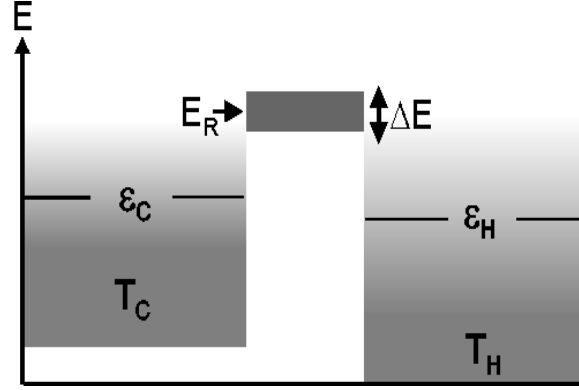


Figure 7.9: The second ‘maximum’ power scenario, in which the central energy, E_R , of a resonance of finite width, ΔE , is considered as the primary variable of the system.

will be equal to one over the range ΔE , and zero elsewhere. A more realistic assumption of a Lorentzian transmission probability can also be used [97]. The same qualitative behaviour is obtained, however results such as the location of the power maximum are not as straightforward to interpret as they are with a ‘rectangular’ shaped transmission function as used here.

To find the power in this situation, Equations 7.17 and 7.18 are integrated between the limits $E_R - \Delta E/2$ and $E_R + \Delta E/2$ to yield

$$P_{HE}^R(E_R) = \frac{2}{h} \int_{E_R - \Delta E/2}^{E_R + \Delta E/2} (\varepsilon_C - \varepsilon_H) [f_C(E) - f_H(E)] dE \quad (7.46)$$

and

$$P_R^R(E_R) = \frac{2}{h} \int_{E_R - \Delta E/2}^{E_R + \Delta E/2} (E - \varepsilon_C) [f_C(E) - f_H(E)] dE \quad (7.47)$$

A numerical calculation of the resulting power and efficiency as a function of E_R was performed for the same values of temperature and Fermi energies as were used in the previous section ($T_C = 1$ K, $T_H = 2$ K, $\varepsilon_C/k = 12$ K and $\varepsilon_H/k = 10$ K), and are shown in Figures 7.10 and 7.11 for three different resonance widths, $\Delta E/k = 0.5$ K, $\Delta E/k = 2$ K and $\Delta E/k = 3.5$ K.

In Figure 7.10, the three curves on the left represent the range of E_R for which the device is behaving as a refrigerator while the three on the right

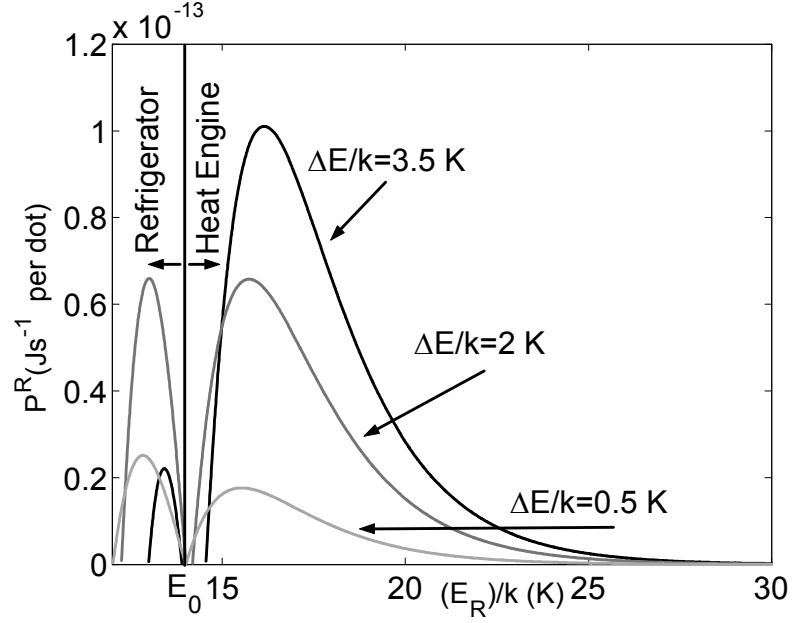


Figure 7.10: The power of the ESR as a function of E_{res} , for $\Delta E/k = 0.5$ K, $\Delta E/k = 2$ K and $\Delta E/k = 3.5$ K. For $12 \text{ K} > E_R/k < 14 \text{ K}$ refrigeration can occur while for $E_R/k > 14 \text{ K}$ the device behaves as a heat engine. These two regimes of operation are marked on the figure by the vertical line at $E_R/k = 14 \text{ K}$. Note that for the ESE heat engine, increasing the width of the resonance increases the maximum power (up to the limit given in §7.3.1) and the maximum moves to higher values of E_R . This occurs because as the width increases, the resonance has to move to higher values of energy so as not to allow transport of electrons with energies which reduce the power, as was illustrated by Figure 7.3. In the case of the ESE refrigerator, increasing the width of the resonance only increases the power up to a certain value (which is determined by the potential and thermal gradients according to the previous section). For larger widths, the power decreases, as electrons with energies which decrease the power are necessarily included in the current. If the central energy of the finite width resonance is placed close to E_0 , then a situation can exist in which no useful work is done, and both the power and the efficiency are undefined (negative).

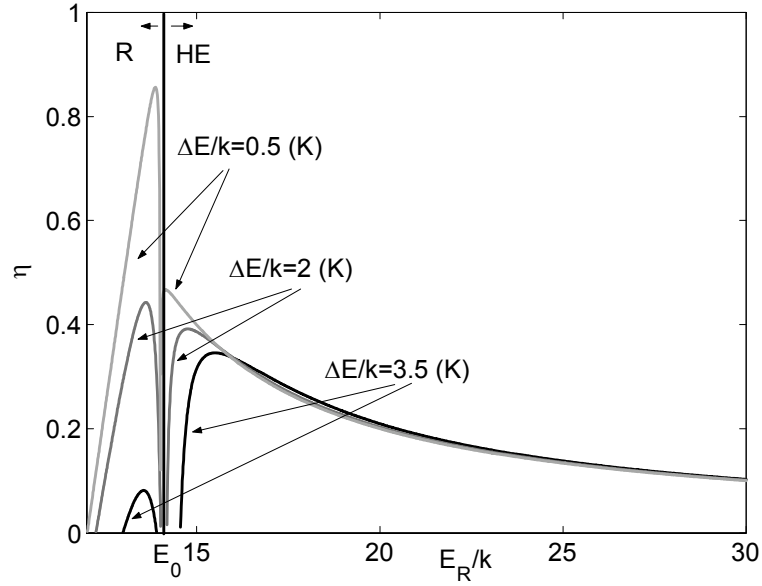


Figure 7.11: The efficiency of the ESE refrigerator and heat engine for the same parameters as in Figure 7.10. Note that the same ‘window’ appears around E_0 for the largest value of ΔE as was seen in Figure 7.10.

represent the range of E_R for which the device is behaving as a heat engine (the same can be seen in Figure 7.11).

It can be seen that wider resonances decrease the range of E_R for which the device can perform useful work, forming gaps around $E_0/k = 14$ K in the power and efficiency curves for $\Delta E/k = 3.5$ K. These gaps occur when the resonance samples a range of energies where some electrons contribute to refrigeration while others contribute to heat engine behaviour such that no useful work is done, even though energy is still expended.

When the resonance is very narrow, reversible behaviour is approached, the power becomes small and the efficiency tends to the Carnot value (for $T_C = 1$ K and $T_H = 2$ K, $\eta_{HE}^C = 0.5$ and $\eta_R^C = 1$). Increasing the width of the resonance increases the power of the ESE heat engine, with an upper bound as derived in §7.3.1. For the ESE refrigerator the power can only be increased to a finite value due to the finite range of energies which contribute positively

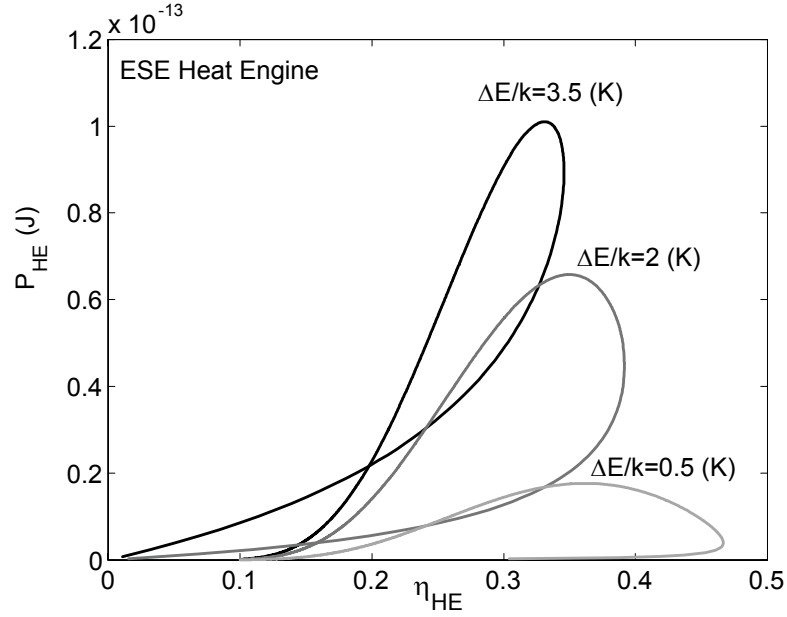


Figure 7.12: A plot of the power of the ESE heat engine versus its efficiency. This plot shows the "loop" shape characteristic of irreversible systems. The data is the same as that shown in the right-hand sides of Figures 7.10 and 7.11. It can be seen that as the width of the resonance increases, the power increases while the efficiency decreases.

to refrigeration power. The range of refrigeration energies can however be increased arbitrarily by decreasing the difference between T_H and T_C (kept constant in this analysis).

The maxima in the efficiency curves always corresponds to the situation when the lower edge of the resonance is placed on E_0 , that is, when $E_R = E_0 + \Delta E/2$. For wide resonances, the value of E_R which maximises the power is the same, $E_R = E_0 + \Delta E/2$. For narrow resonances however, maximum power occurs when E_R is centred on the energy for which Equations 7.17 and 7.18 are maximised. As shown in Figure 7.3, this occurs at electron energies slightly higher and lower than E_0 respectively.

Plots of the power versus the efficiency in this regime show the "loop"

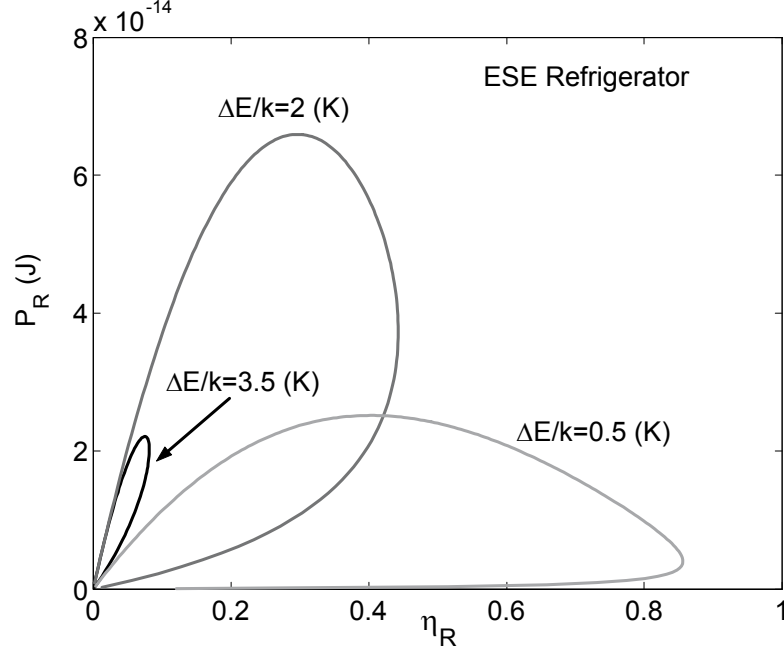


Figure 7.13: A plot of the power vs efficiency of the ESE refrigerator. For the smallest width resonance, $\Delta E/k = 0.5$ K, the maximum power reached by the loop is low, but the maximum efficiency high. For the intermediate width resonance, $\Delta E/k = 2$ K, the maximum power reached by the loop is high, but the maximum efficiency lower than for the narrower resonance. For the widest resonance, $\Delta E/k = 3.5$ K, both the maximum power and the maximum efficiency are low. This occurs because at this width, the resonance extends to energies above E_0 , where the device behaves as a heat engine, and to energies below ε_C , where the electrons do not remove any heat from the cold reservoir when they are transported to the hot reservoir. Both the power and efficiency go down as the device is doing less useful work in this situation.

shape which is characteristic of heat engines and refrigerators in which parameter sets exist for which both the power and the efficiency are zero. For the ESE heat engine and refrigerator this situation exists when heat engine and refrigeration behaviour is mixed by the transmission of electrons with energies both above and below E_0 between the reservoirs, or when electrons with energies both higher and lower than the Fermi energy of the cold reservoir are transmitted. Such situations were excluded from occurring in the maximum power regime analysed in the previous section, and the plot of the power versus the efficiency in that regime, Figure 7.6, did not show the loop shapes which can be seen in Figure 7.12.

The significance of this is that for the ESE heat engine, ‘loop-shaped’ power versus efficiency plots are *not* a signature of the maximum power regime of operation, even though transport *is* irreversible in this regime. Rather loop-shapes only occur in the non-optimum regime of operation discussed above, and result from the mixing of refrigerating and heat engine behaviour. This point emphasises the advantage of utilising energy selectivity to optimise the power produced, by only transporting electrons which are beneficial to the power.

7.3.3 Comparison with the Three-Level Amplifier

A three-level amplifier, or maser, system was first analysed as a heat engine by Scovil and Schulz-DuBois [117] in 1959, and is shown schematically in Figure 7.14. Since then Geva et al. [118, 116, 119] have examined how the irreversible thermodynamic performance of the three-level amplifier is influenced by the quantum nature of its dynamics. In this section, it will be shown that the 3-level amplifier and the ESE heat engine behave in an analogous manner, with the same relationship between refrigerating and heat engine behaviour as a function of the energy at which photons or electrons are exchanged with the hot and cold reservoirs. This indicates that some unified behaviour is expected for heat engines employing energy selectivity, irrespective of the particular dynamics of the system.

Reversible regime of operation

The three-level amplifier is shown schematically in Figure 7.14. The working substance consists of a gas of non-interacting three-level atoms. The relative occupations of the highest and lowest levels, u and g at energies E_u and E_g respectively, are determined by thermal contact with the hot reservoir, on the left in Figure 7.14. This thermal contact is provided by the exchange of photons with frequency $f = (E_u - E_g)/h$ through a narrow bandpass filter. The relative occupations of the middle and lowest level, d and g at energies E_d and E_g respectively, are determined by thermal contact with a colder reservoir, on the right, by exchange of photons at a frequency $f = (E_d - E_g)/h$. Work is done by the system via stimulated emission of photons with energy $(E_u - E_d)$ from level u to level d into a monochromatic radiation field, and will occur whenever population inversion exists between u and d . The system can operate in reverse as a refrigerator if work is done on the system by supplying photons of energy $(E_u - E_d)$ to excite electrons from d to u , removing heat $(E_d - E_g)$ from the cold reservoir and depositing heat $(E_u - E_g)$ into the hot reservoir. Reversible operation is achieved at point of inversion between u and d , that is, when the population of electrons occupying level u (determined by T_H) and that of level d (determined by T_C) is equal.

The three-level amplifier works in an analogous manner to the ESE heat engine. Particles at a single energy are extracted from a hot reservoir, so that an amount of heat $(E_u - E_g)$ is available to be converted into work. In the case of the ESE heat engine this amount of heat is $(E - \varepsilon_H)$. This means that level u in the three-level amplifier may be physically associated with the Fermi energy of the hot reservoir ε_H in the ESE heat engine, and level g in the three-level amplifier with the energy at which electrons are transmitted between the reservoirs. The amount of heat deposited into the cold reservoir is $(E_d - E_g)$ in the three-level amplifier, and $(E - \varepsilon_C)$ in the ESE heat engine, allowing level d in the three-level amplifier to be associated with the Fermi energy of the cold reservoir in the ESE heat engine.

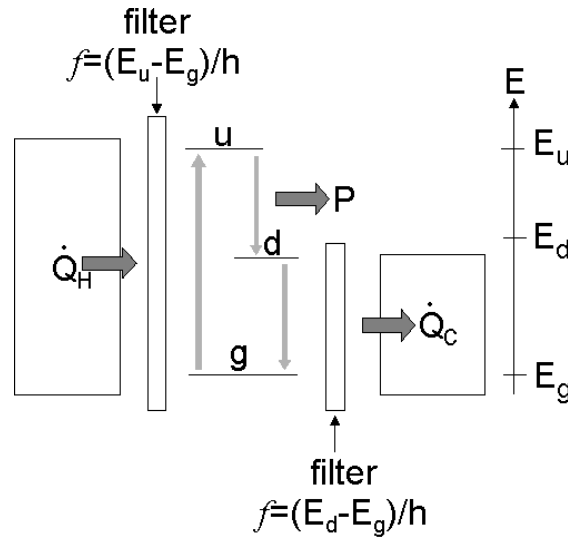


Figure 7.14: A schematic of the three-level amplifier. A gas of three-level atoms constitute a working substance. The u - g transition is in thermal contact with the hot reservoir through the exchange of photons with energy $(E_u - E_g)$. Similarly, the d - g transition is in thermal contact with a cold reservoir. When a population inversion is established between levels u and d , the system emits stimulated radiation with an energy $(E_u - E_d)$ into a radiation field of intensity ϵ , thus amplifying the field and doing useful work.

It can then easily be shown that the same relationship between the reservoir temperatures and the arrangement of the energy levels which yields the Carnot efficiency in the three-level amplifier also yields Carnot efficiency for the ESE heat engine.

The efficiency of the three-level amplifier as a heat engine is given by [117]

$$\eta_{HE}^{3L} = \frac{E_u - E_d}{E_u - E_g}. \quad (7.48)$$

Using the fact that ε_C may be associated with E_d and ε_H with E_u we can substitute $E_0 = (E_d T_H - E_u T_C) / (T_H - T_C)$ for E_g , obtaining

$$\eta_{HE}^{3L} = \frac{E_u - E_d}{E_u - \frac{E_d T_H - E_u T_C}{T_H - T_C}} \quad (7.49)$$

$$= \frac{T_H - T_C}{T_H} \quad (7.50)$$

$$= \eta_{HE}^{Carnot} \quad (7.51)$$

Maximum power regime of operation

We now compare the behaviour of both engines in the maximum power regime, with a number of results obtained for the ESE heat engine with a finite width resonance in §7.3.2, able to be mapped to results obtained for the three-level amplifier by Geva and Kosloff in [116].

Geva and Kosloff derive a generalized master equation describing the quantum dynamics of the three-level amplifier which remains thermodynamically consistent in the limit of very intense driving fields, thus improving on the work of Lamb [120]. They find that at very high field intensities, the levels d and u split, as shown in Figure 7.15, so that the behaviour of the three-level amplifier can be seen as being given by the combined output of two different amplifiers, one working between the lower of each of the split levels u and d and the ground level, and another working between the higher levels and ground. The energy of the splitting is determined by the field intensity through the Rabi frequency $\epsilon = \vec{\mu} \cdot \vec{E}_A$, where \vec{E}_A is the amplitude

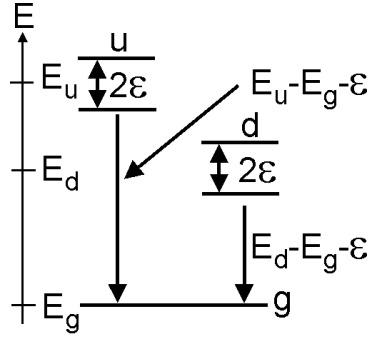


Figure 7.15: A schematic of the three-level amplifier under intense field amplitudes, showing the splitting of levels u and d .

of the driving field in Geva and Kosloff's model and $\vec{\mu}$ is the dipole moment of the u - d transition.

There is no analogous effect in the simple semiclassical model of the ESE heat engine presented in this thesis. However, it will be shown that the behaviour of the ESE heat engine as a function of the central energy of a finite width resonance can be matched to the behaviour of the three-level amplifier as a function of the level splitting, which depends upon the intensity ϵ of the monochromatic radiation field. There are two situations considered by Geva and Kosloff.

1. The first is for the low temperature limit where $\epsilon \gg T_C, T_H$, where the occupation of the higher of the split u and d levels may be neglected.

In this situation, the efficiency of the amplifier is just

$$\eta_{lT} = \frac{E_u - E_d}{(E_u - \epsilon) - E_g} \quad (7.52)$$

which has a maximum at

$$\epsilon_{\max}^{lT} = E_g - \frac{T_H E_d - T_C E_u}{T_H - T_C} \quad (7.53)$$

Physically, ϵ_{\max}^{lT} , defined in Equation 7.53, is the value of ϵ needed to achieve Carnot efficiency in the general case that $E_g \neq E_0$. If the energy

levels in the amplifier happened to be arranged with ‘ideal’ spacing so as to yield Carnot efficiency for the particular temperatures of the reservoirs, then ϵ_{\max}^{lT} would be equal to zero. Geva and Kosloff then consider four ranges of field intensity. The first, where $0 < \epsilon < \epsilon_{\max}^{lT}$ gives the range of field intensities for which the amplifier operates as a heat engine. If $\epsilon < \epsilon_{\max}^{lT}$, then this means that the energy difference between the ground and the higher levels d and u is larger than that which would yield Carnot efficiency. This corresponds exactly to the situation where the resonance in the ESE heat engine is higher than E_0 .

If the resonance is between ϵ_C and E_0 then the electron heat engine operates as a refrigerator. This is also the case for the three-level amplifier in the range $\epsilon_{\max}^{lT} < \epsilon < E_d$. As $T_C \rightarrow 0$, $\epsilon_{\max}^{lT} \rightarrow E_d$, and the refrigeration window closes for the three-level amplifier, as it does for the ESE refrigerator, with $E_0 \rightarrow \epsilon_C$ as $T_C \rightarrow 0$. The final two field intensity ranges considered for the amplifier are where $E_d < \epsilon < E_u$, and $E_u < \epsilon < \infty$, corresponding to $\epsilon_C < E < \epsilon_H$ and $\epsilon_H < E < 0$ for the electron heat engine, where no useful work is done in either device.

2. The second situation considered by Geva and Kosloff was the case where the bath temperatures are sufficiently large compared to ϵ that the higher of the split levels also contributes to the thermodynamic behaviour of the amplifier as the intensity of the field is increased.

As the field intensity is increased beyond ϵ_{\max}^{lT} in the model of the amplifier, the lower levels change from contributing positively to the power of the amplifier as a heat engine to refrigerating the cold reservoir, thus working against the higher levels which always operate as a heat engine. When the power of the higher levels as a heat engine equal that consumed by the lower levels which are operating as a refrigerator, both the output power and efficiency equal zero. The (almost) analogous situation in the ESE heat engine is that of a resonance sit-

uated above E_0 whose width may be increased arbitrarily. The difference between the two is that in the ESE heat engine all electrons with energies between the two extrema are transmitted, whereas in the three-level amplifier only photons with energies *at* the two energy levels are transmitted. The physical behaviour associated with each is however qualitatively the same. The curves shown in Figure 7.10 for $E_{res}/k = 13$ K display behaviour analogous to that seen for the amplifier, with increasing resonance width at constant E_R corresponding to decreasing power and efficiency (also see Figure 7.11).

The maximum power scenarios examined in this thesis for the ESE heat engine and refrigerator have not yet been examined for the three-level amplifier. One might reproduce these scenarios by considering the ground level of the three-level atoms to be a continuum of levels extending from $E_g = (E_d T_H - E_u T_C) / (T_H - T_C)$ down to $-\infty$ for operation as a heat engine or from E_d down to $(E_d T_H - E_u T_C) / (T_H - T_C)$ for operation as a refrigerator. It would be interesting to see if the results obtained for the ESE heat engine and refrigerator could then be reproduced for the three-level amplifier in the low field intensity limit originally considered by Lamb [120]. In the high field intensity situation, that considered by Geva and Kosloff, new behaviour not predicted for the ESE heat engine might be expected, as there is no physical analogue in the ESE heat engine for the level splitting in the three-level amplifier induced by high field amplitudes.

7.4 Conclusions

The main results of this chapter can be summarised as follows:

1. Energy Selective Electron (ESE) heat engines or refrigerators consisting of two reservoirs with different temperatures and potential energies linked via an infinitesimally narrow bandwidth ballistic energy filter can operate reversibly when the energy of the filter is set to the energy $E = E_0$, where the Fermi distributions in the two reservoirs are equal.

2. The efficiency of ESE heat engines and ESE refrigerators is limited only by the Carnot value.
3. Given free choice of both the potential and thermal gradients between the reservoirs, maximum power is obtained from the ESE heat engine when electrons with energies in the range $E_0 < E < \infty$ are transmitted between the reservoirs. To obtain maximum power from the ESE refrigerator, only electrons with energies in the range $\varepsilon_C < E < E_0$ must be transmitted between the reservoirs.
4. There exists a maximum in the power obtained from the ESE heat engine for a particular ratio of potential to thermal gradients. This ratio γ_0^{\max} is the solution to Equation 7.31, which may be solved numerically to obtain $\gamma_0^{\max} \approx 1.1446$. There is no equivalent maximum in the power of the ESE refrigerator, but rather the power tends towards the finite limit $P_R^{\max} = (\pi^2 k^2 T_C^2) / (6h)$ as the ratio of the potential to thermal gradients tends to infinity.
5. The efficiency of the ESE heat engine at the ratio of potential to thermal gradients γ_0^{\max} , is a function only of the ratio of the temperatures of the reservoirs, and is given by $\eta_{HE}^{\max}(\gamma_0^{\max}) = A(\gamma_0^{\max})(1 - \tau) / [A(\gamma_0^{\max}) + (1 + \tau)]$, where $A \approx 1.0685$. The ESE heat engine is not well-described by an endoreversible model in the maximum power regime, and its efficiency at maximum power $\eta_{HE}^{\max}(\gamma_0^{\max})$ differs significantly from both the Curzon-Alhborn and Carnot efficiencies.
6. The efficiency at maximum power of the ESE refrigerator tends to 1/3 of the Carnot value for very small values of γ_0 , and tends to zero for large values γ_0 .
7. The ESE heat engine and refrigerator operates in an analogous manner to the three-level amplifier, displaying similar behaviour in the maximum power regime.

Chapter 8

Outlook

In this final chapter, the implications of the results of Chapter 7 for thermionic and thermoelectric power generators and refrigerators are briefly explored.

8.1 Energy Filtering in Thermionic Power Generators and Refrigerators

As discussed in §5.2.2, thermionic power generators and refrigerators are electron heat engines which utilise an energy barrier to selectively transmit high energy electrons ballistically between reservoirs. Each electron transmitted must have a momentum in the direction of transport greater than some value k'_x , and so a minimum kinetic energy $E_{\min} = (\hbar k'_x)^2 / 2m^*$. The momentum of transmitted electrons in the other two dimensions is, however, unconstrained in conventional thermionic designs (they are 3D-2D-3D systems). The electrons transmitted in this situation may be represented by the shaded region on the left Fermi sphere in Figure 8.1, which shows in k-space the occupation of states of a free electron gas. The two points to note are that the energy spectrum of the current due to these electrons is

1. Broad
2. Dominated by high energy electrons.

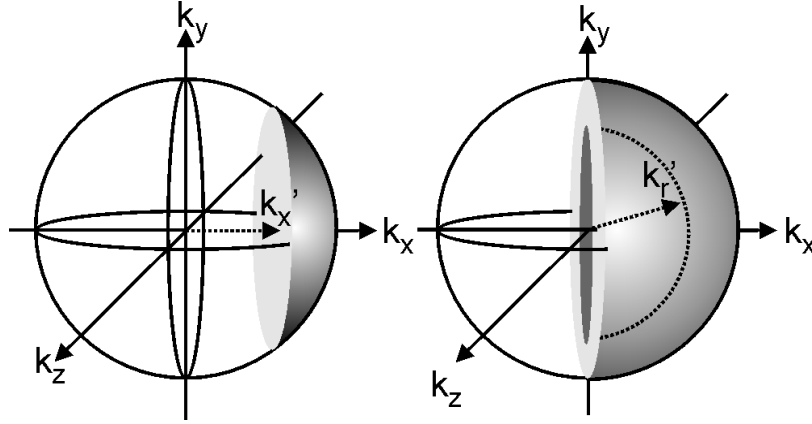


Figure 8.1: Left: The shaded area indicates which electrons in the Fermi sphere are transmitted when only the momentum in the direction of transport is constrained to be greater than a particular value k'_x . Right: The shaded area indicates electrons which may participate in transport when momentum is constrained to have a minimum value in all three dimensions.

The results of Chapter 7 of this thesis show that both of these characteristics are detrimental to the efficiency of thermionic devices. The reason is simply because the electrons which do work or remove heat most efficiently, are those with energies just above E_0 , for a power generator, and those just below E_0 , for a refrigerator.

8.1.1 Efficient Thermionic Power Generation

The ideal thermionic power generator would use an energy filter which constrained the momentum of transmitted electrons in three dimensions (a quasi 0D system such as a quantum dot) rather than an energy barrier in the direction of transport, for two reasons. Firstly, because the efficiency of the device can approach the Carnot limit in principle if only electrons at E_0 are transmitted (and if there is no phonon heat leaks). Secondly, because even if a wide resonance is used to transfer a finite range of electron energies between reservoirs, constraining the momentum of the electrons in all three dimen-

sions means that the spectrum of the transmitted electrons is not dominated by high energy electrons, which do the same amount of work as lower energy electrons (eV per electron) but do it much less efficiently, removing more heat from the hot reservoir. For comparison, the electrons which are transmitted through a device in which momentum is constrained in three dimensions are represented by the shaded shell in the right Fermi sphere in Figure 8.1, and result in quite a different energy spectrum from that of a conventional device, shown on the left. Note that throughout this thesis, a 1D-0D-1D system has been analysed. The electrons transmitted in this case correspond to a cube on the x-axis in the Fermi sphere on the right. A discussion of transport through 3D-0D-03D systems is provided in Appendix H.

8.1.2 Efficient Thermionic Refrigeration

The ideal thermionic refrigerator would also utilise an energy filter which constrained the momentum of transmitted electrons in three dimensions, which again means that the efficiency is limited only by the Carnot limit in principle (if there are no phonon heat leaks). In the case of a refrigerator the use of a finite ‘window’ of transmission is even more important than for a power generator, for in a refrigerator there is only a finite range of electrons with energies which contribute positively to the power. If a simple barrier is used, then the efficiency is *always* limited to below the Carnot value due to the ‘back-current’ of electrons with energies greater than E_0 , which reduce both the power and the efficiency.

8.2 Relationship with Thermoelectric Theory

One of the most surprising results of Chapter 7, is that Equation 7.33, describing the efficiency of the ESE heat engine in the maximum power regime, has the same functional dependence on the temperatures of the reservoirs as that of thermoelectric power generators. The reason this is surprising is that the equations used to describe electron transport in this thesis are only ap-

plicable for ballistic transport, whereas electron transport in thermoelectric devices is diffusive. The maximum efficiency of a thermoelectric heat engine is given by [69]

$$\eta_H^{TE} = (1 - \tau) \left(\frac{M - 1}{M + \tau} \right) \quad (8.1)$$

where $M = \sqrt{1 + Z}$, and $Z = \sigma S^2 T_{av} / \kappa$ is the thermoelectric figure of merit of the material, where σ is the conductivity, $S \equiv dV/dT$ the Seebeck coefficient, $T_{av} = 0.5 (T_H + T_C)$ the average temperature of the junction, and $\kappa = \kappa_{el} + \kappa_{ph}$ the thermal conductivity of the material which is the sum of the thermal conductivity due to electron conduction and the thermal conductivity due to the propagation of phonons through the lattice.

The efficiency of the ESE heat engine in the maximum power regime is given by Equation 7.39, repeated here for the convenience of the reader.

$$\eta_{HE}^{\max}(\gamma_0) = (1 - \tau) \left(\frac{A(\gamma_0)}{1 + A(\gamma_0) + \tau} \right) \quad (8.2)$$

where

$$A(\gamma_0) = \frac{-\gamma_0 \ln \left(\frac{\exp(\gamma_0)}{1 + \exp(\gamma_0)} \right)}{\frac{1}{2} \left[\ln \left(\frac{\exp(\gamma_0)}{1 + \exp(\gamma_0)} \right) \right]^2 + \text{di log} \left(\frac{\exp(\gamma_0)}{1 + \exp(\gamma_0)} \right)} \quad (8.3)$$

and where $\gamma_0 \equiv (\varepsilon_C - \varepsilon_H) / (kT_H - kT_C)$.

Equations 8.1 and 8.2 both have the same explicit dependence on the ratio of the potential gradient to the thermal gradient. The dependence of the efficiency of the ESE heat engine on the electrical conductivity κ_{el} is implicit in Equation 8.2, and there is no dependence on thermal conduction due to phonons, as this has not been considered in this thesis. The form derived for the efficiency of the ESE refrigerator in the maximum power regime does not bear a likewise similarity to the expression for the efficiency of a thermionic refrigerator. This may be expected, as the ESE refrigerator only allows transport between the Fermi energy of the cold reservoir and E_0 , whereas a thermionic refrigerator allows transport at all energies above the barrier provided by the higher bandgap material in the p-n junction.

This is not the first time that a similarity between devices operated in the ballistic and diffusive regime of transport has been noticed, and the

physics behind it is not, as yet, well understood. Mahan et al., in their paper on multilayer thermionic refrigeration [74], noted that in the limit that the difference in temperature and electrical potential between reservoirs becomes small, thermionic equations become identical with thermoelectric equations if appropriate substitutions are made. Nolas, Sharp and Goldsmid, in their recent (2001) book "Thermoelectrics" [71] observe that this

"...suggests that, although solid-state thermionic converters are distinctly different from thermoelectric refrigerators and generators, there may be a close connection between them."

Vining and Mahan [80] have shown using equations for thermionics equivalent to those used for determining the figure of merit Z of thermoelectric materials, that any given material will perform better in thermoelectric mode than thermionic mode. It will be interesting to determine whether this conclusion still holds true if the improvements to thermionic refrigerators and power generators suggested in this thesis are implemented.

Appendix A

Fabrication Details

This appendix lists the steps followed in fabricating the devices, which are fairly standard procedures for producing Point Contacts at the Ørsted Lab:

Wafer: mobility $\sim 630000 \text{ cm}^2 \text{ Vs}^{-1}$ @ 10K; Electron density $\sim 1.4 \times 10^{15} \text{ m}^{-2}$.

1. Cleave the wafer.
2. Wash in Acetone, then Methanol, then Isopropanol, Blow dry with N_2 gas.
3. Spin resist (AZ4511) for 40 seconds at 4000 rev/min. Bake for 45 sec at 115°C .
4. Create mesas by UV lithography, putting wafer in contact with plates and exposing the resist for 21 seconds using Karl Süss MJB3 mask-aligner.
5. Develop the mesas, using AZ400K developer (0.25% solution of KOH in water) for 60 seconds, then rinse with De-ionised millipore water. Blow dry with N_2 gas.
6. Ash for 30s (O_2 plasma)
7. Etch using a solution of $\text{H}_3\text{PO}_4(85\%):\text{H}_2\text{O}_2(30%):\text{H}_2\text{O}$ in a ratio of 1:1:38. This etches the exposed regions of the wafer at a rate of

100nm/min. Then rinse with deionised millipore water to stop the etch. Clean with Acetone to remove unexposed resist, then with methanol and isopropanol. Dry with N₂.

8. Repeat steps 1-6 (using AZ4521 resist) to create the contacts but do not clean the resist off in the last step.
9. Deoxidise for 30s sec in NH₃(25%):H₂O in ratio 1:15.
10. Metallisation of the ohmic contacts. Use Au 400 Å, Ge 600 Å, Ni 270 Å, then Au 2000 Å. Place into Acetone for a few minutes to get lift-off. Wash with Methanol and Isopropanol. Blow dry.
11. Alloy the ohmic contacts in the alloying machine at temp 420 °C.
12. Repeat for 'metal' mask, without etching and using Cr 100 Å and Au 1500 Å to make gate contacts. These are not alloyed.

To do the E-beam lithography:

1. Clean sample in hot acetone, methanol and isopropanol (5min each @ 50 °C)
2. Ash sample for 20 sec.
3. Deoxidise 5-10 min in 18% HCl:H₂O. Rinse in Millipore water.
4. Pre-bake for 5 min at 185 °C.
5. Spin 2% PMMA at 6000 rpm for 60 sec
6. Hard Bake resist at 185 °C for 5 minutes
7. Expose sample in the SEM
8. Develop 60 sec in MIBK:2-propanol (1:3)
9. Post-bake at 115 °C for 5-10min

10. Ash sample for 6 sec
11. Shallow etch in $\text{H}_3\text{PO}_4:\text{H}_2\text{O}_2:\text{H}_2\text{O}$ (1:1:38) $\sim 100\text{nm}/\text{min}$

The parameters used for the SEM exposure were as follows:

Line Dose: $5\mu\text{C}/\text{cm}$

Beam current: 41nA

Step size: 5nm

Dose time: 1.585ms

Resist sensitivity parameter: 130

Total exposure time for asymmetric pattern: 19 sec.

The shape of the devices was given by:

Asymmetric specs: $y=32.5 \pm [0.1/\sqrt{x-32.01} + 0.125]$ for $x = 32.01$ to 33mm

Symmetric Specs: $y=32.5 \pm [1.15*(x-32.5)^2 + 0.225]$ for $x = 30.5$ to 34.5mm

(center of working area: $x=32.5\text{mm}$, $y=32.5\text{mm}$)

After exposure on the SEM the device was etched for 20-25sec, that is, about 40nm , which was just sufficient to remove the donor layer.

Appendix B

Details of the Data Analysis

The parameters measured directly in the experiment were

1. The voltage over the 1K resistor
2. The voltage over the device
3. The voltage over the Lakeshore RuO_x resistor

These measurements were converted to the current through the device, the differential conductance of the device and the temperature respectively as follows.

If the device was asymmetrically gated, that is, the voltage divider in the top right of figure 3.4 is *not* present then the differential current through the device is given by

$$I_{dev} = V_{1K}/1000 \quad (\text{B.1})$$

If the device is symmetrically gated, then some of the current through the 1K resistor goes through the device and some through the voltage divider (resistance = 2×100 kΩ), and then the current through the circuit is given by

$$dI_{dev}/dV_{sd} = V_{1K}/1000 - V_{dev}/200000 \quad (\text{B.2})$$

The voltage over the device may be used in this expression as is must be equal to that dropped over the voltage divider as they are in parallel.

The differential conductance is simply given by

$$g_{dev} = I_{dev}/V_{dev} \quad (\text{B.3})$$

where both I_{dev} and V_{dev} are differential quantities (changes in the current and voltage over the device with respect to the AC component of the source-drain voltage).

The DC source-drain voltage which falls over the device (not including its ohmic contacts) may be determined if the resistance of the ohmic contacts and the rest of the measurement circuit is known.

$$V_{sd}^{device} = \frac{V_{sd}^{circuit}}{700} \frac{1/G_{dev}^{diff}}{1000 + R_{ohmics} + 1/G_{dev}^{diff}} \quad (\text{B.4})$$

The temperature of the device was determined from the resistance of the Lakeshore RuO_x sensor using a Matlab program which was written to implement the 10 parameter fit provided with the sensor for interpolation between the calibrated values. Different fit parameters were used in the temperature ranges 0.23K-1K and 1K to 5K.

Appendix C

Dependence of τ on the barrier shape

Here the $\Delta\tau(E)$ functions of three asymmetric potential barriers are calculated for the purpose of ascertaining how sensitive the transmission probability is to changes in the degree of asymmetry or the width of a barrier. Potential 'A' (shown in Figure C.1 under a source-drain voltage of $\pm V_{sd} = 4\text{meV}$) was made from sinusoids and is only slightly asymmetric. Potential 'B' is very asymmetric, and was produced by very slightly smoothing a sawtooth shape based on the lithography of device D3 (shown in figure C.2). Potential 'C' was produced by smoothing a sawtooth shape based on the lithography of the devices in [26] (results for this potential are shown in [26]). Finally potential 'D' is simply potential C stretched so that its length is the same as the lithographic length of D3 (shown in 3.2). Potential D was the potential chosen for in depth study in numerical modelling in the experimental chapters of this thesis.

The $\Delta\tau$ curves for all four potentials are shown in Figure C.4. The $\Delta\tau$ curve of potential B did not exhibit any sign changes, indicating that the increase in width of the potential under negative bias voltage was sufficiently great that the transmission probability for this polarity was smaller than that for positive voltage for all energies, below and above the barrier height

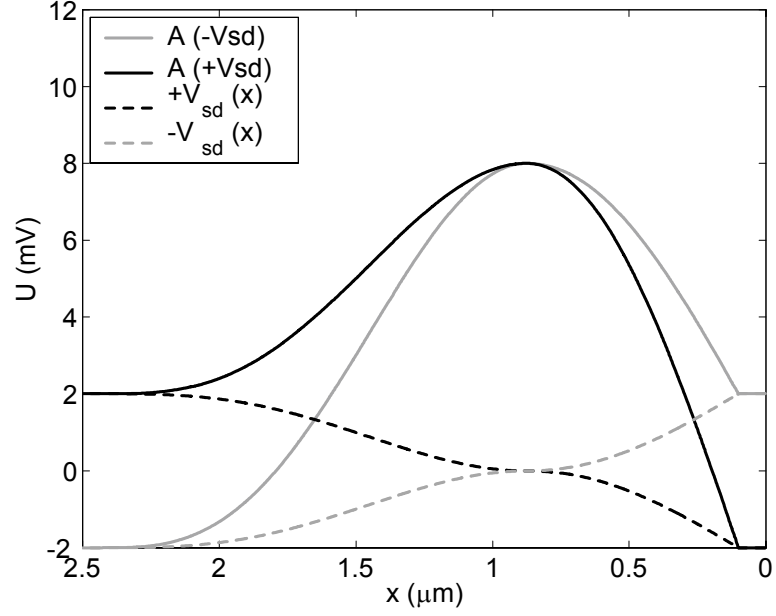


Figure C.1: Potential A is only slightly asymmetric and was created from sinusoids. It is shown for $V_{sd} = \pm 4\text{mV}$. Due to the fact that the potential is only slightly asymmetric, its shape is very similar for source-drain voltages of opposite sign. This in turn means that the transmission probabilities of electrons through it for positive and negative source-drain voltages will be very similar. The manner in which V_{sd} was distributed over the barrier is also shown. This voltage dropped over a section of the potential was chosen to be proportional to the slope of the barrier in that section.

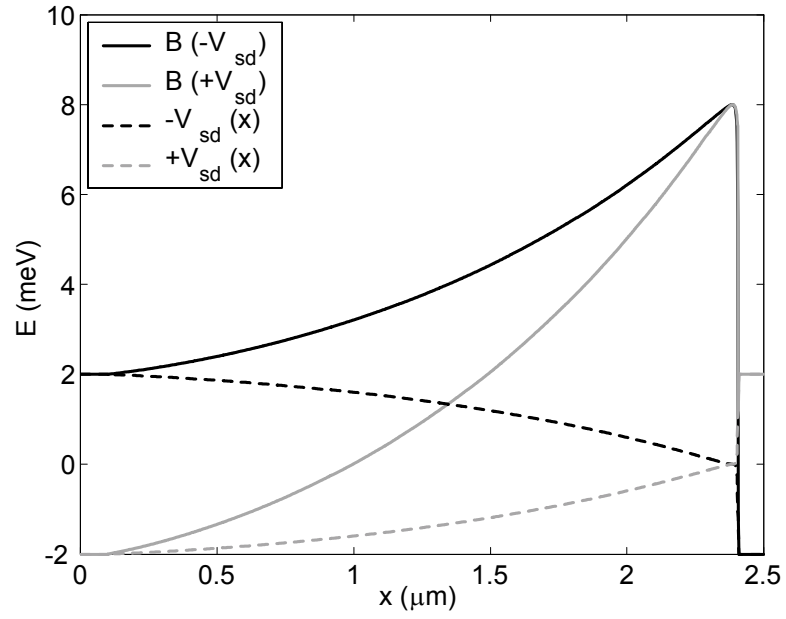


Figure C.2: Potential B was made by very slightly smoothing a sawtooth barrier. It is strongly asymmetric, and this fact is reflected in the very distinct difference in its shape under positive and negative source-drain voltages. Here $V_{sd} = \pm 4\text{mV}$ and again the voltage is distributed across the barrier in proportion to its local gradient.

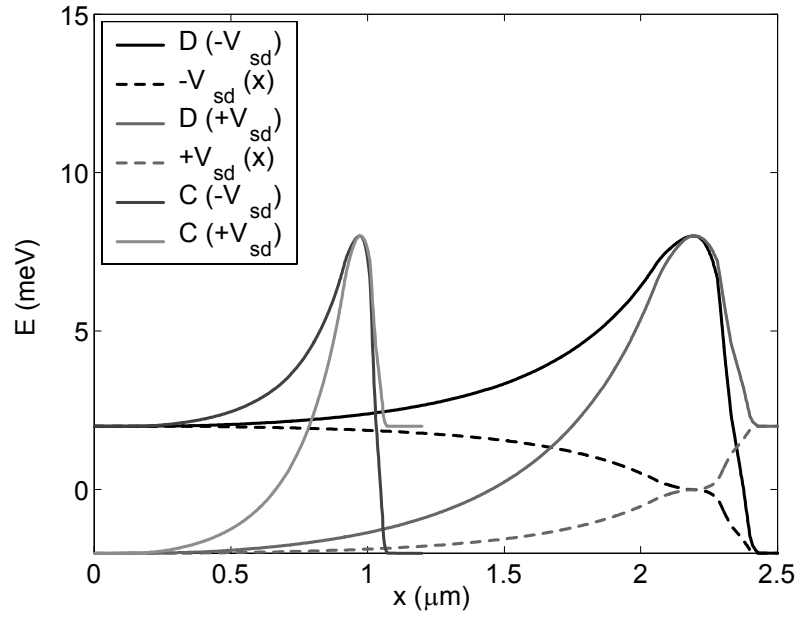


Figure C.3: Barrier C (short) is the barrier which was used in the numerical calculations in [26]. Barrier D (longer) is a stretched version of barrier C. These barriers both have an intermediate amount of asymmetry, with the difference between them being the width of the barrier near the top. An increased width affects the transmission probability as tunnelling is less likely.

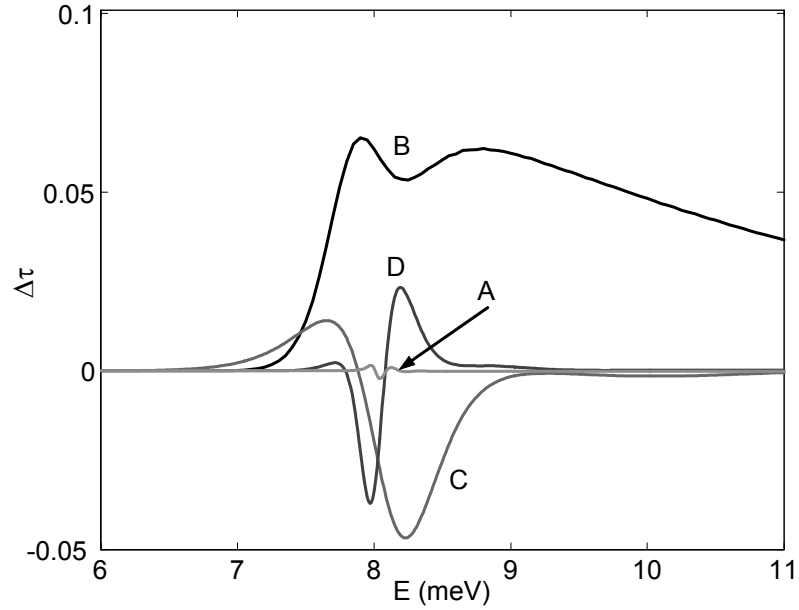


Figure C.4: The $\Delta\tau$ curves of the potentials A to D.

(to $> 50\text{meV}$). The $\Delta\tau$ curve for potential A was relatively insignificant, indicating that the potential experienced by the electrons in the experiment was more asymmetric than this. It is likely that the asymmetry of the experimental potential lay somewhere between potential C and potential B.

In general, if a positive bias, $(+V_{sd})$, is applied to an asymmetric potential (with the steep side on the right) the potential maxima becomes narrower and sharper. If instead a negative bias, $(-V_{sd})$, is applied it becomes wider and smoother (see Figures C.1, C.2 and C.3). This does not occur for symmetric potentials, where the shape is the same under both bias voltage polarities. As the transmission probability in the quantum regime depends not only on the height of a barrier (which remains constant here), but also on the exact shape of a barrier, the transmission probability of the barrier under positive and negative bias voltages is not the same. This difference, $\Delta\tau$, is shown as a function of energy in figure C.4. With reference to figures C.1, C.2, C.3 and C.4, some *qualitative* observations may be made about the effect of the

shape of the potential upon $\Delta\tau$:

1. The narrower the potential, the smaller the energy at which tunnelling begins.
2. Sharp maximas tend to increase wave-reflection at energies close to the barrier height and cause oscillations in the transmission probability at high energies.
3. The wider the potential, the larger the wave reflection at energies much higher than the barrier height.

With reference to figure C.4, it can be seen that the $\Delta\tau$ curves of all the potentials exhibit:

1. An initial local maximum.
2. A local minimum near the barrier height of 8mV.
3. Another local maximum at energies higher than 8mV.

The relative magnitudes of these positive and negative areas depend upon the details of the potential shape, but they are present in all four potentials examined. It follows that the general predictions of the model may be expected to be insensitive to the exact shape of the asymmetric potential that was ultimately chosen for further analysis (potential D). This is very important, given the difficulty of ascertaining the exact confinement potential experienced by the electrons in the experiment.

Appendix D

Numerical Calculation of τ

The one-dimensional, time-independent Schrödinger equation for a free electrons is:

$$\frac{d^2\psi(x)}{dx^2} = k(x) \psi(x) \quad (\text{D.1})$$

where

$$k(x) = \frac{\sqrt{2m^*[E - V(x)]}}{\hbar} \quad (\text{D.2})$$

and $\psi(x)$ is the electron wave-function, $V(x)$ the potential, m^* the effective mass of the electron ($0.067m_e$ in GaAs) and E the energy of the electron.

This is a linear, second-order differential equation and may be solved numerically by dividing the distance across the barrier from $x = 0$ to $x = L$ into segments of length δx , and using Numerov's method [65] for solving second order differential equations with no first-order derivative term to calculate the value of the wavefunction at segment n as:

$$\left[1 - \frac{1}{12}(\delta x)^2 k(n)\right] \psi(n) = \left[2 + \frac{5}{6}(\delta x)^2 k(n-1)\right] \psi(n-1) \quad (\text{D.3})$$

$$- \left[1 - \frac{1}{12}(\delta x)^2 k(n-2)\right] \psi(n-2) \quad (\text{D.4})$$

Two initial conditions are needed. It is known that, far from the barrier on the right, the wavefunction of electrons transmitted across the barrier is well-described by a plane wave (assuming the potential is constant far from the barrier). Using this information, the wavefunction on the far side

of the barrier is calculated first (conceptually, the electron is propagated 'backwards' over the barrier) by using the substitution $z = L - x$. The initial conditions are taken at $z = 0$ and $z = \delta x$ to be $\psi(0) = 1$ and $\psi(\delta x) = \exp[-ik(\delta x)\delta x]$ where

$$k(\delta x) = \frac{\sqrt{2m^*[E - V(\delta x)]}}{\hbar} \quad (\text{D.5})$$

To find the transmission probability from the wavefunction, it is noted that far from the barrier on left (the direction of incidence) the wavefunction of the electron can be assumed to be a combination of right- and left-going plane waves, and can be written as

$$\psi(x) = A \exp[-ik(x)x] + B \exp[+ik(x)x] \quad (\text{D.6})$$

where A and B are amplitudes of the incident and reflected waves respectively. To obtain an expression for A , the equations for the wavefunction at $x = 0$ and $x = \delta x$ are solved simultaneously to give:

$$A = \frac{\psi(\delta x) - \psi(0) \exp[ik(0)\delta x]}{\exp[-ik(0)\delta x] - \exp[ik(0)\delta x]} \quad (\text{D.7})$$

Assuming that half of the source-drain voltage V_{sd} is applied to each side of the barrier ($+eV_{sd}/2$ to the left and $-eV_{sd}/2$ to the right side), and defining C as the amplitude of the transmitted wave, the transmission probability may then be found as:

$$T(\varepsilon, V_{sd}) = \frac{k(0)}{k(L)} \frac{C^* C}{A^* A} = \sqrt{\frac{\varepsilon - eV_{sd}/2}{\varepsilon + eV_{sd}/2}} \frac{1}{A^* A} \quad (\text{D.8})$$

Appendix E

Saddle-point Potential Model

The saddle-point potential model assumes that the two-dimensional potential of the point contact close to the narrowest point can be described by an analytic 'saddle' shape (for zero magnetic field):

$$U(x, y) = U_0(V_{sd}) + 0.5m^*\omega_y^2y^2 - 0.5m^*\omega_x^2x^2 \quad (\text{E.1})$$

where m^* is the effective mass of an electron, ω_x and ω_y are parameters describing the shape of the saddle and x and y are the coordinates along the length and width of the point contact respectively. The model retains only the linear and quadratic terms of the Taylor expansion of the electrostatic potential near the centre of the point contact, and assumes that the shape of the potential doesn't change with the source drain voltage V_{sd} , but rather that the electrostatic potential energy of the saddle-point is a function of V_{sd} .

Appendix F

Fermi Distribution Proof

As referred to in §7.1.2, in this appendix it will be shown that the heat flux into the hot and cold reservoirs is the same for positive and negative source drain voltage when the transmission probability is a resonance which is located at $\varepsilon_C + \phi$ for $+V_{sd}$, and at $\varepsilon_C - \phi$ for $-V_{sd}$. That is, $\dot{Q}_C(+V_{sd}) = \dot{Q}_C(-V_{sd})$ and $\dot{Q}_H(+V_{sd}) = \dot{Q}_H(-V_{sd})$.

For simplicity it will be assumed that the resonance is sufficiently narrow that the integrals in Equations 6.3 and 6.4 may be evaluated at the energy of the resonance. The heat flux into the cold and hot reservoirs is then

$$\dot{Q}_C(\pm V_{sd}) = \pm \frac{2}{h} \phi \left\{ \frac{1}{\exp \left[\frac{\pm \phi \pm e V_{sd}}{k T_H} \right] + 1} - \frac{1}{\exp \left[\frac{\pm \phi}{k T_C} \right] + 1} \right\} \delta E \quad (\text{F.1})$$

$$\dot{Q}_R(\pm V_{sd}) = \pm \frac{2}{h} [\phi + e V_{sd}/2] \left\{ \frac{1}{\exp \left[\frac{\pm \phi \pm e V_{sd}}{k T_H} \right] + 1} - \frac{1}{\exp \left[\frac{\pm \phi}{k T_C} \right] + 1} \right\} \delta E \quad (\text{F.2})$$

Now

$$\dot{Q}_C(-V_{sd}) = -\frac{2}{h}\phi \left\{ \frac{1}{\exp\left[\frac{-\phi-eV_{sd}}{kT_H}\right] + 1} - \frac{1}{\exp\left[\frac{-\phi}{kT_C}\right] + 1} \right\} \delta E \quad (\text{F.3})$$

$$= -\frac{2}{h}\phi \left\{ \frac{\exp\left[-\frac{-\phi-eV_{sd}}{kT_H}\right]}{1 + \exp\left[-\frac{-\phi-eV_{sd}}{kT_H}\right]} - \frac{\exp\left[-\frac{-\phi}{kT_C}\right]}{1 + \exp\left[-\frac{-\phi}{kT_C}\right]} \right\} \delta E \quad (\text{F.4})$$

$$= -\frac{2}{h}\phi \left\{ \frac{\frac{\exp\left[\frac{+\phi+eV_{sd}}{kT_H}\right]}{\exp\left[\frac{+\phi+eV_{sd}}{kT_H}\right] + 1} - 1}{-\frac{\exp\left[\frac{+\phi}{kT_C}\right]}{\exp\left[\frac{+\phi}{kT_C}\right] + 1} + 1} \right\} \delta E \quad (\text{F.5})$$

$$= -\frac{2}{h}\phi \left\{ \frac{\frac{\exp\left[\frac{+\phi+eV_{sd}}{kT_H}\right] - \exp\left[\frac{+\phi+eV_{sd}}{kT_H}\right] - 1}{\exp\left[\frac{+\phi}{kT_H}\right] + 1}}{-\frac{\exp\left[\frac{+\phi}{kT_C}\right] - \exp\left[\frac{+\phi}{kT_C}\right] - 1}{\exp\left[\frac{+\phi}{kT_C}\right] + 1}} \right\} \delta E \quad (\text{F.6})$$

$$= -\frac{2}{h}\phi \left\{ \frac{-1}{\exp\left[\frac{+\phi+eV_{sd}}{kT_H}\right] + 1} - \frac{-1}{\exp\left[\frac{+\phi}{kT_C}\right] + 1} \right\} \delta E \quad (\text{F.7})$$

$$= \frac{2}{h}\phi \left\{ \frac{1}{\exp\left[\frac{+\phi+eV_{sd}}{kT_H}\right] + 1} - \frac{1}{\exp\left[\frac{+\phi}{kT_C}\right] + 1} \right\} \delta E \quad (\text{F.8})$$

$$= \dot{Q}_C(+V_{sd}) \quad (\text{F.9})$$

It can similarly be shown that $\dot{Q}_H(+V_{sd}) = \dot{Q}_H(-V_{sd})$.

Appendix G

Derivation of $\delta S/\delta N$

The entropy of a free electron gas in a conductor is given by [67]

$$S = Nk \frac{\pi^2}{2} \left(\frac{kT}{\varepsilon_F} \right) \left[1 - \frac{\pi^2}{10} \left(\frac{kT}{\varepsilon_F} \right)^2 + \dots \right] \approx Nk \frac{\pi^2}{2} \frac{kT}{\varepsilon_F} \quad (\text{G.1})$$

Here N is the total number of electrons, T is the temperature of the gas, and the Fermi energy ε_F is given by

$$\varepsilon_F = \frac{h^2}{8m} \left(\frac{3N}{\pi V} \right)^{2/3} \quad (\text{G.2})$$

If we add a small number of electrons to the reservoir, δN , then the corresponding change in the entropy of the gas is given by

$$\delta S = \frac{k^2 \pi^2}{6} \frac{T}{\varepsilon_F} \delta N + \frac{k^2 \pi^2}{2 \varepsilon_F} \frac{\delta T}{\delta N} \delta N \quad (\text{G.3})$$

$\delta \varepsilon_F / \delta N$ is given by the partial derivative of Equation G.2 with respect to N

$$\frac{\delta \varepsilon_F}{\delta N} = \frac{2}{3} \frac{\pi^2}{2m} \left(\frac{3N}{\pi V} \right)^{2/3} N^{-1} = \frac{2}{3} \frac{\varepsilon_F}{N} \quad (\text{G.4})$$

In order to find an expression for $\delta T / \delta N$ we take the partial derivative of the total energy, U , of the electron gas with respect to N , and note that if the electrons added all have energy E , then $\delta U / \delta N$ must be equal to E . From [67],

$$U = \frac{3}{5} N \varepsilon_F \left[1 + \frac{5\pi^2}{12} \left(\frac{kT}{\varepsilon_F} \right) - \dots \right]. \quad (\text{G.5})$$

Then

$$\frac{\delta U}{\delta N} = \varepsilon_F + \frac{\pi^2 k^2 N T}{2\varepsilon_F} \frac{\delta T}{\delta N} = E \quad (\text{G.6})$$

and

$$\delta T = -\frac{2\varepsilon_F (E - \varepsilon_F)}{\pi^2 k^2 T} \frac{\delta N}{N}. \quad (\text{G.7})$$

Substituting Equations G.4 and G.7 into Equation G.3 we obtain

$$\delta S = \frac{k^2 \pi^2}{6} \frac{T}{\varepsilon_F} \delta N + \frac{E - \varepsilon_F}{T} \delta N \quad (\text{G.8})$$

We earlier assumed that kT was small compared to ε_F , when the cubic term in Equation 7.1 was disregarded. We may then also disregard the first term in Equation G.8 to finally obtain the usual expression for the change in entropy of an electron gas upon the addition of δN electrons.

$$\delta S = \frac{E - \varepsilon_F}{T} \delta N \quad (\text{G.9})$$

This equation is only valid where $\delta T \ll T$, and where $kT \ll \varepsilon_F$.

Appendix H

2D-0D-2D and 3D-0D-3D transport

In §7.2.1 it was demonstrated that the second law of thermodynamics places a restriction in the form that the energy-resolved current between two electron reservoirs may take. As shown by Equation 7.4, the second law specifies that the current $\dot{N}(E)$ between two electron reservoirs over a small range of energies δE about the energy E , must be proportional to the difference in the occupation of states in the reservoirs at this energy E . In §7.2.2 it was confirmed that the Landauer equation, used to describe transport between one-dimensional reservoirs, is consistent with this requirement. In this section, it will be shown that the current between two and three dimensional reservoirs via an energy filter, that is 3D-0D-3D or 2D-0D-2D transport situations, yields an expression which also changes sign at the energy required by Equation 7.4 when derived under the same assumptions as were used in §7.2.2. In this case it is assumed that all modes in the 3D lead with the ‘right’ energy couple perfectly with the state in the quantum dot energy filter. In reality, the coupling of states in the 3D leads will not be complete, and a discussion of recent work using Greens formalism to calculate the 3D-0D-3D current is given at the end. The analysis presented here does however give an upper limit on the current through a quantum dot via 3D

leads by assuming perfect coupling. It should be made clear that where a higher dimensional reservoir is adiabatically merged into a one-dimensional region, through which transport then proceeds ballistically, as is the case for the QPC devices discussed in the first chapters of this thesis, then the current is well-described by the one-dimensional Landauer formalism already introduced.

The strategy used in this section is similar to that used in deriving the expression for the current between one-dimensional reservoirs in §7.2.2. The assumption used is that current is given, as a function of wave-vector, by the product of number of states (at a particular wave-number), the occupation of those states, and velocity in the direction of transport (assumed to be the z-direction). Per 'energy filter' between the reservoirs, the current of electrons over a small momentum range δk_r from the cold to the hot reservoir (please refer to figure 7.1 for an illustration), $\dot{N}(E)_{C \rightarrow H}$, is given in spherical k-space coordinates by

$$\dot{N}_{C \rightarrow H}^{3D}(k_r) = \int_0^\pi \int_{-\pi/2}^{\pi/2} \left[\frac{2k_r^2 \sin k_\phi dk_\theta dk_\phi}{(2\pi)^3} \right] \left[\frac{\hbar}{m} k_r \sin k_\phi \cos k_\theta \right] f_C(E) \delta k_r \quad (\text{H.1})$$

$$\dot{N}_{C \rightarrow H}^{2D}(k_r) = \int_{-\pi/2}^{\pi/2} \left[\frac{2k_r dk_\theta}{(2\pi)^2} \right] \left[\frac{\hbar}{m} k_r \cos k_\theta \right] f_C(E) \delta k_r \quad (\text{H.2})$$

The terms in $\dot{N}(E)_{C \rightarrow H}$ are, respectively, the product of a volume element in k-space and density of states, the occupation function, $f_C(E)$, and the speed of electrons with velocity $\hbar k_r/m$ in the direction of transport, which is assumed to be the z-direction, in three and two-dimensions. We can now integrate over k_θ and k_ϕ (where appropriate) and we then obtain

$$\dot{N}_{C \rightarrow H}^{3D}(k_r) = \frac{\hbar}{4m\pi^2} k_r^3 f_C \delta k_r \quad (\text{H.3})$$

$$\dot{N}_{C \rightarrow H}^{2D}(k_r) = \frac{\hbar}{m\pi^2} k_r^2 f_C \delta k_r \quad (\text{H.4})$$

We change variables to energy, $E = \hbar^2 k_r^2 / 2m$. Then

$$\dot{N}_{C \rightarrow H}^{3D}(E) = \frac{2mE}{4\hbar^3 \pi^2} f_C \delta E \quad (\text{H.5})$$

$$\dot{N}_{C \rightarrow H}^{2D}(E) = \frac{\sqrt{2mE}}{\hbar^2 \pi^2} f_C \delta E \quad (\text{H.6})$$

This then is the flux of electrons travelling from the cold to the hot reservoir. The hot to cold-going flux is obtained similarly as

$$\dot{N}_{C \rightarrow H}^{3D}(E) = -\frac{2mE}{4\hbar^3 \pi^2} f_H \delta E \quad (\text{H.7})$$

$$\dot{N}_{C \rightarrow H}^{2D}(E) = -\frac{\sqrt{2mE}}{\hbar^2 \pi^2} f_H \delta E \quad (\text{H.8})$$

This gives the total flux as

$$\dot{N}^{3D}(E) = \frac{2mE}{4\hbar^3 \pi^2} [f_C - f_H] \delta E \quad (\text{H.9})$$

$$\dot{N}^{2D}(E) = \frac{\sqrt{2mE}}{\hbar^2 \pi^2} [f_C - f_H] \delta E \quad (\text{H.10})$$

Substituting Equations H.9 and H.10 into Equation 7.4 we can obtain expressions for the total entropy flux of the composite system consisting of the hot and cold reservoirs as

$$\dot{S}_{tot}^{3D} = \frac{2mE}{4\hbar^3 \pi^2} \left[\frac{E - \varepsilon_H}{T_H} - \frac{E - \varepsilon_C}{T_C} \right] \left[\frac{1}{1 + \exp\left(\frac{E - \varepsilon_C}{kT_C}\right)} - \frac{1}{1 + \exp\left(\frac{E - \varepsilon_H}{kT_H}\right)} \right] \delta E \quad (\text{H.11})$$

$$\dot{S}_{tot}^{2D} = \frac{\sqrt{2mE}}{\hbar^2 \pi^2} \left[\frac{E - \varepsilon_H}{T_H} - \frac{E - \varepsilon_C}{T_C} \right] \left[\frac{1}{1 + \exp\left(\frac{E - \varepsilon_C}{kT_C}\right)} - \frac{1}{1 + \exp\left(\frac{E - \varepsilon_H}{kT_H}\right)} \right] \delta E \quad (\text{H.12})$$

Equations H.11 and H.12 give an indication of the current expected in a 3D-0D-3D or 2D-0D-2D system, and are consistent with the thermodynamical requirement expressed by Equation 7.4. However, the contribution from a state in the leads will, in general, be k dependent, and a more sophisticated approach is really needed to describe 3D-0D-3D current. Boero et al. [121, 122] have calculated the current through a quantum dot for the situation where the emitter and collector contacts are three-dimensional using the Landauer formula derived for interacting systems by Meir and Wingreen [123]

$$I = -\frac{2e}{h} \int dE [f_L(E) - f_R(E)] \text{Im} \left(\text{Tr} \left(\Gamma(E) G^R(E) \right) \right) \quad (\text{H.13})$$

where I is the current flowing through the system, f_L and f_R are the Fermi-Dirac distribution functions for the left and right contacts, G^R is the quantum-dot retarded Green's function. Γ represents the coupling between the dot states and the contacts

$$\Gamma = \frac{\Gamma^L \Gamma^R}{\Gamma^L + \Gamma^R} \quad (\text{H.14})$$

where

$$\Gamma_{a,b}^L = \sum_n \rho_n^L(E) V_{a,n}^{*L} V_{n,b}^L \quad (\text{H.15})$$

where $\rho_n(E)$ is the density of states in the contact in the n th sub-band, and $V_{a,n}^{*L}$ and $V_{n,b}^L$ are the matrix elements between the dot states and the contacts. As many states in the contacts can couple to a particular state in the dot, the calculation of Γ is more complicated for three-dimensional contacts than for one-dimensional contacts, where the lateral state of an electron is not changed during tunnelling. Note is that Equation H.13 contains a multiplicative term consisting of the difference in the Fermi distributions in the emitter and collector contacts, as required by Equation 7.4.

Appendix I

Maximum Power Integrals

Here the analytic expressions for the power and efficiency of the ESE heat engine and refrigerator operating in the maximum power regime will be derived.

The heat change in the cold reservoir is given by

$$\dot{Q}_C = -\frac{2}{h} \int_a^b (E - \varepsilon_C) \left(\left[1 + \exp \left(\frac{E - \varepsilon_C}{kT_C} \right) \right]^{-1} - \left[1 + \exp \left(\frac{E - \varepsilon_H}{kT_H} \right) \right]^{-1} \right) dE \quad (\text{I.1})$$

$$\dot{Q}_H = \frac{2}{h} \int_a^b (E - \varepsilon_H) \left(\left[1 + \exp \left(\frac{E - \varepsilon_C}{kT_C} \right) \right]^{-1} - \left[1 + \exp \left(\frac{E - \varepsilon_H}{kT_H} \right) \right]^{-1} \right) dE \quad (\text{I.2})$$

The power of the device when it is behaving as a heat engine is

$$P_{HE} = - \left(\dot{Q}_C + \dot{Q}_H \right) \quad (\text{I.3})$$

and the efficiency given by

$$\eta_{HE} = \frac{- \left(\dot{Q}_C + \dot{Q}_H \right)}{-\dot{Q}_H} \quad (\text{I.4})$$

The power of the device when it is behaving as a refrigerator is given by

$$P_R = -\dot{Q}_C \quad (\text{I.5})$$

and the efficiency given by

$$\eta_R = \frac{-\dot{Q}_C}{\dot{Q}_C + \dot{Q}_H} \quad (\text{I.6})$$

The integrals I.1 and I.2 must each be done between the limits $E_0 = (\varepsilon_C T_H - \varepsilon_H T_C)/(T_H - T_C)$ and ∞ , and ε_C and E_0 to calculate the efficiency at maximum power for the device as a heat engine (η_{HE}^{\max}) and as a refrigerator (η_R^{\max}).

Let

$$I_1 = +\frac{2}{h} \int_a^b \frac{(E - \varepsilon_H)}{1 + \exp\left(\frac{E - \varepsilon_C}{kT_C}\right)} dE \quad (\text{I.7})$$

$$I_2 = -\frac{2}{h} \int_a^b \frac{(E - \varepsilon_H)}{1 + \exp\left(\frac{E - \varepsilon_H}{kT_H}\right)} dE \quad (\text{I.8})$$

$$I_3 = -\frac{2}{h} \int_a^b \frac{(E - \varepsilon_C)}{1 + \exp\left(\frac{E - \varepsilon_C}{kT_C}\right)} dE \quad (\text{I.9})$$

$$I_4 = +\frac{2}{h} \int_a^b \frac{(E - \varepsilon_C)}{1 + \exp\left(\frac{E - \varepsilon_H}{kT_H}\right)} dE \quad (\text{I.10})$$

Then $\dot{Q}_H = I_1 + I_2$, and $\dot{Q}_C = I_3 + I_4$

I_1 will be calculated analytically. I_2 , I_3 and I_4 may be calculated similarly.

Using integration by parts

$$I_1 = [(E - \varepsilon_H) I_5]_a^b - \int_a^b I_5 dE = [(E - \varepsilon_H) I_5]_a^b - I_6 \quad (\text{I.11})$$

where

$$I_5 = \frac{2}{h} \int \frac{dE}{1 + \exp\left(\frac{E - \varepsilon_C}{kT_C}\right)} \quad (\text{I.12})$$

Using the substitution

$$x = \exp\left(\frac{E - \varepsilon_C}{kT_C}\right) \quad (\text{I.13})$$

gives

$$I_5 = \frac{2}{h} kT_C \int \frac{1}{x} \frac{1}{1+x} dx \quad (\text{I.14})$$

$$= \frac{2}{h} kT_C \int \frac{1}{x} - \frac{1}{1+x} dx \quad (\text{I.15})$$

$$= \frac{2}{h} kT_C \ln \left[\frac{\exp\left(\frac{E-\varepsilon_C}{kT_C}\right)}{1 + \exp\left(\frac{E-\varepsilon_C}{kT_C}\right)} \right] \quad (\text{I.16})$$

and where

$$I_6 = \int_a^b I_5 dE = \frac{2}{h} kT_C \int_a^b \ln \left[\frac{\exp\left(\frac{E-\varepsilon_C}{kT_C}\right)}{1 + \exp\left(\frac{E-\varepsilon_C}{kT_C}\right)} \right] dE \quad (\text{I.17})$$

Again the substitution I.13 is used to obtain

$$I_6 = \frac{2}{h} (kT_C)^2 \int_a^b \frac{1}{x} \ln \left[\frac{x}{1+x} \right] dx \quad (\text{I.18})$$

then the substitution $u = x/(1+x)$ is used to obtain

$$I_6 = \frac{2}{h} (kT_C)^2 \int_a^b \ln[u] \frac{1-u}{u} \frac{du}{(1-u)^2} \quad (\text{I.19})$$

$$= \frac{2}{h} (kT_C)^2 \int_a^b \left(\frac{\ln[u]}{u} + \frac{\ln[u]}{1-u} \right) du \quad (\text{I.20})$$

$$= \frac{2}{h} (kT_C)^2 \left[\ln \left[\frac{\exp\left(\frac{E-\varepsilon_C}{kT_C}\right)}{1 + \exp\left(\frac{E-\varepsilon_C}{kT_C}\right)} \right]^2 + \text{di log} \left[\frac{\exp\left(\frac{E-\varepsilon_C}{kT_C}\right)}{1 + \exp\left(\frac{E-\varepsilon_C}{kT_C}\right)} \right] \right]_a^b \quad (\text{I.21})$$

The function dilog is defined as

$$\text{di log}(x) = \int_1^x \frac{\ln(t)}{1-t} dt \quad (\text{I.22})$$

Using the notation $\gamma_C = (E - \varepsilon_C)/(kT_C)$ and $\gamma_C = (E - \varepsilon_C)/(kT_C)$, and doing the integrals I_2 , I_3 and I_4 in a similar manner to the above, gives the

following results for \dot{Q}_H and \dot{Q}_C .

$$\dot{Q}_H = \frac{2}{h} \left[\begin{array}{l} kT_C kT_H \gamma_H \ln \left(\frac{\exp(\gamma_C)}{1+\exp(\gamma_C)} \right) - (kT_C)^2 \ln \left(\frac{\exp(\gamma_C)}{1+\exp(\gamma_C)} \right)^2 \\ - (kT_C)^2 \text{di log} \left(\frac{\exp(\gamma_C)}{1+\exp(\gamma_C)} \right) - (kT_H)^2 \gamma_H \ln \left(\frac{\exp(\gamma_H)}{1+\exp(\gamma_H)} \right) \\ + (kT_H)^2 \ln \left(\frac{\exp(\gamma_H)}{1+\exp(\gamma_H)} \right)^2 + (kT_H)^2 \text{di log} \left(\frac{\exp(\gamma_H)}{1+\exp(\gamma_H)} \right) \end{array} \right]_a^b \quad (\text{I.23})$$

$$\dot{Q}_C = -\frac{2}{h} \left[\begin{array}{l} (kT_C)^2 \gamma_C \ln \left(\frac{\exp(\gamma_C)}{1+\exp(\gamma_C)} \right) - (kT_C)^2 \ln \left(\frac{\exp(\gamma_C)}{1+\exp(\gamma_C)} \right)^2 \\ - (kT_C)^2 \text{di log} \left(\frac{\exp(\gamma_C)}{1+\exp(\gamma_C)} \right) - kT_H kT_C \gamma_C \ln \left(\frac{\exp(\gamma_H)}{1+\exp(\gamma_H)} \right) \\ + (kT_H)^2 \ln \left(\frac{\exp(\gamma_H)}{1+\exp(\gamma_H)} \right)^2 + (kT_H)^2 \text{di log} \left(\frac{\exp(\gamma_H)}{1+\exp(\gamma_H)} \right) \end{array} \right]_a^b \quad (\text{I.24})$$

The maximum power of the device as a heat engine, and the efficiency of the device at this maximum power will be given when these integrals are evaluated between the limits E_0 and ∞ . Using the notation

$$\gamma_0 = \frac{\varepsilon_C - \varepsilon_H}{kT_H - kT_C} \quad (\text{I.25})$$

and equations I.3 and I.4 gives

$$P_{HE}^{\max} = -\frac{2}{h} (kT_H - kT_C)^2 \gamma_0 \ln \left(\frac{\exp(\gamma_0)}{1 + \exp(\gamma_0)} \right) \quad (\text{I.26})$$

$$\eta_{HE}^{\max} = \frac{(1 - \tau)}{(1 + \tau)} \frac{-\gamma_0 \ln \left(\frac{\exp(\gamma_0)}{1 + \exp(\gamma_0)} \right)}{\left[\ln \left(\frac{\exp(\gamma_0)}{1 + \exp(\gamma_0)} \right)^2 + \text{di log} \left(\frac{\exp(\gamma_0)}{1 + \exp(\gamma_0)} \right) - \frac{1}{1 + \tau} \gamma_0 \ln \left(\frac{\exp(\gamma_0)}{1 + \exp(\gamma_0)} \right) \right]} \quad (\text{I.27})$$

where $\tau = T_C/T_H$.

The maximum power of the device when it is behaving as a refrigerator will be given when equations I.23 and I.24 are evaluated between the limits

ε_C and E_0 . Using equations I.5 and I.6 we obtain

$$P_R^{\max} = \frac{2}{h} \left[\begin{aligned} & -\gamma_0 k T_C (k T_H - k T_C) \ln \left(\frac{\exp(\gamma_0)}{1 + \exp(\gamma_0)} \right) \\ & + [(k T_H)^2 - (k T_C)^2] \left[\ln \left(\frac{\exp(\gamma_0)}{1 + \exp(\gamma_0)} \right)^2 + \text{di} \log \left(\frac{\exp(\gamma_0)}{1 + \exp(\gamma_0)} \right) \right] \\ & + (k T_C)^2 \left[\ln \left(\frac{1}{2} \right)^2 + \text{di} \log \left(\frac{1}{2} \right) \right] \\ & - (k T_H)^2 \left[\begin{aligned} & \ln \left(\frac{\exp[(\varepsilon_C - \varepsilon_H)/k T_H]}{1 + \exp[(\varepsilon_C - \varepsilon_H)/k T_H]} \right)^2 \\ & + \text{di} \log \left(\frac{\exp[(\varepsilon_C - \varepsilon_H)/k T_H]}{1 + \exp[(\varepsilon_C - \varepsilon_H)/k T_H]} \right) \end{aligned} \right] \end{aligned} \right] \quad (\text{I.28})$$

$$\eta_R^{\max} = \frac{2}{h} \left[\frac{P_R^{\max}}{\dot{Q}_{in}} \right] \quad (\text{I.29})$$

where

$$\begin{aligned} \dot{Q}_{in} = & (k T_H - k T_C)^2 \gamma_0 \ln \left(\frac{\exp(\gamma_0)}{1 + \exp(\gamma_0)} \right) \\ & - (\varepsilon_C - \varepsilon_H) \left[\begin{aligned} & T_H \ln \left(\frac{\exp[(\varepsilon_C - \varepsilon_H)/k T_H]}{1 + \exp[(\varepsilon_C - \varepsilon_H)/k T_H]} \right) \\ & - T_C \ln \left(\frac{1}{2} \right) \end{aligned} \right] \end{aligned} \quad (\text{I.30})$$

Bibliography

- [1] M.v. Smoluchowski. Experimentell nachweisbare, der üblichen thermodynamik widersprechende molekularchänomene. *Physik. Zeitschr.*, 13:1069, 1912.
- [2] R.P. Feynman, R.B Leighton, and M. Sands. *The Feynman Lectures on Physics, Vol I*, pages 46.1–46.9. Addison-Wesley, Reading, 1966.
- [3] J.M.R Parrondo and P. Español. Criticism of Feynman’s analysis of the ratchet as a heat engine. *Am. J. Phys.*, 64:1125–1139, 1996.
- [4] P. Reimann. Noisy transport in periodic systems far from equilibrium. *Phys. Rep.*, 361:57, 2002.
- [5] J. Prost, J.F. Chauwin, L. Peliti, and A. Adjari. Asymmetric pumping of particles. *Phys. Rev. Lett.*, 72:2652–2655, 1994.
- [6] R.D. Astumian and M. Bier. Fluctuation driven ratchets: Molecular motors. *Phys. Rev. Lett.*, 72:1766, 1994.
- [7] J. Rousselet, L. Salome, A. Ajdari, and J. Prost. Directional motion of a Brownian particle induced by a periodic asymmetric potential. *Nature*, 370:446, 1994.
- [8] M. Bier. Reversal of noise induced flow. *Phys. Lett. A*, 211:12, 1996.
- [9] L. Schimansky-Geier, M. Kschischo, and T. Fricke. Flux of particles in a sawtooth media. *Phys. Rev. Lett.*, 79:3335, 1997.

- [10] J.M.R Parrondo. Reversible ratchets as Brownian particles in an adiabatically changing periodic potential. *Phys. Rev. E*, 57:7297, 1998.
- [11] M.O. Magnasco. Forced thermal ratchets. *Phys. Rev. Lett.*, 71:1477, 1993.
- [12] R. Bartussek, P. Hänggi, and J.G. Kissner. Periodically rocked thermal ratchets. *Europhys. Lett.*, 28:459–464, 1994.
- [13] C.R. Doering, W. Horsthemke, and J. Riordan. Nonequilibrium fluctuation-induced transport. *Phys. Rev. Lett.*, 72:2984–2987, 1994.
- [14] J. Luczka, R. Bartussek, and P. Hänggi. White-noise-induced transport in periodic structures. *Europhys. Lett.*, 31:431, 1995.
- [15] R. Bartussek, P. Reimann, and P. Hänggi. Precise numerics versus theory for correlation ratchets. *Phys. Rev. Lett.*, 76:1166, 1996.
- [16] J. Kula, T. Czernik, and J. Luczka. Brownian ratchets: Transport controlled by thermal noise. *Phys. Rev. Lett.*, 80:1377–1380, 1998.
- [17] B. Alberts. *Molecular Biology of the Cell (2nd ed.)*. Garland, New York, 1989.
- [18] F. Jülicher, A. Adjari, and J. Prost. Modeling molecular motors. *Rev. Mod. Physics*, 69:1269–1281, 1997.
- [19] R.D. Astumian. Thermodynamics and kinetics of a Brownian motor. *Science*, 276:917–922, 1997.
- [20] H. Chou, C. Spence, A. Scherer, and S. Quake. A microfabricated device for sizing and sorting DNA molecules. *Proc. Nat. Acad. Sci. USA*, 96:11–13, 1999.
- [21] P. Cohen. Speedy sorting. *New Scientist*, 164:11, 1999.

- [22] J.S. Bader, R.W. Hammond, S.A. Henck, M.W. Deem, G.A. McDermott, J.M. Bustillo, J.W. Simpson, G.T. Mulhern, and J.M. Rothberg. *Proc. Nat. Acad. Sci. U.S.A.*, 96:13165, 1999.
- [23] C. Marquet, A. Buguin, L. Talini, and R. Silberzan. Rectified motion of colloids in asymmetrically structured channels. *Phys. Rev. Lett.*, 88:168301, 2002.
- [24] Z. Siwy and A. Fuliński. Fabrication of a synthetic nanopore ion pump. *Phys. Rev. Lett.*, 89:198103, 2002.
- [25] P. Reimann, M. Grifoni, and P. Hänggi. Quantum ratchets. *Phys. Rev. Lett.*, 79:10, 1997.
- [26] H. Linke, T.E. Humphrey, A. Löfgren, A.O. Sushkov, R. Newbury, R.P. Taylor, and P. Omling. Experimental tunneling ratchets. *Science*, 286:2314–2317, 1999.
- [27] H. Linke, W. Sheng, A. Löfgren, H. Xu, P. Omling, and P.E. Lindelof. A quantum dot ratchet: Experiment and theory. *Europhys. Lett.*, 44:341–347, 1998.
- [28] H. Linke, W. Sheng, A. Löfgren, H. Xu, P. Omling, and P.E. Lindelof. Erratum, a quantum dot ratchet: Experiment and theory. *Europhys. Lett.*, 45:406, 1999.
- [29] H. Linke, W.D. Sheng, A. Svensson, A. Löfgren, L. Christensson, H.Q. Xu, P. Omling, and P.E. Lindelof. Asymmetric nonlinear conductance of quantum dots with broken inversion symmetry. *Phys. Rev. B.*, 61:15914–15926, 2000.
- [30] A.P. Micolich. *Fractal Magneto-conductance Fluctuations in Mesoscopic Semiconductor Billiards*. PhD thesis, School of Physics, University of New South Wales, Sydney, 2000.

- [31] R.E. Williams. *Modern GaAs Processing Techniques, 2nd Ed.* Artech House, Boston, 1990.
- [32] R.P. Taylor. The role of surface-gate technology for AlGaAs/GaAs nanostructures. *Nanotechnology*, 5:183, 1994.
- [33] B. J. van Wees, H. van Houten, C. W. J. Beenakker, J.G. Williamson, L. P. Kouwenhoven, D. van der Marel, and C.T. Foxton. Quantised conductance of point contacts in a two-dimensional electron gas. *Phys. Rev. Lett.*, 60:848–850, 1988.
- [34] D.A. Wharam, T.J. Thornton, R. Newbury, M. Pepper, H. Ahmed, J.E.F. Frost, D.G. Hasko, D.C. Peacock, D.A. Ritchie, and G.A.C. Jones. One-dimensional transport and the quantization of the ballistic resistance. *J. Phys. C Solid State*, 21:L209–L214, 1988.
- [35] R. Landauer. Spatial variation of currents and fields due to localized scatterers in metallic conduction. *IBM J. Res. Dev.*, 1:223, 1957.
- [36] R. Landauer. Can a length of perfect conductor have a resistance? *Phys. Lett.*, 85A:91, 1981.
- [37] M. Büttiker, Y. Imry, R. Landauer, and S. Pinhas. Generalized many-channel conductance formula with application to small rings. *Phys. Rev. B*, 31:6207, 1985.
- [38] D.S. Fisher and P.A. Lee. Relation between conductivity and transmission matrix. *Phys. Rev. B*, 23:6851, 1981.
- [39] Y. Imry. *Introduction to Mesoscopic Physics*. Oxford University Press, New York, 1997.
- [40] S. Datta. *Electronic Transport in Mesoscopic Systems*. Cambridge University Press, Cambridge, 1997.
- [41] J. H. Davies. *The Physics of Low-Dimensional Semiconductors*. Cambridge University Press, Cambridge, 1999.

- [42] L. Martín-Moreno, J.T. Nicholls, N.K. Patel, and M. Pepper. Non-linear conductance of a saddle point constriction. *J. Phys.: Condens. Matter*, 4:1323, 1992.
- [43] A. Kristensen, H. Bruus, A.E. Hansen, J.B. Jensen, P.E. Lindelof, C.J. Marckmann, J. Nygard, and C.B. Sørensen. Bias and temperature dependence of the 0.7 conductance anomaly in quantum point contacts. *Phys. Rev. B*, 62:10950, 2000.
- [44] S.M. Sze. *Semiconductor Devices Physics and Technology*, pages 201–203. John Wiley and Sons, New York, 1985.
- [45] A. Löfgren. *Linear and Nonlinear Transport in Quantum Nanostructures*. PhD thesis, Division of Solid State Physics, Lund Institute of Technology, Lund University, 2002.
- [46] S.M. Cronenwett, H.J. Lynch, D. Goldhaber-Gordon, L.P. Kouwenhoven, C.M. Marcus, K. Hirose, N.S. Wingreen, and V. Umansky. Low-temperature fate of the 0.7 structure in a point contact: A Kondo-like correlated state in an open system. *Phys. Rev. Lett.*, 88:226805, 2002.
- [47] D.J. Reilly, T.M. Buehler, J.L. O’Brian, A.R. Hamilton, A.S. Dzurak, R.G. Clark, B.E. Kane, L.N. Pfeiffer, and K.W. West. Density-dependent spin polarization in ultralow-disorder quantum wires. *Phys. Rev. Lett.*, 89:246801, 2002.
- [48] K.J. Thomas, J.T. Nicholls, M.Y. Simmons, M. Pepper, D.R. Mace, and D.A. Ritchie. Possible spin polarization in a one-dimensional gas. *Phys. Rev. Lett.*, 77:135–138, 1996.
- [49] K.J. Thomas, J.T. Nicholls, N.J. Appleyard, M.Y. Simmons, M. Pepper, D.R. Mace, W.R. Tribe, and D.A. Ritchie. Interaction effects in a one-dimensional constriction. *Phys. Rev. B*, 58:4846–4852, 1998.

- [50] B.E. Kane, G.R. Facer, A.S. Dzurak, N.E. Lumpkin, and R.G. Clark. Quantized conductance in quantum wires with gate-controlled width and electron density. *Appl. Phys. Lett.*, 72:3506–3508, 1998.
- [51] D.J. Reilly, G.R. Facer, A.S. Dzurak, B.E. Kane, R.G. Clark, P.J. Stiles, A.R. Hamilton, J.L. O’Brien, and N.E. Lumpkin. Many-body spin-related phenomena in ultra low-disorder quantum wires. *Phys. Rev. B*, 63:121311, 2001.
- [52] P.E. Lindelof. Effect on conductance of an isomer state in a quantum point contact. *SPIE Proc. Optical Organic and Inorganic Materials*, 4415:77–85, 2001.
- [53] Chuan-Kui Wang and K.-F. Berggren. Local spin polarization in ballistic quantum point contacts. *Phys. Rev. B*, 57:4552–4556, 1998.
- [54] L. Calmels and A. Gold. Spin-polarized electron gas in quantum wires: Anisotropic confinement model. *Solid State Commun.*, 106:139, 1998.
- [55] N. Zabala, M.J. Puska, and R.M. Nieminen. Spontaneous magnetization of simple metal nanowires. *Phys. Rev. Lett.*, 80:3336–3339, 1998.
- [56] B. Spivak and Z. Zhou. Ferromagnetic correlations in quasi-one-dimensional conducting channels. *Phys. Rev. B*, 61:16730–16735, 2000.
- [57] K.F. Berggren and I.I. Yakimenko. Effects of exchange and electron correlation on conduction and nanomagnetism in ballistic semiconductor quantum point contacts. *Phys. Rev. B*, 66:085323, 2002.
- [58] V.V. Flambaum and M.Yu. Kuchiev. Possible mechanism of the fractional quantisation in a one-dimensional constriction. *Phys. Rev. B*, 61:R7869, 2000.
- [59] T. Rejec and A. Ramšac. Spin-dependent resonances in the conduction edge of quantum wires. *Phys. Rev. B*, 62:12985, 2000.

- [60] Kenji Hirose, Yigal Meir, and Ned S. Wingreen. Local moment formation in quantum point contacts. *Phys. Rev. Lett.*, 90:026804, 2003.
- [61] Georg Seelig and K.A. Mateev. Electron-phonon scattering in quantum point contacts. *Phys. Rev. Lett.*, 90:176804, 2003.
- [62] O.P. Sushkov. Restricted and unrestricted Hartree-Fock calculations of conductance for a quantum point contact. *Phys. Rev. B*, 67:195318, 2003.
- [63] I.H. Tan, G.L. Snider, L.D. Chang, and E.L. Hu. A self-consistent solution of Schrödinger-Poisson equations using a non-uniform mesh. *J. Appl. Phys.*, 68:4071, 1990.
- [64] H. Xu. Theory of nonlinear ballistic transport in quasi-one-dimensional constrictions. *Phys. Rev. B*, 47:15630, 1993.
- [65] D.R. Hartree. *Numerical Analysis*, page 142. Oxford University Press, London, 1958.
- [66] M. Büttiker. Quantised transmission of a saddle-point constriction. *Phys. Rev. B*, 41:7906, 1990.
- [67] Francis W. Sears and Gerhard L. Salinger. *Thermodynamics, Kinetic Theory, and Statistical Thermodynamics*. Addison-Wesley, Reading, Massachusetts, 1986.
- [68] S. Carnot. *Réflexions sur la Puissance Motrice du Feu et sur les Machines propres à D’évelopper cette Puissance*. Bachelier, Paris, 1824.
- [69] A.F. Ioffe. *Semiconductor thermoelements and thermoelectric cooling*. Infosearch, London, 1957.
- [70] G.D. Mahan. Thermionic refrigeration. *J. Appl. Phys.*, 76:4362–4366, 1994.

- [71] G.S. Nolas, J. Sharp, and H.J. Goldsmid. *Thermoelectrics*. Springer, Berlin, 2001.
- [72] M. Nahum, T.M. Eiles, and J.M. Martinis. Electronic microrefrigerator based on a normal-insulator-superconductor tunnel junction. *Appl. Phys. Lett.*, 65:3123, 1994.
- [73] H.L. Edwards, Q. Niu, and A.L. de Lozanne. A quantum-dot refrigerator. *Appl. Phys. Lett.*, 63:1815–1817, 1993.
- [74] G.D. Mahan, J.O. Sofo, and M. Bartkowiak. Multilayer thermionic refrigerator and generator. *J. Appl. Phys.*, 83:4683–4689, 1998.
- [75] G.D. Mahan. Good thermoelectrics. *Solid State Physics*, 51:82, 1998.
- [76] F.J. DiSalvo. Thermoelectric cooling and power generation. *Science*, 285:703, 1999.
- [77] C. Wood. Materials for thermoelectric energy conversion. *Rep. Prog. Phys.*, 51:459, 1988.
- [78] Y. Hishinuma, T.H. Geballe, B.Y. Mozyshes, and T.W. Kenny. Refrigeration by combined tunneling and thermionic emission in vacuum: Use of nanometer scale design. *Appl. Phys. Lett.*, 78:2572, 2001.
- [79] Y. Hishinuma, B.Y. Mozyshes, T.H. Geballe, and T.W. Kenny. Vacuum thermionic refrigeration with a semiconductor heterojunction structure. *Appl. Phys. Lett.*, 81, 2002.
- [80] C.B. Vining and G.D. Mahan. The b factor in multilayer thermionic refrigeration. *Appl. Phys. Lett.*, 86:6852, 1999.
- [81] M.D. Ulrich, P.A. Barnes, and C.B. Vining. Comparison of solid-state thermionic refrigeration with thermoelectric refrigeration. *J. Appl. Phys.*, 90:1625, 2001.

- [82] H.L. Edwards, Q. Niu, G.A. Georgakis, and A.L. de Lozanne. Cryogenic cooling using tunneling structures with sharp energy features. *Phys. Rev. B*, 52:5714–5736, 1995.
- [83] M.M. Leivo, J.P. Pekola, and D.V. Averin. Efficient peltier refrigeration by a pair of normal metal/insulator/superconductor junctions. *Appl. Phys. Lett.*, 68:1996, 1996.
- [84] A.J. Manninen, M.M. Leivo, and J.P. Pekola. Refrigeration of a dielectric membrane by a superconductor/insulator/normal-metal/insulator/superconductor tunneling. *Appl. Phys. Lett.*, 70:1885–1887, 1997.
- [85] M.M. Leivo, A.J. Manninen, and J.P. Pekola. Microrefrigeration by normal-metal/insulator/superconductor tunnel junctions. *Appl. Supercond.*, 5:227–233, 1998.
- [86] J.P. Pekola, J.M. Kyyräinen, M.M. Leivo, and A.J. Manninen. NIS chip refrigeration. *Cryogenics*, 39:653–657, 1999.
- [87] J.M.R Parrondo and B. Jiménez de Cisneros. Energetics of Brownian motors: A review. *Appl. Phys. A-Mater*, 75:179–191, 2002.
- [88] K. Sekimoto. Kinetic characterization of heat bath and the energetics of thermal ratchet models. *J. Phys. Soc. Japan*, 66:1234–1237, 1997.
- [89] K. Sekimoto and S. Sasa. Complementary relations for irreversible processes derived from stochastic energetics. *J. Phys. Soc. Japan*, 66:3326, 1997.
- [90] K. Sekimoto, F. Takagi, and T. Hondou. *Phys. Rev. E*, 62:7759, 2000.
- [91] L. Brillouin. Can the rectifier become a thermodynamics demon? *Phys. Rev.*, 78:627, 1950.
- [92] I.M. Sokolov. On the energetics of a nonlinear system rectifying thermal fluctuations. *Europhys. Lett.*, 44:278–283, 1998.

- [93] I.M. Sokolov. Reversible fluctuation rectifier. *Phys. Rev. E*, 60:4946–4949, 1999.
- [94] M. Büttiker. Transport as a consequence of state-dependent diffusion. *Z. Phys. B*, 68:161–167, 1987.
- [95] R. Landauer. Motion out of noisy states. *J. Stat. Phys.*, 53:233–248, 1988.
- [96] I. Derényi and R.D. Astumian. Efficiency of Brownian heat engines. *Phys. Rev. E*, 59:R6219–R6222, 1999.
- [97] T.E. Humphrey, R. Newbury, R.P. Taylor, and H. Linke. Reversible quantum Brownian heat engines for electrons. *Phys. Rev. Lett.*, 89:116801, 2002.
- [98] F.L. Curzon and B. Ahlborn. Efficiency of a Carnot engine at maximum power output. *Am. J. Phys.*, 43:22–24, 1975.
- [99] P. Salamon, B. Andresen, and R.S. Berry. Thermodynamics in finite time. II. potentials for finite-time processes. *Phys. Rev. A*, 15:2094, 1977.
- [100] P. Salamon, A. Nitzan, B. Andresen, and R.S. Berry. Minimum entropy production and the optimization of heat engines. *Phys. Rev. A*, 21:2115, 1980.
- [101] B. Andresen, P. Salamon, and R.S. Berry. Thermodynamics in finite time. *Physics Today*, 84:62–70, 1984.
- [102] A. de Vos. *Endoreversible Thermodynamics of Solar Energy Conversion*. Oxford University Press, New York, 1992.
- [103] H. Leff. Thermal efficiencies at maximum work output: new results for old heat engines. *American Journal of Physics*, 55:602, 1987.

- [104] P.T. Landsburg and H. Leff. Thermodynamic cycles with nearly universal maximum-power efficiencies. *Journal of Physics A: Mathematical and General*, 22:4019, 1989.
- [105] J. Gordon. Maximum power point characteristics of heat engines as a general thermodynamic problem. *American Journal of Physics*, 57:1136, 1989.
- [106] L. Chen and Z. Yan. The effect of heat-transfer law on performance of a two-heat-source endoreversible cycle. *J. Chem. Phys.*, 90:3740–3743, 1989.
- [107] J. Chen. The maximum power output and maximum efficiency of an irreversible Carnot heat engine. *J. Phys. D: Appl. Phys.*, 27:1144–1149, 1994.
- [108] F. Angulo-Brown, L.A Hernández, and R. Páez-Hernández. A general property of non-endoreversible thermal cycles. *J. Phys. D: Appl. Phys.*, 32:1415, 1999.
- [109] S. Velasco, J.M.M. Roco, A. Medina, and A.C. Hernández. New performance bounds for a finite-time Carnot refrigerator. *Phys. Rev. Lett.*, 78:3241, 1997.
- [110] Z. Yan and J. Chen. Comment on "new performance bounds for a finite-time Carnot refrigerator". *Phys. Rev. Lett.*, 81:5469, 1998.
- [111] S. Velasco, J.M.M. Roco, A. Medina, and A.C. Hernández. Reply to yan and chen: Comment on "new performance bounds for a finite-time Carnot refrigerator". *Phys. Rev. Lett.*, 81:5470, 1998.
- [112] S. Velasco, J.M.M. Roco, A. Medina, and A.C. Hernández. Feynman's ratchet optimization: maximum power and maximum efficiency regimes. *J. Phys. D: Appl. Phys.*, 34:1000–1006, 2001.

- [113] N.S. Salas and A.C. Hernández. Nonlinear systems rectifying thermal fluctuations: maximum power and maximum efficiency regimes. *J. Phys. D: Appl. Phys.*, 35:1442–1446, 2002.
- [114] T.E. Humphrey, H. Linke, and R. Newbury. Pumping heat with quantum ratchets. *Physica E*, 11:281–286, 2001.
- [115] E. Boneta, M.M. Desmukh, and D.C. Ralph. Solving rate equations for electron tunneling via discrete quantum states. *Physical Review B*, 65:045317, 2002.
- [116] E. Geva and R. Kosloff. The quantum heat engine and heat pump: An irreversible thermodynamic analysis of the three-level amplifier. *J. Chem. Phys.*, 104:7681–7699, 1996.
- [117] H.E.D. Scovil and E.O. Schulz-DuBois. Three-level masers as heat engines. *Phys. Rev. Lett.*, 2:262–263, 1959.
- [118] E. Geva and R. Kosloff. Three-level quantum amplifier as a heat engine: A study in finite time thermodynamics. *Phys. Rev. E*, 49:3903–1918, 1994.
- [119] E. Geva. On the irreversible performance of a quantum heat engine. *J. Mod. Optics*, 49:635–644, 2002.
- [120] W.E. Lamb. Theory of an optical maser. *Phys. Rev.*, 134:A1429, 1964.
- [121] M. Boero and J.C. Inkson. Calculated I-V characteristics of low-dimensional structures. *Surface Science*, 361:618, 1996.
- [122] M. Boero, J.C Inkson, G. Faini, C. Vieu, F. Laruelle, E. Bedel, and C. Fontaine. Study of ion-implanted semiconductor nanostructures. *Surface Science*, 377-379:103–107, 1997.
- [123] Y. Meir and N.S. Wingreen. Landauer formula for the current through an interacting electron region. *Phys. Rev. Lett.*, 68:2512, 1992.